Numerical Evaluation of Feynman Loop Integrals by Reduction to Tree Graphs

Dissertation
zur Erlangung des Doktorgrades
des Departments Physik
der Universität Hamburg

vorgelegt von
Tobias Kleinschmidt
aus Duisburg

Hamburg
2007

Gutachter des Dissertation:	Prof. Dr. W. Kilian
	Prof. Dr. J. Bartels
Gutachter der Disputation:	Prof. Dr. W. Kilian
	Prof. Dr. G. Sigl
Datum der Disputation:	18. 12. 2007
Vorsitzender des Prüfungsausschusses:	Dr. H. D. Rüter
Vorsitzender des Promotionsausschusses:	Prof. Dr. G. Huber
Dekan der Fakultät MIN:	Prof. Dr. A. Frühwald

Abstract

We present a method for the numerical evaluation of loop integrals, based on the Feynman Tree Theorem. This states that loop graphs can be expressed as a sum of tree graphs with additional external on-shell particles. The original loop integral is replaced by a phase space integration over the additional particles. In cross section calculations and for event generation, this phase space can be sampled simultaneously with the phase space of the original external particles. Since very sophisticated matrix element generators for tree graph amplitudes exist and phase space integrations are generically well understood, this method is suited for a future implementation in a fully automated Monte Carlo event generator. A scheme for renormalization and regularization is presented. We show the construction of subtraction graphs which cancel ultraviolet divergences and present a method to cancel internal on-shell singularities. Real emission graphs can be naturally included in the phase space integral of the additional on-shell particles to cancel infrared divergences. As a proof of concept, we apply this method to NLO Bhabha scattering in QED. Cross sections are calculated and are in agreement with results from conventional methods. We also construct a Monte Carlo event generator and present results.

Zusammenfassung

Es wird eine Methode zur numerischen Auswertung von Schleifengraphen vorgestellt, die auf dem Feynman Tree Theorem beruht. Dieses sagt aus, daß ein Schleifengraph durch eine Summe von Baumgraphen mit zusätzlichen Teilchen auf der Massenschale ausgedrückt werden kann. Das ursprüngliche Schleifenintegral wird dabei durch ein Phasenraumintegral ersetzt. In Berechnungen von Wirkungsquerschnitten und bei der Erzeugung von Ereignissen kann dieses Integral gleichzeitig mit der Phasenraumintegration der ursprünglichen externen Teilchen ausgewertet werden. Da für die Erzeugung von Baumgraphen weit entwickelte Matrixelementgeneratoren existieren und Phasenraumintegrationen im Allgemeinen sehr gut verstanden sind, ist diese Methode für eine spätere Implementierung in einem Monte Carlo Ereignis Generator gut geeignet. Es wird ein Schema zur Renormierung und Regularisierung vorgestellt. Es werden dabei Subtraktionsgraphen konstruiert, die die UV-Divergenzen aufheben. Weiterhin wird eine Methode zur Aufhebung interner Singularitäten präsentiert. Infrarotdivergenzen werden durch die Hinzunahme von reellen Abstrahlungen niederenergetischer masseloser Teilchen aufgehoben. Diese können auf natürliche Weise unter das Phasenraumintegral über die zusätzlichen Teilchen hinzugenommen werden. Um eine Bestätigung für die Anwendbarkeit dieser Methode zu erlangen, wird die Berechnung von Wirkungsquerschnitten der Bhabha-Streuung in erster Ordnung in QED gezeigt. Die Resultate werden mit denen konventioneller Methoden verglichen. Ein Monte Carlo Ereignis Generator wird vorgestellt und Ergebnisse präsentiert.

Contents

1. Introduction

The task of high energy physics is on the one hand to find models which, based on symmetry principles, predict the outcomes of any experiment by as few free input parameters as possible and on the other hand to precisely measure observables and corresponding free parameters to verify or falsify a theory and get hints of further underlying symmetries. Deviations from predicted values of observables or the findings of new degrees of freedom can then be used to construct models whose predictability spans a wider range of energy, resulting in a refined and in a scientific sense simpler picture of our nature.

Up to an energy scale of roughly 100 GeV the Standard Model of particle physics (SM) has proven very successful[1]. It is a $SU(3)_c \times SU(2)_L \times U(1)_Y$ gauge theory incorporating the fundamental strong, electromagnetic and weak interactions. The latter two are jointly described by the $SU(2)_L \times U(1)_Y$ electroweak gauge group. However, the W- and Z-bosons are massive and since gauge invariance forbids an explicit mass term for the gauge bosons, this symmetry has to be broken. Furthermore, the scattering amplitude of longitudinal polarized massive vector bosons rises proportional to the center of mass energy squared s. This would lead to a violation of unitarity at an energy of about 1.2 TeV if not compensated by a new particle or the onset of a new strong interaction. Similar upper bounds are also obtained for massive fermions. In the standard model, the electroweak symmetry is broken by a $SU(2)$ scalar Higgs doublet with a non-vanishing vacuum expectation value. This gives masses to three of the four bosons of the $SU(2)_L \times U(1)_Y$ gauge group and introduces a new physical particle, the Higgs boson. Apart from this scalar, all particles predicted by the standard model have been found and experimental precision data [5] agrees very well with the predictions of the standard model, which has about 20 free parameters.

In this form, the standard model can be valid up to the Planck scale, where gravitational interactions become as strong as the other three fundamental forces. However, it is very unnatural to have a light scalar in the presence of such a high scale. There is no mechanism or symmetry to prevent the Higgs mass to be of the order of the Planck scale due to radiative corrections. Thus, to get a Higgs scalar with mass at the electroweak scale, counterterms have to be added in the renormalization procedure, which are of the order of the Planck scale and cancel the quadratic divergence to obtain a squared mass of the physical Higgs boson which lies about 30 orders of magnitude below that scale.

An elegant solution to this problem is the minimal supersymmetric extension of the standard model (MSSM) via the introduction of a symmetry relating bosons and fermions [6,7]. Here, the quadratic divergences in the corrections to the Higgs self energy are canceled by additional loop terms containing the supersymmetric partners of the standard model particles. Furthermore, if supersymmetry (SUSY) is broken at the TeV-scale, the couplings of the strong, electromagnetic and weak interactions come close to each other at a scale of about 10^{16} GeV, indicating a possible unification of the couplings and an embedding of

[1] For a full review of the Standard Model, see the standard textbooks, e.g. [1–4], and references therein.

the gauge groups in a bigger group. A further, independent hint to a grand unification (GUT) is the value of the Weinberg angle $\sin^2\theta_W \simeq 0.231$ which is predicted by such theories to be $\frac{3}{8}$ at the GUT scale, resulting in a value of 0.203 at the electroweak scale through renormalization group running, very close to the measured value. A third virtue of a TeV-scale SUSY is a lightest supersymmetric particle, which, if stable, would have the right magnitude of relic density to step in as a candidate for cold dark matter.

In the next year, the Large Hadron Collider (LHC) will begin taking data. The International Linear Collider (ILC) is scheduled for the year 2014. These two high energy particle colliders are the first ones entering the TeV regime. Thus, as described above, it is likely that physics responsible for the breaking of the electroweak symmetry is found and pinned down to a certain mechanism by precision measurements in the next decades. Furthermore, it would be *natural* to find physics beyond the standard model in this energy regime, mitigating the huge discrepancy between the Planck and the electroweak scale. In the discovery and the measurements of parameters of new physics these two colliders, one being a proton/(anti)proton - the other an e^+e^--collider, often play a complementary role [8].

Extraction of parameters and comparison with theory is a highly non-trivial task. The multiplicity of final states in a particle collision is immense, at the LHC several hundred final state particles per event are expected. The detectors require accurate understanding to know their influence on the extracted data. Perturbative calculations of strong interactions involve partonic quarks and gluons, while the final states detected are hadrons. This transition is understood only empirically. To help the reconstruction and studies of multi particle events and to study detector requirements and the feasibility of analyses, simulation programs are needed. These Monte Carlo event generators are set up in several stages according to the energy scale of the sub-processes of a collision[2]. At the highest scale lies the hard partonic sub-process, described by matrix elements up to some order in perturbation theory. In events involving hadrons, parton distribution functions have to be implemented. Parton shower algorithms have to be used to simulate the emission of additional particles from the initial and final states of the hard scattering process and their subsequent evolution down to lower scales. Produced quarks and gluons will eventually hadronize. These hadrons as well as heavy unstable particles might decay. Finally, a simulation of the detector can also be applied to mimic collision processes in experiments as good as possible.

For many processes under consideration at the upcoming colliders, the precision for the extracted parameters like masses and couplings may reach the percent to per mil regime [8]. To have a combined error of theory and experiment in the same region, the theoretical predictions should match this precision. Therefore, it is necessary to implement the matrix element, describing the hard subprocess in an event generation up to next to leading order (NLO) in perturbation theory. There are further arguments for the inclusion of NLO calculations, e.g. the rather strong dependence of the amplitudes on the renormal-

[2] see [9] and references therein

ization scale in QCD, which should decrease when higher orders are taken into account. However, loop calculations of processes with many final state particles are quite involved. There exist Monte Carlos which have some processes implemented at next to leading order [10–12], however it would be particularly favorable to have a fully automated matrix element generation at NLO and corresponding event generation. There are several groups heading for this goal. We will give an overview of these efforts and the technical tools involved in chapter 2.

In this thesis we present a method to generate and calculate matrix elements at NLO, which is very well suited for an implementation in an automated Monte Carlo event generator. The idea, reaching back to R. Feynman [13], is to consecutively cut each propagator of a loop by replacing it with a delta function. This leads to a sum of tree graphs. The cut propagator of each tree graph can be interpreted as one additional incoming and outgoing on-shell particle, which is integrated over. We regularize UV-divergent integrals by subtraction terms which are fixed by the renormalization conditions. A striking feature of the introduced method is the treatment of IR-divergences. Here the virtual and the real corrections can be evaluated under the same integral. In addition to the usual infrared and ultraviolet divergences further internal singularities appear when loop propagators get singular. These peaks are taken care of by additional fix functions. Terms resulting from multiple cuts of the loop can add further real and imaginary contributions to the results. Since these include multiple delta functions, they lower the dimension of integration and can easily be evaluated.

The proposed method allows for the calculation of loop diagrams from tree graphs. The subtraction terms from the regularization procedure can easily be obtained from these tree graphs. This facilitates a simple and fast creation of matrix elements by standard automated generators. The original loop integral is replaced by a phase space integration over the additional particle momentum. Except for the addition of the fix functions, no further manipulations of the integrand have to be made. This allows for a simple implementation in a Monte Carlo framework for cross section integration and event generation. The additional phase space integration can then be performed simultaneously with the integrations over the external momenta. When amplitudes with a higher number of legs are considered, no further techniques than those already considered have to applied to prepare the matrix elements for the numerical integration. Thus, the level of complexity of the calculations only rises due the growing number of terms which have to be considered and the growing dimension of integration. We therefore expect the method to be an efficient tool for computations in collider physics.

This thesis is structured as follows. In the next chapter we will give a short introduction to field theory with main emphasis on the choice of gauges and the renormalization scheme as well as the calculation of cross sections. Here, we will also discuss alternative approaches to calculations of NLO processes. In chapter 3 we will present the Feynman Tree Theorem (FTT) and give an improved version, suited for numerical evaluation. We will discuss the singularity structure of the integrands, give a regularization and renormalization scheme and show the treatment of infrared divergences. We will also introduce

fix functions rendering internal threshold singularities finite. A path to a generalization of the tree theorem to multi loop graphs is shown in appendix D. In chapter 4 we will discuss phase space integration and the multi channel approach used by VAMP [14]. We will present a first application of the FTT to Bhabha scattering in QED in chapter 5. This includes up to four-point functions, and the treatment of IR-,UV- and threshold singularities can be seen simultaneously. Here, we will also present results obtained with different methods of the integration algorithm as well as matrix element generation, namely by FeynArts⋄FormCalc [15,16] and O'Mega [17]. In chapter 6, we will give an overview of Monte Carlo event generation and present our implementation of the Feynman Tree Theorem in a Monte Carlo event generator for NLO Bhabha scattering. Chapter 7 summarizes and gives an outlook.

2. Field Theory - Gauges, Renormalization and Cross Sections

In this chapter we will give a short introduction to the path integral formalism of gauge theories. We point out the derivation of Feynman rules and discuss several gauge choices. We then give an overview of renormalization and introduce the BPHZ procedure which we will use for regularization. Finally, we discuss different techniques for loop integral calculations. Most of this chapter is gathered from standard field theory books and it is not intended to give a broad overview, but to lead the reader to our choices of gauge and renormalization scheme. Details can be found in [1–4, 18, 19].

2.1. de Witt - Faddeev - Popov Formalism

A convenient way to obtain Green functions and Feynman rules in a Lorentz and gauge invariant way is to extract them from a generating functional in the path integral formalism. For non-Abelian, as well as Abelian gauge theories, the vacuum-vacuum amplitude in the presence of classical currents J coupled to the field content of the theory can be represented as:

$$Z[J] = \langle \Omega_{\text{out}} | \Omega_{\text{in}} \rangle = \int \mathcal{D}A \mathcal{D}\Psi \mathcal{D}\omega \mathcal{D}\omega^* \, e^{i \int d^4x \, \left(\mathcal{L}^{\text{eff}} + \mathcal{L}_{\text{J}} \right)}. \tag{2.1}$$

Here, the integral measures run over all possible configurations of the corresponding fields:

$$\mathcal{D}A = \prod_{x,\mu,a} dA^a_\mu(x), \tag{2.2}$$

and similar for the other fields. The effective Lagrangian is composed of the terms

$$\mathcal{L}^{\text{eff}} = \mathcal{L}_{\text{m}} + \mathcal{L}_{\text{A}} + \mathcal{L}_{\text{fix}} + \mathcal{L}_{\text{gh}}, \tag{2.3}$$

which will be explained in the following. The first two terms are the common matter and gauge field Lagrangians

$$\mathcal{L}_{\text{m}} = \sum_f \bar{\Psi}_f \left(i \not{D} - m_f \right) \Psi_f \tag{2.4}$$

$$\mathcal{L}_{\text{A}} = -\frac{1}{4} F^{a,\mu\nu} F^a_{\mu\nu}. \tag{2.5}$$

The sum in the matter Lagrangian runs over all fermion flavors. Here, we explicitly wrote a mass term for fermions. We will not discuss the dynamical creation of masses due to electroweak symmetry breaking in this thesis. The field strength and the covariant derivative are given by

$$F^a_{\mu\nu} = \partial_\mu A^a_\nu - \partial_\nu A^a_\mu + g f^{abc} A^b_\mu A^c_\nu \tag{2.6}$$
$$D_\mu = \partial_\mu - ig\, t^a A^a_\mu, \tag{2.7}$$

where f^{abc} is the structure constant of the gauge group considered. In Abelian theories this term vanishes.

The path integral over the gauge field runs over all its possible configurations. Those differing only by a gauge transformation are also included and therefore the path integral is infinite. The natural procedure to get meaningful results is to factor out the infinite part and integrate only over distinct field configurations. This can be achieved by inserting a delta function in the integrand which fixes the gauge. This delta function is accompanied by a Jacobian determinant of the infinitesimal gauge transformation:

$$Z[J] = \int \mathcal{D}A \,\mathrm{Det}F\, \delta(f^a(A)) \ldots \tag{2.8}$$
$$F = \left.\frac{\delta f^a(A)}{\delta \epsilon^b}\right|_{\epsilon=0} \tag{2.9}$$

The delta function can be equivalently replaced by a Gaussian integral, leading to the gauge fixing term in the Lagrangian:

$$\mathcal{L}_{\mathrm{fix}} = -\frac{1}{2\xi} f^a f^a \tag{2.10}$$

A common choice for the gauge fixing function is the so-called covariant or Lorenz gauge,

$$f^a = \partial^\mu A^a_\mu \tag{2.11}$$

leading to the generalized ξ-gauge. We will discuss separate choices for the gauge below. Note that in Abelian gauge theories the functional determinant F does not depend on the gauge field A^a_μ, since the gauge transformation does not. Therefore, in Abelian theories the determinant is a constant term which can be pulled out of the integral and just changes its normalization.

If the determinant depends on the gauge field, as is usually the case in non-Abelian theories, one can substitute it by an additional path integral, involving auxiliary Grassmann valued fields, the Faddeev-Popov ghosts:

$$\mathrm{Det}F = \int \mathcal{D}\omega \mathcal{D}\omega^*\, e^{-i \int d^4x\, d^4y\, \omega^*(x) F(x,y) \omega(y)} \tag{2.12}$$

Thus, the ghosts only couple to the gauge fields and the structure of this coupling is directed by the choice of the gauge fixing functional $f^a(A)$. The ghost term in the effective Lagrangian can directly be read off:

$$\mathcal{L}_{\mathrm{gh}} = -\int d^4y\, \omega^*(x) F(x,y) \omega(y). \tag{2.13}$$

The last ingredient of the generating functional is the Lagrangian containing the source terms:

$$\mathcal{L}_{\mathrm{J}} = J^{a,\mu} A^a_\mu + J_\Psi \Psi - \bar{\Psi} J_{\bar{\Psi}} + J_\omega \omega - \omega^* J_{\omega^*}. \tag{2.14}$$

2.2. Feynman Rules and Gauge Choices

From the generating functional (2.1) one can now easily derive Green functions, vacuum expectation values of time ordered products of operators:

$$\langle T\, \Phi_1(x_1)\Phi_2(x_2)\cdots \rangle = \frac{\partial^n}{\partial J_1(x_1)\partial J_2(x_2)\cdots} W[J]\bigg|_{J=0}, \tag{2.15}$$

where

$$W[J] = -i \log Z[J]. \tag{2.16}$$

Here, the J_i are the sources of the corresponding fields or operators. While $Z[J]$ is the sum of all vacuum to vacuum amplitudes, $W[J]$ is the sum of all *connected* graphs. To obtain S-matrix elements, one applies the LSZ reduction formula to the Fourier transformed Green functions.

The generating functional of vertex functions is the Legendre transform of the functional $W[J]$:

$$\Gamma[A, \Psi, \bar{\Psi}, \omega, \omega^*] = -\int d^4x \mathcal{L}_{\mathrm{J}} + W[J]. \tag{2.17}$$

This can be interpreted as the sum of all connected one-particle-irreducible (1PI) graphs. To obtain the vertex function of any combination of fields, one just takes the variational derivative with respect to these fields and sets all fields to zero afterwards. For the two point function of the vector boson A this would be:

$$\Gamma^{AA}_{\mu\nu}(x_1,x_2) = \frac{\delta^2}{\delta A^\mu(x_1)\delta A^\nu(x_2)} \Gamma[A, \Psi, \bar{\Psi}, \omega, \omega^*]\bigg|_{A=\Psi=\omega=\omega^*=0} \tag{2.18}$$

The full propagator can then be obtained by inverting $\Gamma^{AA}_{\mu\nu}(x_1,x_2)$. The generating functional for vertex functions can be expanded in a series of the Planck constant $\hbar$, which effectively is an expansion in loops[1]. To lowest order, the tree-level vertex functional is given by:

$$\Gamma^0[A, \Psi, \bar{\Psi}, \omega, \omega^*] = \int d^4x \mathcal{L}_{\mathrm{eff}}. \tag{2.19}$$

[1] Each propagator is accompanied by a factor $\hbar$, each vertex by $\hbar^{-1}$ and the number of loops is given by $L = I - V + 1$, where I is the number of internal lines and V the number of vertices.

In perturbation theory one uses Feynman rules to construct graphs representing the considered process. The vertices (propagators) are just the (inverse) tree level vertex functions, Fourier transformed to momentum space and can therefore directly be read off the effective Lagrangian.

In covariant gauge (2.11), the propagator of a massless vector boson is given by:

$$i\Delta^{ab}_{F,\mu\nu} = \frac{-i\delta^{ab}}{p^2 + i\epsilon}\left(g_{\mu\nu} - (1-\xi)\frac{p_\mu p_\nu}{p^2}\right) \tag{2.20}$$

Here, ab are possible group indices and ϵ is an infinitesimal positive parameter inserted to preserve causality. It is obvious that for massless vector bosons as in $U(1)_{\mathrm{QED}}$ and $SU(3)_{\mathrm{QCD}}$, the additional gauge choice $\xi = 1$, the 't Hooft-Feynman gauge, is convenient for our calculations. Especially the structure of the denominator is simplest in this gauge and will not lead to further singularities of the integrand, which will be discussed later. There is one further gauge which should be mentioned at this place - the axial gauge, defined by:

$$f^a = n \cdot A^a, \tag{2.21}$$

with a fixed four-vector n. In this gauge the Faddeev-Popov determinant (2.9) is independent of the gauge field A and can therefore be pulled out of the path integral. Then, like for Abelian theories there is no need for the introduction of ghost fields in this gauge. The axial gauge has the further advantage of a physical propagator carrying only two polarizations in the limit $p^2 \to 0$, e.g. cf. [20]:

$$i\Delta^{ab}_{F,\mu\nu} = \frac{-i\delta^{ab}}{p^2 + i\epsilon}\left(g_{\mu\nu} - \frac{n_\mu p_\nu + p_\mu n_\nu}{np} + \frac{n^2 + \xi p^2}{(np)^2} p_\mu p_\nu\right). \tag{2.22}$$

In its form given in [4] it vanishes if multiplied by p^μ. Because of this, the virtual collinear singularities which we will discuss in chapter 3, are suppressed considerably. However, due to the structure of the denominator of the propagator in axial gauge, new singularities at $n \cdot p = 0$ appear.

In the case of electroweak symmetry breaking, a conventional choice for the gauge fixing function is:

$$f^a = \partial^\mu A^a_\mu + \xi e v \Phi, \tag{2.23}$$

with e being the electric charge, v the vacuum expectation value of the scalar Higgs and Φ the Goldstone boson. This choice avoids cross terms of the gauge and the Goldstone boson fields. In this R_ξ gauge, the propagators of the Goldstone bosons and the gauge field read:

$$i\Delta^{\Phi} = \frac{i}{p^2 - \xi M^2 + i\epsilon} \tag{2.24}$$

$$i\Delta^{A} = \frac{-i}{p^2 - M^2 + i\epsilon}\left(g_{\mu\nu} - (1-\xi)\frac{p_\mu p_\nu}{p^2 - \xi M^2}\right) \tag{2.25}$$

With this gauge fixing functional, also the ghost fields acquire a mass of $\sqrt{\xi}M$. Taking $\xi \to \infty$ leads to the so-called unitary gauge. Unphysical fields, the Goldstone bosons as well as the Faddeev-Popov ghosts become infinitely massive and decouple off the dynamics. However, this gauge is usually only used in Born level calculations, since the propagators are proportional to $\frac{p_\mu p_\nu}{p^2}$ for $p \to \infty$ and can therefore lead to numerical instabilities in loop calculations.

For the suggested method of loop integral evaluations, we will always use gauges with the simplest structure in the denominator. Thus, in all cases discussed above, we will set $\xi = 1$. This will simplify the analysis of the singularity structure of the integrands, on the other hand Feynman graphs with unphysical particles like Faddeev-Popov ghosts will have to be evaluated in addition. For the electroweak standard model, the number of Feynman rules is rather high and we will not list them explicitly in this thesis. For t' Hooft-Feynman gauge, they can be found in [21].

2.3. Renormalization

The Lagrangian of a gauge theory involves a certain number of free parameters like masses and couplings. When processes are calculated at tree level the bare parameters of the Lagrangian equal the physical quantities. However, when quantum corrections to these processes resulting from loop diagrams are taken into account, this relation is destroyed. The bare parameters cannot be interpreted as the physical ones. Furthermore, the shift between bare and physical parameters becomes infinite. Therefore, a redefinition of the parameters is necessary when computing higher order corrections. This is done by adding or multiplying renormalization constants to the bare parameters and also the fields. These constants also have to absorb the divergences occurring in loop calculations. A theory in which these divergences can be absorbed by a finite number of renormalization constants to all order in perturbation theory, and therefore can give meaningful predictions, is called renormalizable. For spontaneously broken non-Abelian gauge theories this renormalizability was shown in general R_ξ gauges [22–26].

One commonly seen procedure is multiplicative renormalization. Here, a set of independent parameters of the Lagrangian is chosen and each of this bare parameters as well as each field is re-expressed by the renormalized parameter or field multiplied by a renormalization constant Z_i^n. This constant can be split up in $Z_i = 1 + \delta Z_i$. As an example in QED we have:

$$A_0^\mu = \sqrt{Z_A} A^\mu \tag{2.26}$$
$$\Psi_0 = \sqrt{Z_\Psi}\Psi \tag{2.27}$$
$$m_0 = Z_m\, m = m + \delta m \tag{2.28}$$
$$e_0 = Z_e\, e = e + \delta e \tag{2.29}$$
$$\xi_0 = Z_\xi \xi \tag{2.30}$$

The field renormalizations are not necessary to obtain finite S matrix elements. However, they are needed to absorb the divergences in Green functions and vertex functions. Furthermore, in the electroweak standard model mass matrices acquire non zero off-diagonal entries due to radiative corrections. Here, renormalization constant matrices are required to rotate the bare fields onto the mass eigenstates. The on-shell renormalization scheme, introduced in the following, makes use of the masses of all physical particles, including the quark mixing matrix, and the electric charge e. Using experimental values for these parameters, all other parameters can be derived from those.

Renormalization Conditions

There is always a freedom of adding a finite part to the renormalization constants. Therefore, these have to be fixed by imposing renormalization conditions. Throughout this thesis we will use the widely used *on-shell* renormalization scheme [27], which is specified by the following conditions on the n-point vertex functions:

$$\text{Re } i\Gamma^{(2)}_{\alpha\beta}(-p,p)\Phi^{\beta}(p)\Big|_{p^2=m^2} = 0 \tag{2.31}$$

$$\text{Res}\left(-\Gamma^{(2)}(p)\right)^{-1}_{\not{p}=m,p^2=m^2} = 1 \tag{2.32}$$

$$\Gamma^{(3)}(p_i,\lambda)\Big|_{p_i^2=m^2} = \lambda_0^3 \tag{2.33}$$

$$\Gamma^{(4)}(p_i,\lambda)\Big|_{p_i^2=m^2} = \lambda_0^4, \tag{2.34}$$

where $\Phi(p)$ is the corresponding wave function for the external particle, e.g. $\epsilon^{\nu}(p)$ or $u(p)$, and α,β possible Lorentz or Dirac indices. The λ_i are the tree level vertex functions, e.g. $\lambda_0^3 = ie\gamma_\mu$ in QED. The first two conditions require the real parts of propagators to become singular at the physical mass, with residue unity to any order in perturbation theory. The latter two will fix the couplings to physical parameters. This scheme has the advantage that it directly relates the input parameters to experimentally measured values. However, in the case of QCD, where experimental results are obtained from hadrons rather than quarks and gluons, other schemes, like $\overline{MS}$ may be preferable.

In the case of the electroweak standard model a further condition can be imposed which removes possible tadpoles in calculations, by keeping the Higgs vev equal to the physical value to any order in perturbation theory, $v^2 = \frac{4\mu^2}{\lambda}$. Here, the first renormalization condition (2.31) also includes two point functions of different particles. The field renormalization constants of the two neutral gauge bosons and the quark fields are matrix valued. Condition (2.31) determines the off diagonal elements such that the two point functions vanish if one of the external particles is on-shell. A more detailed description can for example be found in [21].

Usually, the renormalization conditions (2.31-2.34) are used to relate and fix all of the renormalization constants. By eliminating all redundancies from the renormalization con-

ditions, one ends up with only a handful of constants with rather simple analytic expressions. These are sufficient to renormalize any diagrams in perturbation theory. Technically, one analytically evaluates primitively divergent vertex functions[2] by introducing a UV-regulator, rendering the loop integral finite. Examples for this additional parameter are a UV cutoff Λ, a parameter ϵ, reducing the dimension of the loop integral from 4 to $D = 4-\epsilon$ or the introduction of an additional vector boson propagator with a large mass Λ_{PV}. The analytic result of the loop integral then depends on this regulator, and becomes infinite in the limit $\Lambda \to \infty$ or $\epsilon \to 0$. The renormalization constants then will also depend on the regulator, whereas the final results for S matrix elements will not - the original divergences will be canceled by the counterterms containing the renormalization constants. However, great care has to be taken when regulating loop integrals. The introduction of a regulator might destroy some symmetries of the original Lagrangian, e.g. the violation of Lorentz symmetry by a UV cutoff Λ. For non-Abelian gauge theories, the generating functional of Green functions (2.1) obeys an extended gauge symmetry, the BRST symmetry. This translates to equations of motion for the Green function, the so-called Slavnov-Taylor identities, and in the case of vertex functions Lee identities. Dimensional regularization fulfills these identities and preserves Poincaré symmetry as well as global internal symmetries, however cancellations of divergences will take place between different graphs of a process.

In this thesis, we will not make use of the renormalization constants introduced in the way above. Although they are a simple and efficient tool to analytically renormalize and evaluate one loop graphs, they are of minor use in numerical applications. In the following we will propose a scheme, where for each graph subtraction graphs fulfilling the renormalization conditions can directly be found by a simple prescription.

2.4. BPHZ Prescription

Since we are aiming for a fully automated numerical evaluation of processes, we do not want to introduce an unphysical regulator. Although in full processes the dependence of the results on this regulator cancels in the associated limit, we still would have to assign a finite value to it. An error estimate of the numerical results would become difficult and cancellations between very large numbers would occur, which could lead to numerical instabilities. Furthermore, we want to calculate infrared divergent real emission graphs under the same integral, although they have a reduced number of loops. These arguments eliminate dimensional regularization as a possible regularization scheme for loop calculation with the Feynman Tree Theorem. We will therefore choose a BPHZ scheme of regularization, which renders loop integrals finite before integration.

This alternative procedure to the renormalization of masses, couplings and fields was prescribed by Bogoliubov and Parasiuk [28] and later Hepp and Zimmermann [29]. Consider a graph Γ. Bogoliubov's R operation is defined as

[2] By *primitively divergent*, it is referred to those vertex functions whose superficial degree of divergence $\omega(\Gamma)$ (2.39) is not negative.

$$\mathrm{R}(\Gamma) = \Gamma + \sum_{\{\gamma_1,\ldots,\gamma_n\}} \Gamma_{\gamma_i \to C(\gamma_i)} \tag{2.35}$$

Here, the γ_i indicate 1PI subgraphs of Γ and the sum runs over all possible ways of surrounding the graph Γ and/or its 1PI subgraphs γ_i by nested but not overlapping boxes, sometimes called *forests*. The prescription $\gamma_i \to C(\gamma_i)$ replaces the subgraph γ_i by its counterterm $C(\gamma_i)$:

$$C(\gamma_i) = -T \circ \mathrm{R}'(\gamma_i), \tag{2.36}$$

where T is an operation which extracts the divergent part of its argument. R' is again the R operation (2.35), except the sum running now over all forests except the one which would produce a counterterm for the whole 1PI subgraph, since its divergent part is extracted by (2.36) and removed by (2.35):

$$\mathrm{R}'(\gamma_i) = \gamma_i + \sum_{\{\gamma'_1,\ldots,\gamma'_n\} \cap \{\gamma_i\}} \gamma_{i\,\gamma'_j \to C(\gamma'_j)} \tag{2.37}$$

Thus, the R-operation is a recursive operation, starting at the 1-loop 1PI subgraphs and then going to higher loops in all possible ways until finally the last divergence is absorbed by the final R-operation on the whole graph Γ. It has been proven by Zimmermann that this prescription eliminates all divergences of a Feynman integral to all orders in perturbation theory.

T Operation

The T-operator in (2.36) may be any operation which extracts the divergent part of its argument. It therefore determines the renormalization scheme. In dimensional regularization it can be chosen to be, e.g. cf. [30]:

$$T \circ \gamma = \text{pole part in } \epsilon, \tag{2.38}$$

defining the MS scheme. As mentioned above, we want to use the on-shell renormalization scheme. A suitable definition for the T-operation is a Taylor expansion of Γ around some fixed external momenta. We define the *superficial degree of divergence* of a one loop graph $\omega(\Gamma)$ as:

$$\omega(\Gamma) = 4 - E_S - E_V - \frac{3}{2} E_\Psi - d(\Gamma), \tag{2.39}$$

where E_X is the number of external scalars (including ghosts), vector-bosons (in 't Hooft-Feynman gauge, $\xi = 1$) and fermions of Γ and $d(\Gamma)$ the minimal number of external momenta coming from derivative couplings. This formula results from power counting of propagators and vertices with derivative couplings in loop integrations. The superficial degree of divergence reflects the behavior of a loop integration in the limit of loop momentum $q \to \infty$. If $\omega(\Gamma) \geq 0$, the integral diverges. When differentiating Γ with respect to an external momentum, the superficial degree of divergence lowers by one. Therefore, any loop integral can be made finite by a sufficient number of derivatives ($\omega(\Gamma) + 1$) with

respect to the external momenta and the divergent part is a polynomial in external momenta of degree $\omega(\Gamma)$. One could ascribe this polynomial to a further vertex term in the Lagrangian with corresponding derivative couplings. This is done in multiplicative renormalization. Note that renormalizability requires masses and couplings of positive mass dimensions. This lead to (2.39) and from this one would deduce further renormalizable (counter-) terms in the Lagrangian. Thus, in renormalizable theories only a few counterterms are necessary to absorb all divergences in perturbation theory and the inclusion of all possible renormalizable terms allowed by symmetry in the Lagrangian might be necessary.

Consider a 1PI one loop graph $\Gamma^n(p_1,\dots,p_n)$ with superficial degree of divergence $\omega(\Gamma)$. We define the T operator as a Taylor expansion around on-shell momenta $\bar{p}_i$, with $\bar{p}_i^2 = m_i^2$:

$$\begin{aligned} T\circ\Gamma^n(p_1,\dots,p_n) &= \Gamma^n(\bar{p}_1,\dots,\bar{p}_n) + \sum_i^{n-1}(p_i-\bar{p}_i)^\mu \left.\frac{\partial\Gamma^n}{\partial p_i^\mu}\right|_{p_1=\bar{p}_1,\dots,p_n=\bar{p}_n} + \\ &\quad \cdots + \\ &\quad \frac{1}{d!}\sum_{i_1,\dots,i_d}^{n-1}(p_{i_1}-\bar{p}_{i_1})^{\mu_1}\dots(p_{i_d}-\bar{p}_{i_d})^{\mu_d}\left.\frac{\partial^d\Gamma^n}{\partial p_{i_1}^{\mu_1}\dots\partial p_{i_d}^{\mu_d}}\right|_{p_1=\bar{p}_1,\dots,p_n=\bar{p}_n}, \end{aligned} \tag{2.40}$$

up to $d=\omega(\Gamma)$. With this T operator, the renormalized 1PI n-point functions

$$\hat{\Gamma}^n(p_1,\dots,p_n) = \Gamma^n(p_1,\dots,p_n) - T\circ\Gamma^n(p_1,\dots,p_n) \tag{2.41}$$

fulfill the renormalization conditions (2.31-2.34). Note that we consider the external four-vectors in Minkowski space and not Euclidean, which is commonly used in schemes derived from the BPHZ prescription. In our formulation, the subtraction terms derived from (2.40) can be complex valued. However, only the real part is needed for renormalization. For two loop calculations, it therefore might be necessary to further restrict the subtraction terms to be the real parts of the considered graphs.

Renormalization of One Loop Vertex Functions in QED

As an example we will discuss the three primitively divergent vertex functions of QED. The electron two point function (up to one loop order) can be decomposed into Lorentz covariants:

$$\Gamma^{ee}(p) = i(\not{p}-m) + i\Sigma^{ee}(p) = i(\not{p}-m) + i\not{p}\Sigma_V^{ee}(p^2) + im\Sigma_S^{ee}(p^2). \tag{2.42}$$

We choose an on-shell momentum $\bar{p}_\mu$ with spatial component equal to the original momentum $\vec{p}$ flowing through the vertex:

$$\bar{p} = (E_{\vec{p}},\vec{p}), \quad E_{\vec{p}} = \sqrt{\vec{p}^2+m^2}. \tag{2.43}$$

T operation on the divergent one loop part of (2.42) yields:

$$\begin{aligned} T \circ \Sigma^{ee}(p) &= i\not{p}\Sigma_V^{ee}(m^2) + im\Sigma_S^{ee}(m^2) \\ &\quad + i(\not{p} - \not{\bar{p}})\Sigma_V^{ee}(m^2) + 2i(p-\bar{p})^\mu \bar{p}_\mu \left[\not{p}\Sigma_V^{ee\prime}(m^2) + m\Sigma_S^{ee\prime}(m^2)\right]. \end{aligned} \tag{2.44}$$

Thus, the renormalized electron self-energy reads:

$$\begin{aligned} i\hat{\Sigma}^{ee}(p) &= i\not{p}\left(\Sigma_V^{ee}(p^2) - \Sigma_V^{ee}(m^2)\right) + im\left(\Sigma_S^{ee}(p^2) - \Sigma_S^{ee}(m^2)\right) \\ &\quad -2i(p\bar{p} - m^2)\left[\not{p}\Sigma_V^{ee\prime}(m^2) + m\Sigma_S^{ee\prime}(m^2)\right]. \end{aligned} \tag{2.45}$$

And the electron two point function is

$$\hat{\Gamma}^{ee}(p) = i(\not{p} - m) + i\hat{\Sigma}^{ee}(p). \tag{2.46}$$

The renormalization condition (2.31) imposed on (2.46) gives:

$$\text{Re } i\hat{\Gamma}^{ee}(p)u(p) \stackrel{!}{=} 0 \quad \rightarrow \quad \text{Re } \hat{\Sigma}^{ee}(p)u(p) \stackrel{!}{=} 0, \tag{2.47}$$

which is clearly fulfilled if $p^2 = m^2$, which also implies $p \rightarrow \bar{p}$. The second renormalization condition translates into

$$\lim_{p^2 \rightarrow m^2} \frac{i}{\not{p} - m} \text{Re } \hat{\Sigma}^{ee}(p)u(p) \stackrel{!}{=} 0 \tag{2.48}$$

Using Dirac's equation $\not{p}u(p) = mu(p)$ we have

$$\begin{aligned} \lim_{p^2 \rightarrow m^2} \Bigg[&\frac{2m^2}{p^2 - m^2}\left(\Sigma_V^{ee}(p^2) - \Sigma_V^{ee}(m^2) + \Sigma_S^{ee}(p^2) - \Sigma_S^{ee}(m^2)\right) \\ &- 4m^2 \frac{p\bar{p} - m^2}{p^2 - m^2}\left(\Sigma_V^{ee\prime}(m^2) + \Sigma_S^{ee\prime}(m^2)\right)\Bigg] u(p) \stackrel{!}{=} 0. \end{aligned} \tag{2.49}$$

Taking the limit $p^2 \rightarrow m^2$ in the first line gives just the derivatives of the self energies. The crucial factor in the second line is:

$$\frac{p\bar{p} - m^2}{p^2 - m^2} = \frac{(\bar{p} + \Delta)\bar{p} - m^2}{(\bar{p} + \Delta)^2 - m^2} = \frac{\bar{p}\Delta}{2\bar{p}\Delta + \Delta^2}, \tag{2.50}$$

where we replaced p_μ by $(\bar{p} + \Delta)_\mu$, $\Delta_\mu = (\delta, 0)$. Taking the limit $\delta \rightarrow 0$ yields a factor $\frac{1}{2}$. Therefore the expression vanishes and the second renormalization condition is fulfilled.

The BPHZ procedure provides subtraction terms, which are easily interpreted as additional graphs. In the case of a photonic correction to an electron propagator, we just subtract the same graph at a new momentum $\bar{p}$ flowing through the propagator as well as the same graph with an additional insertion of a Dirac valued factor $(\not{p} - \not{\bar{p}})$ in the fermion line of the loop, which is equivalent to the derivative of the electron self-energy. This is depicted in figure 2.1. Note that the derivative term is infrared divergent. This divergence

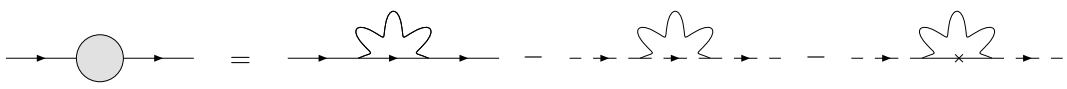

Figure 2.1: Renormalization of the 1-loop electron self-energy: From the unrenormalized loop correction, we subtract the same graph at on-shell external momentum (dashed) as well as the derivative with respect to the external momentum. This results in an insertion of a Dirac gamma matrix, indicated by $\times$.

will be absorbed by the subtraction graphs of the two adjacent vertex corrections. We will discuss the procedure in detail in section 3.3. For one loop calculations, we do not have to worry about additional imaginary contributions from the subtraction graphs, since we only evaluate the real part numerically. For higher loop calculations, we will only consider the real part of the subtraction terms.

The renormalization of the photon self-energy $\Sigma^{AA}(p)$ is rather involved and does not lead to simple subtraction graphs, since we have to take two derivatives. We give the calculation in appendix B in the language of scalar integrals, which we will briefly introduce in the next section. It turns out that the final result is fairly simple, and factors out of the Lorentz and Dirac structure of the graphs. It is also infrared finite and can therefore be interpreted as a global correction factor to the tree level amplitude which can easily be implemented in the numerical calculations.

The last primitively divergent vertex function of QED is the vertex correction $\Gamma_\mu^{\bar{\Psi}A\Psi}(p,-p')$. Since its superficial degree of divergence is $\omega(\Gamma_\mu^{\bar{\Psi}A\Psi}) = 0$, we only have to subtract the same graph at $p^2 = p'^2 = m^2$, $p = -p'$ as in the definition of the electric charge in the Thomson limit. The UV divergence is independent of the external momenta, so we can freely choose the spatial parts. To cancel IR divergences we have to subtract the same graph once at $\Gamma_\mu^{\bar{\Psi}A\Psi}(p,-p)$ and once at $\Gamma_\mu^{\bar{\psi}A\Psi}(p',-p')$, with $p^2 = m^2$ and $p'^2 = m^2$, correspondingly. This will also be discussed in section 3.3. In figure 2.2 we depicted the mechanism of renormalization of this three point function.

QED Ward Identities

In QED, there is a one to one correspondence between the subtraction terms of our BPHZ procedure and the counterterms obtained with multiplicative renormalization[3]. Here, the Ward identities are fulfilled for renormalized quantities if dimensional regularization is used, which preserves local gauge invariance. Since we do not introduce a further regulator, but evaluate the expressions of the bare quantities and the corresponding counterterms simultaneously, the Ward identities are automatically fulfilled. If the one to one correspondence is also present in the case of non-Abelian theories, we also do not have to worry about the constraints imposed by the Slavnov-Taylor identities. A rigorous proof is still

[3]For a thorough list of counterterms in terms of self energies, cf. [21]

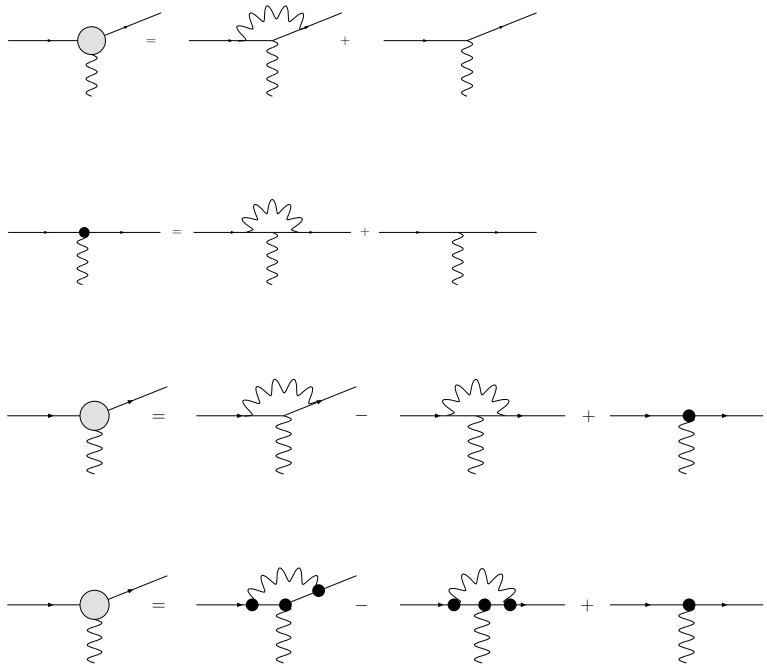

Figure 2.2: Renormalization of the QED vertex correction: The first line shows the unrenormalized vertex correction up to one loop in perturbation theory. In the second line we depicted the definition of the electric charge in the Thomson limit $p_\gamma \to 0$, indicated by the straight fermion lines. Substituting the born vertex in line 1 by this definition yields line 3. By taking the experimental value of the electric charge at each vertex, the inflicted error is then of second order in perturbation theory.

missing and will not be the subject of this thesis. Nevertheless, in critical cases, one can always switch back to renormalization and regularization schemes preserving the identities. As mentioned above, we already use this hybrid ansatz in the case of the infrared finite corrections to the photon propagator, since here the use of an algebraic reduction to scalar integrals is much more efficient.

Extension to Electroweak Standard Model

In the case of the electroweak standard model, two point functions with different external particles can arise and the BPHZ prescription has to be extended for their incorporation. In case of the ZA vertex, one can use the simple subtraction prescription:

$$\hat{\Sigma}^{AZ}_{\mu\nu}(p) = \Sigma^{AZ}_{\mu\nu}(p) - \frac{p^2}{M_Z^2}\Sigma^{AZ}_{\mu\nu}(\bar{p}_Z) + \frac{p^2 - M_Z^2}{M_Z^2}\Sigma^{AZ}_{\mu\nu}(\bar{p}_0), \tag{2.51}$$

where $\bar{p}_i = a_i p_i$ with $a_i^2 = \frac{m_i^2}{p_i^2}$. This is equivalent to results obtained with multiplicative

renormalization, cf. [21]. Note that in the limit of $M_Z \to 0$ we obtain the result (B.10) for the renormalized photon self-energy. Since no infrared divergences are encountered in these two point functions, we could also use a representation in terms of scalar integrals and follow the same line as in the appendix B for the renormalization of the two photon vertex. This is also true for off-diagonal two point function involving quark fields.

2.5. Calculation of Cross Sections

In this section, we will introduce the ingredients of cross section calculations. We will give a short overview of different methods of evaluating loop integrals and briefly discuss the approaches of different groups aiming at an automatized generation and evaluation of loop order processes. We will also introduce the helicity formalism used in O'MEGA◇WHIZARD [17, 31, 32] for matrix element creation and event generation.

The cross section of a $2 \to n$ scattering event is given by:

$$\begin{aligned} d\sigma &= \Phi \, d\Pi_n(P; q_1, \ldots, q_n) \, |\mathcal{M}(p_1, p_2 \to q_1, \ldots, q_n)|^2 && (2.52) \\ \Phi &= \frac{1}{2E_1 2E_2 |v_a - v_b|} && (2.53) \\ d\Pi_n(P; q_1, \ldots, q_n) &= \prod_f \frac{d^3 q_f}{(2\pi)^3 2E_f} (2\pi)^4 \delta^{(4)}(P - \sum q_f), && (2.54) \end{aligned}$$

with $P = p_1 + p_2$, the kinematic flux factor Φ and the n-particle phase space $d\Pi_n$. The Lorentz transformation property of the cross section is solely given by the flux factor. Performing the integration over the phase space will lead to the total cross section. The dynamics of the scattering event is incorporated in the matrix element $\mathcal{M}$. Up to one loop order in perturbation theory we write for the matrix element with n final state particles:

$$\mathcal{M}_n = \mathcal{M}_n^{\text{Born}} + \mathcal{M}_n^{\text{loop}}. \tag{2.55}$$

The leading order total cross section is then given by:

$$\sigma^{(0)} = \Phi \int d\Pi_n \, |\mathcal{M}_n^{\text{Born}}|^2. \tag{2.56}$$

Some of the graphs contributing to the matrix element $\mathcal{M}^{\text{loop}}$ will be UV divergent. In the following we will write the contributions of the subtraction diagrams explicitly as $\mathcal{M}_{\text{CT}}^{\text{loop}}$. The loop contribution to the cross section in first order of perturbation theory is then given by the interference term of the one loop with the Born matrix elements:

$$\sigma_v^{(1)} = \Phi \int d\Pi_n \, 2 \, \text{Re}(\mathcal{M}^{\text{Born}} (\mathcal{M}_n^{\text{loop}} + \mathcal{M}_{n,\text{CT}}^{\text{loop}})^*) \tag{2.57}$$

The matrix elements $\mathcal{M}_n^{\text{loop}}$ and $\mathcal{M}_{n,\text{CT}}^{\text{loop}}$ can also be infrared divergent, which is the case if massless gauge bosons like photons and gluons are exchanged between external on-shell

particles. Physically, an initial or final state particle state cannot be distinguished from a state with an additional number of soft photons. It was pointed out by Kinoshita [33], Lee and Nauenberg [34] that the sum over all degenerate initial and final states is infrared safe in each order of perturbation theory. In the case of QED corrections this means that if the Born cross section of the real emission process $\sigma(1)_{\text{re}}$with n particles and an additional photon in the final state is added to the virtual cross section $\sigma_v^{(1)}$ the resulting total cross section is finite [35]. Assuming that the detector cannot resolve photons of energy less than ΔE_s, one can split up the real emission cross section, which is of the same order in perturbation theory than the virtual cross section, into a soft and a hard part,

$$\sigma_{\text{re}}^{(1)} = \sigma_{\text{soft}}^{(1)}(\Delta E_s) + \sigma_{\text{hard}}^{(1)}(\Delta E_s) \tag{2.58}$$

$$\sigma_{\text{soft}}^{(1)}(\Delta E_s) = \Phi \int d\Pi_n \int^{\Delta E_s} \frac{d^3k}{(2\pi)^3 2E_k} |\mathcal{M}_{n+\gamma}^{\text{Born}}|^2 \tag{2.59}$$

$$\sigma_{\text{hard}}^{(1)}(\Delta E_s) = \Phi \int\limits_{E_k \geq \Delta E_s} d\Pi_{n+\gamma} |\mathcal{M}_{n+\gamma}^{\text{Born}}|^2 \tag{2.60}$$

and add the soft part to $\sigma_v^{(1)}$. The usual procedure to cancel the divergent contributions is to evaluate the soft real emission cross section analytically in the so called soft photon approximation with a small photon mass λ. Here, the cross section can be written as the Born cross section of the $2 \to n$ process times a prefactor which can be integrated analytically. In the added result the dependence on the photon mass λ then drops out.

In the next chapter we will introduce a method to evaluate loop diagrams which reduces the loop integration to a phase space integration. The former loop graphs split into a sum of tree graphs with an additional initial and final state particle over which the phase space integration is performed. Thus, in first order of perturbation theory, the virtual cross section, including the contribution of the soft real emission part, can be written as:

$$\sigma_v^{(1)}(\Delta E_s) = \Phi \int d\Pi_n \int \frac{d^3k}{(2\pi)^3 2E_k} 2\text{Re}(\mathcal{M}_n^{\text{Born}}(\mathcal{M}_{n+1}^{\text{Tree}} + \mathcal{M}_{n+1,\text{CT}}^{\text{Tree}})^*) + |\mathcal{M}_{n+\gamma,\text{soft}}^{\text{Born}}(\Delta E_s)|^2, \tag{2.61}$$

and $\mathcal{M}_{n+\gamma,\text{soft}}^{\text{Born}}(\Delta E_s)$ is understood to be the real emission matrix element with an additional theta function cutting out the soft part. Written in this way, the integrand is ultraviolet and infrared finite before integration and in principle there is no need for any regulator. One can also add the Born cross section to the integrand as a constant divided by the integration volume. The full fixed order next to leading order (NLO) cross section is then given by:

$$\sigma^{\text{NLO}} = \sigma^{(0)} + \sigma_v^{(1)}(\Delta E_s) + \sigma_{\text{hard}}^{(1)}(\Delta E_s). \tag{2.62}$$

Here, the first two terms are $2 \to n$ processes, while $\sigma_{\text{hard}}^{(1)}(\Delta E_s)$ is a $2 \to n+1$ process. Ideally, in the sum the total cross section does not depend on the cutoff ΔE_s anymore.

In practice, often an approximation is used to incorporate the soft real radiation in the virtual part, which will be shown in chapter 3. In this thesis, we will mainly focus on the $2 \to n$ part, which in the form of equation (2.61) is very well suited for Monte Carlo integration and event generation, cf. chapters 5 and 6.

Helicity Amplitudes

Besides the denominator resulting from propagators, a typical amplitude consists of several fermion chains with Dirac and Lorentz indices. When multiplied with another amplitude the sum over Dirac indices results in traces of chains of Dirac Gamma matrices. These can simply be reduced and evaluated by algebraic programs. The final expressions then consist of terms of scalar products of momenta of the amplitudes. This procedure can give simple expressions, however, when considering scattering processes with many particles in the final states, the number of terms rises drastically when each product of two amplitudes is calculated separately. Often, it is therefore more efficient to calculate single amplitudes, sum up the values for all different amplitudes and take the product afterwards. This can be done in terms of helicity amplitudes, where each amplitude is just a unique complex number in a basis given by helicity eigenstates of the spinor and bosonic wave functions. The evaluation of single amplitudes has the further advantage that amplitudes for different processes like for example the production of instable particles and their subsequent decay factorize and can be calculated separately. The whole process is then the product of the two amplitudes summed over the helicities of the intermediate particle. This takes also interference effects into account contrary to the simple product of the cross sections for particle production and the decay width. To calculate helicity amplitudes, we will use the matrix element generator O'MEGA [17]. The conventions used for the helicity eigenstates are listed in appendix A.2.

Reduction of Tensor Integrals

For one loop integrals there exists a systematic method to reduce tensor valued integrals to scalar integrals, which can analytically be evaluated rather easily. This method was introduced by Passarino and Veltman [36]. Since we will use it for the evaluation of the one loop photon self-energy, we will briefly introduce it in the following. Any one loop graph can be decomposed into a sum of tensor integrals $T^N_{\mu\nu\ldots}$ multiplied with Lorentz valued coefficients which are independent of the integration momentum. These tensor integrals can be written in D dimensions as:

$$T^{(N)}_{\mu\nu\ldots} = \frac{(2\pi\mu)^D}{i\pi^2}\int d^D k \frac{k_\mu k_\nu \ldots}{\left[k^2 - m_0^2 + i\epsilon\right]\left[(k+p_1)^2 - m_1^2 + i\epsilon\right]\ldots\left[(k+p_{N-1})^2 - m_{N-1}^2 + i\epsilon\right]}. \tag{2.63}$$

Usually, $T^{(N)}$ is replaced by the N-th character of the alphabet. The tensor integrals are Lorentz covariants and can therefore be decomposed into Lorentz tensors composed of the external momenta $p_{\mu,i}$ and the metric $g_{\mu\nu}$ times a scalar coefficient. For example, the two-point tensor integral $B_{\mu\nu}$ can be written as:

$$B_{\mu\nu}(p, m_0, m_1) = g_{\mu\nu} B_{00}(p^2, m_0, m_1) + p_\mu p_\nu B_{11}(p^2, m_0, m_1). \tag{2.64}$$

This equation can be inverted to get equations for the scalar coefficients B_{00} and B_{11}. These can be obtained by multiplying (2.64) with the metric and external momenta, substituting

$$kp = \frac{1}{2}\left[(k+p)^2 - m_1^2\right] - \frac{1}{2}\left[k^2 - m_0^2\right] - \frac{1}{2}(p^2 - m_0^2 + m_1^2), \tag{2.65}$$

and replacing the original integral by a sum of integrals with a lower rank and equal or less propagators. Doing this iteratively, one ends up with a sum of scalar integrals, which can be evaluated analytically.

The inversion of the linear equations for the decomposition into Lorentz covariants involves a determinant of external momenta. This Gram determinant vanishes for linearly dependent momenta. From five point functions on, this can happen within the phase space and one therefore has to take great care in the reduction to scalar integrals. Except for the two point functions of the photon self-energy, we will not make use of any reduction scheme in this thesis and therefore do not encounter this determinant. For alternative reduction schemes avoiding a small determinant, cf. [37] and references therein.

Feynman Parameterization

A commonly seen method of evaluation of the scalar integrals is the usage of Feynman parameters. Here, the product of propagators is replaced by an integration of a simple polynomial in the denominator over additional parameters:

$$\frac{1}{A_1 \dots A_n} = (n-1) \int \prod_i^n dx_i \frac{\delta(1 - \sum x_i)}{\left(\sum x_i A_i\right)^n}. \tag{2.66}$$

The integration over the loop momentum can then easily be performed after completing the square and rotation to Euclidean coordinates. It remains to evaluate the integrals over the Feynman parameters.

Different Approaches to Evaluation of Loop Integrals

The calculation of higher order cross sections is a highly active field of theoretical particle physics. In this section we will give a brief overview of the main approaches and tools used for the evaluation of loop integrals and the extraction of infrared singularities. For recent more detailed overviews of different techniques and further references, cf. [38, 39].

Mellin-Barnes Integration

In the case of two- or higher loop corrections, the simple reduction method of Passarino and Veltman cannot be applied anymore. By making use of the Poincaré invariance of loop integrals one can find integration by parts identities as well as Lorentz invariance identities to reduce the amount of integrals involved in a multi loop calculation to a small

set of master integrals. There exist automated routines which implement an algorithm for this reduction [40].

It then remains to evaluate the set of master integrals. In the past years, substantial progress was made in analytical and numerical evaluations with Mellin-Barnes representations [41, 42]. Here the loop integrals in Feynman parameterization are represented as complex contour integrals:

$$\frac{1}{(A+B)^{\nu}} = \frac{1}{2\pi i} \int\limits_{c-i\infty}^{c+i\infty} d\omega A^{\omega} B^{-\nu-\omega} \frac{\Gamma(-\omega)\Gamma(\omega+\nu)}{\Gamma(\nu)}. \tag{2.67}$$

Applying this representation iteratively on the integrands, one can then easily integrate over the Feynman parameters and the loop integral is finally represented as a multi dimensional complex contour integral. Infrared singularities localize on simple poles in the complex integration volume and can be extracted rather easily. After extraction of divergent pieces one can perform a Taylor expansion in the dimension parameter ϵ and numerically or analytically evaluate the coefficients of the series.

Clearly, it is favorable to have an analytic expression for the matrix element of a given process. However, the evaluation of a lengthy analytic expression might still take some time if harmonic functions and multiple polylogarithms are involved. A fully automated implementation in form of a universal event generator requires further essential developments of today's techniques. The amount of calculated master integrals is growing but still limited. Going to higher orders or multi leg processes might require additional techniques for the reduction to master integrals and their evaluation.

Sector Decomposition and Contour Deformation

One of the major problems which has to be overcome in loop calculations is the occurrence of singularities, like virtual IR or collinear peaks. Especially in the case of overlapping singularities, their extraction and the numerical evaluation of the integral is a non-trivial task. A method called sector decomposition was proposed in [43]. Here, the integration over Feynman parameter space is iteratively divided into sectors with a specific ordering of the integration variables. The singularities at the endpoints of the integration parameters factorize and can then be easily extracted.

Besides the infrared and collinear peaks, further threshold singularities can appear. One method of a numerical evaluation in presence of such singularities was proposed in [44]. Here, the integration over the Feynman parameters is analytically continued to the complex space and the contour deformed to avoid singular points. Combining sector decomposition and contour deformation gives a powerful tool to evaluate complicated multi loop diagrams, cf. [45]. However, the computational costs of the decomposition into sectors and the subsequent numerical evaluation can be very high. Furthermore, the proposed methods require strong algebraic manipulations of the expressions of the loop integrals,

which makes a fully automated matrix element creation and evaluation tedious.

A method for full numerical evaluations in QCD, with similarities to the one presented in chapter 3, was presented in [46–48]. To get numerical results for a loop integral, a sum over cuts of this loop is considered. To avoid scattering singularities, which arise from on-shell intermediate particles, a contour deformation is performed which analytically continous the loop momentum to imaginary space. Contrary to the contour deformation used in this method, we will show the construction of subtraction terms, which cancel internal on-shell singularities. In the final sampling of the integrand, no special emphasis has to be placed on these regions in phase space. Using real momenta, the method presented in this thesis allows for an immediate application to cross section integration and event generation.

Subtraction Methods and Phase Space Slicing

The infrared divergent parts of loop integrals are compensated by the infrared divergences of the corresponding real emission processes. However, in numerical calculations the integrals have to be convergent separately, if the two contributions are evaluated at two different stages. Primarily for QCD calculations, subtraction methods were developed [49–51], which add a term to the real emission process, rendering the phase space integral finite. The analytic integral of the term is known and can be subtracted from the divergent part of the loop calculation, such that this is also finite. Here, no approximation is needed to cancel the infrared divergent parts of the loop integrals, however an analytic expansion in the dimensional parameter still has to be performed.

To perform the phase space integration in real emission diagrams, often a method called phase space slicing is used. Here, the phase space is cut in parts by the parameters ΔE_s and θ_c, to separate the soft from the hard and the collinear from the non-collinear regime. The soft and collinear parts can then be evaluated analytically by appropriate approximations. In this way, one can also isolate the infrared divergent part and subtract it from the loop calculation.

In this thesis, we will make use of the above methods in the sense that we add the soft real emission diagrams to the integrands of the loops to render them finite before integration. We will discuss this in section 3.3.

Summary

In the preceding chapter we showed the embedding of gauge freedom in field theoretic quantities and motivated our choice of gauge, namely the t' Hooft-Feynman gauge, where gauge field propagators get a simple structure in the denominators. We further introduced the on-shell renormalization scheme and the BPHZ prescription to regularize UV divergent Feynman graphs. Finally, we discussed several techniques to evaluate loop diagrams. In the following chapters we will develop a method of loop integral evaluation, incorporating the proposed renormalization and regularization scheme and making use of subtraction terms to remove singular and divergent pieces of the integrand.

3. Feynman Tree Theorem

In this chapter we will develop a method to evaluate loop integrals from tree graphs. The starting point of this method is a theorem by Feynman [13, 52, 53][1]. The idea is to decompose loop propagators into advanced Green functions and a delta function. When integrating over the zero component of the loop momentum, the delta functions will put the internal momentum of the associated propagator on-shell. This has the effect of *opening* or *cutting* the loop. The Feynman Tree Theorem states, that a loop integral can be expressed as the sum of all possible cuts of its propagators. Terms with one cut propagator can be interpreted as tree level processes with an additional incoming and outgoing particle. The original integration over the loop momentum becomes a phase space integration for the additional particle. Operating on every loop diagram, a full one loop $m \to n$ matrix element can be rewritten as the coherent sum of all possible $m \to n + p + \bar{p}$ tree level processes with an additional integration over the phase space of the particle p and its corresponding antiparticle $\bar{p}$. Since tree level amplitudes can be created by automatic matrix element generators and phase space integrations are well under control for up to $2 \to 6$ processes [32], this method of evaluating loop integrals is ideally suited for implementation into a Monte Carlo event generation framework. A further advantage of the proposed method is that real emission diagrams can be evaluated under the same integral and infrared divergences can therefore be compensated before final integration. The same is true for the subtraction terms which will be constructed from the on-shell BPHZ scheme described in the previous chapter. Thus, all UV and IR divergences cancel before integration and the final results can be easily compared to experimental data. Furthermore, no additional algebraic manipulations have to be applied to the integrands, which again simplifies a future implementation in an event generator.

In the next section we will derive the method for one loop integrals. A path to a generalization to multi loop diagrams is shown in appendix D. The resulting integrand usually has a rich structure of peaks hampering the numerical evaluation. In section 3.2, we will discuss in detail the structure of possible peaks and show the construction of fix functions to smooth the peaks. In section 3.3, we will examine the infrared divergences and show their cancellation by addition of real emission graphs. The explicit construction of subtraction terms from the BPHZ prescription is shown. These have to cancel UV divergences as well as IR divergences from some of the associated real emissions. A detailed study of the collinear peaks is given at the end of this chapter.

[1] Here, the Tree Theorem was invented to invest the renormalizability of a quantum theory of gravitation. In [54], preliminary work towards a numerical evaluation of loop integrals in scalar theories was commenced.

3.1. Derivation of the Feynman Tree Theorem

In this section, we will first derive the Feynman Tree Theorem closely following [52][2]. We will then derive a new version of the Tree Theorem, which is better suited for a numerical integration. We will then discuss in detail the contributions and interrelations of the single terms appearing in this improved version.

The integrand $I(k)$ of a loop integral can be written as a product of Green functions G_{F} of the Klein-Gordon equation times a regular function $N(k)$ in the numerator. The latter may depend on the integration momentum k and have Lorentz and Dirac indices but is not of interest in the following. Suppressing the possible indices, we have

$$I(k) = N(k) \prod_i G_{\mathrm{F}}(k + p_i, m_i), \tag{3.1}$$

where the subscript F indicates the use of the Feynman prescription. The p_i are linear combinations of external momenta, the m_i the masses of the physical particle the propagator corresponds to. We define

$$\begin{aligned} F_i &\equiv G_{\mathrm{F}}(k + p_i, m_i) \\ &= \frac{i}{(k+p_i)^2 - m_i^2 + i\epsilon} \\ &= i \frac{1}{k^0 - (-p_i^0 + \sqrt{(\vec{k} + \vec{p_i})^2 + m_i^2} - i\epsilon)} \frac{1}{k^0 - (-p_i^0 - \sqrt{(\vec{k} + \vec{p_i})^2 + m_i^2} + i\epsilon)} \end{aligned} \tag{3.2}$$

Note that we only consider cases, where the k-dependence in the denominator of a propagator is of the form (3.2). As stated in section 2.2, we use 't Hooft-Feynman gauge, where gauge boson propagators take on this simple structure in the denominator.

In the following, we want to replace the Feynman Green functions F_i by advanced Green functions A_i, where both poles lie in the upper k^0-half plane. We define

$$E_i = \sqrt{(\vec{k} + \vec{p_i})^2 + m_i^2}. \tag{3.3}$$

Performing a partial fraction decomposition in (3.2), and similar for A_i, we get

$$F_i = \frac{i}{2(E_i - i\epsilon)} \left(\frac{1}{k^0 - (-p_i^0 + E_i) + i\epsilon} - \frac{1}{k^0 - (-p_i^0 - E_i) - i\epsilon} \right), \tag{3.4}$$

$$A_i = \frac{i}{2E_i} \left(\frac{1}{k^0 - (-p_i^0 + E_i) - i\epsilon} - \frac{1}{k^0 - (-p_i^0 - E_i) - i\epsilon} \right), \tag{3.5}$$

$$\Delta_i^l \equiv F_i - A_i = \frac{i}{2E_i} \left(\frac{1}{k^0 - (-p_i^0 + E_i) + i\epsilon} - \frac{1}{k^0 - (-p_i^0 + E_i) - i\epsilon} \right). \tag{3.6}$$

[2] A similar derivation can also be found in [55], where the Feynman Tree Theorem was used in the context of MHV amplitudes.

Here, we ignored the imaginary part in the prefactor of the Feynman Green function F_i. Being independent of k^0 it is not relevant in the following. Using a representation of the delta function

$$2\pi i\delta(u) = \lim_{\epsilon\to 0}\left(\frac{1}{u-i\epsilon} - \frac{1}{u+i\epsilon}\right), \tag{3.7}$$

the difference of the Feynman and advanced Green function is:

$$\Delta_i^l = \frac{2\pi}{2E_i}\delta(k^0 - (-p_i^0 + E_i)). \tag{3.8}$$

The superscript l indicates that this delta function picks out the propagator pole with a positive energy component of the momentum $k + p_i$, which originally was situated in the lower half plane. The k^0 integration over a product of advanced Green functions A_i vanishes, since for two or more Green functions the integrand falls of sufficiently fast for large k^0 and one can close the contour of integration in the lower half plane, where no poles are situated:

$$0 = \int N(k)\prod_i^n A_i. \tag{3.9}$$

Replacing A_i with $F_i - \Delta_i^l$, we get:

$$0 = \int N(k)\left[F\cdots F - \sum \Delta^l F\cdots + \sum \Delta^l\Delta^l F\cdots - \ldots + (-1)^n \sum \Delta^l\cdots\Delta^l\right], \tag{3.10}$$

where we skipped indices in the terms in the brackets.

Equation (3.10) is the Feynman Tree Theorem [13, 52], stating that a loop integral can be expressed as a sum of tree graphs. The first sum runs over all permutations where one propagator is replaced by a delta function, the second sum runs over all terms including two delta functions and so on. The first term on the right hand side, which contains only Feynman Green functions is the integrand (3.1). In the following the terminus *cutting a propagator* of a loop will refer to one of the terms in (3.10), where a propagator was replaced by a delta function.

In the following, we will derive an equation which is better suited for a numerical evaluation.

Improved Version of the Feynman Tree Theorem

The integrand we want to evaluate in a final phase space integration should not contain any auxiliary parameter like the infinitesimal ϵ. We can re-express the Feynman Green functions F_i by the use of the identity:

$$\frac{1}{x-a\pm i\epsilon} = \mathcal{P}\frac{1}{x-a} \mp i\pi\delta(x-a), \tag{3.11}$$

where $\mathcal{P}$ is Cauchy's Principal Value, which is obtained by evenly approaching the singular point from both sides such that the diverging pieces cancel each other. Applying this identity to the Feynman Green function (3.4) and again skipping the $i\epsilon$ term in the factor in front of the brackets we get:

$$\begin{aligned} F_i &= \frac{i}{2E_i}\left(\mathcal{P}\frac{1}{k^0-(-p_i^0+E_i)} - i\pi\delta(k^0-(-p_i^0+E_i)) \right. \\ &\qquad \left. -\mathcal{P}\frac{1}{k^0-(-p_i^0-E_i)} - i\pi\delta(k^0-(-p_i^0-E_i))\right) \\ &\equiv P_i + \frac{1}{2}\Delta_i^l + \frac{1}{2}\Delta_i^u, \end{aligned} \tag{3.12}$$

where we defined Δ^u as the delta function setting the zero component of the momentum of the associated propagator negative:

$$\Delta^u = \frac{2\pi}{2E_i}\delta(k^0-(-p_i^0-E_i)). \tag{3.13}$$

P stands for the propagator with no $i\epsilon$-prescription in the numerator:

$$P_i = \mathcal{P}\frac{i}{(k+p_i)^2-m_i^2}. \tag{3.14}$$

In numerical evaluations of tree amplitudes, propagators of this form, without $i\epsilon$-terms, are used. Inserting (3.12) in (3.10), we therefore get after some combinatorics a version of the tree theorem (3.10), which is better suited for numerical evaluations:

$$\begin{aligned} \int I(k) &= \int N(k)\left[\Delta_1^l P_2\cdots P_n + P_1\Delta_2^l P_3\cdots P_n + \ldots + P_1\cdots P_{n-1}\Delta_n^l\right] \\ &\quad + \int N(k)\sum_{\substack{perm. \\ U+L\geq 2}} C_{LUP}\ \Delta^{l^L}\Delta^{u^U}P^P, \end{aligned} \tag{3.15}$$

$$C_{LUP} = \frac{1}{2^{L+U}}\left(1-(-1)^L\right). \tag{3.16}$$

Since the structure of (3.15) is still very similar to (3.10), we will from now on refer to (3.15) as the Feynman Tree Theorem. The sum runs over all possible permutations, where the functions (Δ^l,Δ^u,P) appear (L,U,P) times, with the additional constraint $L+U+P=n$. The coefficient C_{LUP} stands in front of every term. Note that there are no terms with an even number of Δ^l functions. We explicitly wrote out the terms containing one Δ^l function in the first line. Here, in each term, one of the propagators of the original loop is replaced by a delta function. After k_0 integration, all of the terms of the first line in (3.15) can be interpreted as tree graphs with one additional phase space integral

$$\int \frac{d^3k}{(2\pi)^3 2E_i}. \tag{3.17}$$

Note however, that the momentum which is put on-shell is $k + p_i$ and the integration is performed over k. One must not shift the integration momentum in a single term, since the integrand consists of several terms which are coherently summed up. Some of these terms may have peaks or may even be UV divergent and only in the sum singularities are canceled.

The numerator of a propagator, which in the preceding derivation was included in the function $N(k)$, can be written as the product of two wave functions of the corresponding particle summed over all physical and unphysical helicity states:

$$(\not{k} + \not{p}_i + m) = \sum_\lambda u_\lambda(k + p_i)\bar{u}_\lambda(k + p_i); \tag{3.18}$$

$$(\not{k} + \not{p}_i - m) = \sum_\lambda v_\lambda(k + p_i)\bar{v}_\lambda(k + p_i); \tag{3.19}$$

$$-g_{\mu\nu} = \sum_\sigma \epsilon^*_\mu(k + p_i; \sigma)\epsilon_\nu(k + p_i; \sigma). \tag{3.20}$$

When a propagator is replaced by Δ^l_i, setting $k + p_i$ on the mass shell, the corresponding numerator can be read as the product of one additional incoming and outgoing external on-shell particle. For a cut fermion propagator, we will obtain the particle if the momentum flow of the loop is in the same direction as the fermion number flow and antiparticles otherwise. This interpretation will help us understand the cancellation of IR divergences of loop diagrams by real emissions, cf. section 3.3. Furthermore, the creation of all relevant Feynman graphs contributing to a process in a given order is reduced to the task of finding all tree level graphs with the corresponding additional particles.

The first line of (3.15) can also be interpreted as the result of the k_0 integration of the original loop, when the contour is closed in the lower half plane and only single, simple poles are picked up. Setting $i\epsilon$ to zero afterwards leads to wrong results if poles fall together and form double or multiple poles.

In (3.15), there are additional contributions which are collected in the sum in the second line. These terms give a non-vanishing contribution, if the momenta of the propagators they were replaced with go on-shell simultaneously. Since after the k^0 integration there are still δ-functions left, these terms will get support for hypersurfaces, lines or points in the three-dimensional phase space volume, dependent on the initial number of Δ_i functions. Since each Δ_i effectively lowers the dimension of the integration by one, the contribution of these terms can be calculated rather easily. Whether these terms give a finite contribution, can already be inferred from the integrand of the terms in the first line of (3.15). When replacing the original integral by a sum over tree graphs with one additional on-shell particle, the remaining propagators can become singular, or in other words, internal lines can get on-shell at certain values of $\vec{k}$. This leads to a peak structure which is resembled by the sub-leading terms in (3.15).

Replacing a propagator by a delta function reduces the number of factors i by one. Terms in (3.15) with an even number of Δ_i will therefore give an imaginary contribution to the final result, terms with an odd number a real contribution. Note that terms with an even number of Δ^l vanish, the reason for that will be explained in the next section. Terms with one Δ^l and one Δ^u are exactly those which are needed in the optical theorem to calculate the imaginary part of a scattering amplitude [56].

The preceding results immediately generalize to multi loop diagrams. After cutting one loop, the resulting graphs have one additional particle in the initial and final state and one loop less. The remaining loops can further be cut until only tree graphs are left. A more detailed description in the case of two loops is given in appendix D.

Since loop correction to processes include any intermediate state as long it is allowed by the couplings, the above arguments can be reversed and summarized as:

- For any, say $2 \to n$ process, all corrections can be found by coherently summing all possible tree graphs of the process $2 + l \to n + l$, with l additional on-shell particles in the initial and final state. These particles are of any allowed physical kind, but for each additional incoming particle, the corresponding outgoing particle is identical in all intrinsic and kinematic states. For each additional particle a sum over helicity states and an integral over phase space has to be performed. Additional contributions come from terms which correspond to multiple cuts of the original loops. These can directly be inferred from the singularity structure of the tree graphs.

Singularities of Feynman Diagrams

In the following sections, we will investigate the singularity structure of the tree graphs obtained by the Tree Theorem. In general, the set of all possible non-ultraviolet singularities of a one loop Feynman diagram is given by the following Landau equations [57]:

$$\kappa_i(q_i^2 - m_i^2) = 0, \tag{3.21}$$

$$\sum_i \kappa_i q_i = 0, \tag{3.22}$$

for at least one non-zero κ_i. Here, $q_i = k + p_i$ is the momentum flowing through propagator P_i, k is the integration momentum of the loop and p_i is a linear combination of external momenta. These equations are derived from the condition that the k_0-integration contour is trapped between poles of the integrand and can therefore not be avoided by a deformation of the integration path, see also [4]. Thus, either a propagator P_i goes on-shell or the corresponding κ_i vanishes and the second equation is reduced by the term $\kappa_i q_i$. In general the set of solutions depend on the direction of external momenta. In the next section, we will examine these internal or threshold singularities which do not give rise to divergences but to branch points and can be fixed by suitable subtraction terms. Solutions, which are independent of the direction of external momenta are called mass singularities. These fall into two categories, the infrared and the collinear divergences, which will be discussed in section 3.3.

3.2. Internal Singularities

When the momentum integration is performed in the first line of (3.15), the integrand might get peaks in parts of the phase space where momenta of remaining propagators are on-shell. These regions are open or closed two-dimensional surfaces in the three-dimensional integrand. Intersections of these surfaces will correspond to kinematic situations where two or more momenta of internal lines become on-shell at the same time. The occurrence of such peaks, although analytically integrable, leads to problems in the numerical evaluation of the integrand, cf. chapter 4. Subtraction terms with zero real value but with the same peak structure will smooth the integrand and allow for a better numerical evaluation. In this section we will give the conditions under which peaks of the integrand arise and calculate the corresponding fix functions.

The cutting of propagator P_i in a loop leads to a delta function in (3.8), which effectively sets the four-vector $k+p_i$ on its mass-shell at $(k+p_i)^2 = m_i^2$ with positive zero component:

$$\delta\left(k^0 - (-p_i^0 + \sqrt{(\vec{k}+\vec{p}_i)^2 + m_i^2})\right). \tag{3.23}$$

There are two possible situations under which another propagator P_j can get singular corresponding to its original k_0-poles in the lower and upper half plane, which correspond to the positive and negative zero components $\pm E_j$. After the k_0 integration the relevant term of the integrand in (3.15) reads:

$$\Delta_i^l P_j R(k) = \frac{1}{2E_i} \frac{i}{[(p_j^0 - p_i^0) + (E_i - E_j)][(p_j^0 - p_i^0) + (E_i + E_j)]} R(-p_i^0 + E_i, \vec{k}), \tag{3.24}$$

where $R(k)$ is the analytic remainder of the term, containing the numerator and denominators of further propagators which are assumed to be non-singular in the integration volume. If the first factor in the denominator vanishes for some $\vec{k}$, both momenta of the two propagators P_i and P_j get on-shell with a positive zero component. In other words, at this constellation of the integration momentum $\vec{k}$, the two poles in the lower k_0 half plane of the original loop momentum coincide. Therefore, we will also encounter this singularity when propagator P_j is cut:

$$\Delta_j^l P_i R(k) = \frac{1}{2E_j} \frac{i}{[(p_i^0 - p_j^0) + (E_j - E_i)][(p_i^0 - p_j^0) + (E_j + E_i)]} R(-p_j^0 + E_j, \vec{k}). \tag{3.25}$$

In the limit of the first factor becoming zero, the residue of the combined contribution vanishes:

$$\begin{aligned} \lim_{(p_j^0 - p_i^0) + (E_i - E_j) \to 0} & \left((p_j^0 - p_i^0) + (E_i - E_j)\right) \left(\Delta_i^l P_j R(k) + \Delta_j^l P_i R(k)\right) \\ &= \frac{i}{2E_i 2E_j} \left(R(-p_i^0 + E_i, \vec{k}) - R(-p_i^0 + E_i, \vec{k})\right) = 0. \end{aligned} \tag{3.26}$$

Thus, if the two terms are added, the peaks will compensate each other and the integrand can safely be evaluated numerically in this case. Note that we also did not get a term in (3.15) with only two Δ^l. Therefore, just like there is no peak in the sum of the tree level contribution there is also no imaginary contribution to the final result in this case.

In the case where the second factor in (3.24) becomes singular, we will get a peak and corresponding imaginary part. This happens, if one pole of the lower k_0-half plane coincides with a pole in the upper half plane. There is no term with a single Δ^u in (3.15), which would set the associated momentum on-shell with a negative zero component and could lead to a cancellation of this peak.

3.2.1. Conditions for Internal Singularities

We now look for general conditions under which a loop propagator P_j becomes singular if we cut a propagator P_i, and give equations for the corresponding surfaces. Cutting propagator P_i, we have:

$$\begin{aligned} 0 &\stackrel{!}{=} (k+p_j)^2 - m_j^2\big|_{k^0=-p_i^0+\sqrt{(\vec{k}+\vec{p}_i)^2+m_i^2}}, \\ &\stackrel{!}{=} ((k+p_i)+(p_j-p_i))^2 - m_j^2\big|_{k^0=-p_i^0+\sqrt{(\vec{k}+\vec{p}_i)^2+m_i^2}}, \\ &\stackrel{!}{=} m_i^2 - m_j^2 + 2(k+p_i)(p_j-p_i) + (p_j-p_i)^2\big|_{k^0=-p_i^0+\sqrt{(\vec{k}+\vec{p}_i)^2+m_i^2}}. \end{aligned} \tag{3.27}$$

The occurrence and the shape of the peaks depend on the value of $p_{ji}^2 \equiv (p_j - p_i)^2$. We can distinguish 4 kinematic regions, separated by $p_{ji}^2 = 0$ and the two nodes $\lambda(p_{ji}^2, m_i^2, m_j^2) = 0$ of the kinetic function defined by

$$\lambda(x,y,z) = x^2 + y^2 + z^2 - 2xy - 2xz - 2yz. \tag{3.28}$$

The different regimes are depicted in figure 3.1.

We switch to Lorentz frames where the calculation of solutions to (3.27) is particularly simple. We first discuss the case of negative p_{ji}^2.

• I: $p_{ji}^2 < 0$

Here, we cannot find a rest frame of $p_j - p_i$, however, we can define a Lorentz transformation projecting $p_j - p_i$ on the z-axis:

$$\Lambda_{\mu\nu}(p_j - p_i)^\nu = (0,0,0,p_{ji}^z), \tag{3.29}$$

$$-{p_{ji}^z}^2 = (p_j - p_i)^2, \tag{3.30}$$

$$k'_\mu \equiv \Lambda_{\mu\nu} k^\nu. \tag{3.31}$$

Using this transformation we get for (3.27):

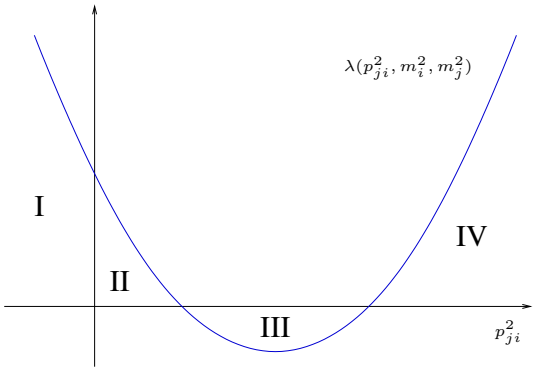

Figure 3.1: Different regions for p_{ji}^2, defined by the origin and the two zeros of the kinetic function λ. The occurrence and the structure of singularities of the integrand depend on the value of p_{ji}^2.

$$\begin{aligned} 0 &\overset{!}{=} m_i^2 - m_j^2 + 2(k+p_i)(p_j-p_i) + (p_j-p_i)^2, \\ &= m_i^2 - m_j^2 + 2k(p_j-p_j) + p_j^2 - p_i^2, \\ &\overset{L.T.}{=} m_i^2 - m_j^2 - 2k'_z p_{ji}^z + p_j^2 - p_i^2, \\ \Longrightarrow k'_z &= \frac{(p_j^2 - m_j^2) - (p_i^2 - m_i^2)}{2p_{ji}^z}. \end{aligned} \tag{3.32}$$

There are no further conditions for this singularity to appear. Thus, we will always encounter it in the case of $(p_j - p_i)^2 < 0$. However, if we cut propagator P_j, propagator P_i will exactly have the same singularity with opposite sign. This can be seen from the derivation of (3.32) by interchanging indices i and j, but applying the same Lorentz transformation as before. As a result we have the situation described in the beginning of this section and the two peaks will cancel each other in the sum of the tree graphs.

• $p_{ji}^2 > 0$, (II,III,IV)

Here, we apply a Lorentz transformation to get into the rest frame of $p_j - p_i$:

$$(p_j - p_i)^\mu \to p_{ji}^\mu = \Lambda^{\mu\nu}(p_j - p_i)_\nu = (p_{ji}^0, \vec{0}), \tag{3.33}$$

$$p_{ji}^{0\,2} = (p_j - p_i)^2. \tag{3.34}$$

We indicate k' as the Lorentz transformed on-shell momentum[3]:

$$k^{\mu\prime} = (\sqrt{\mathbf{k}'^2 + m_i^2}, \vec{k'}) = \Lambda^{\mu\nu}(k + p_i)_\nu. \tag{3.35}$$

[3]Bold letters indicate absolute values of spatial vectors

With this parameterization of $k^{\mu\prime}$ the Lorentz transformation has to be of proper orthochronous type, which implies that p^0_{ji} may be both positive or negative. We thus get from (3.27):

$$m_i^2 - m_j^2 + 2p^0_{ji}\sqrt{\mathbf{k'}_s^2 + m_i^2} + {p^0_{ji}}^2 = 0, \tag{3.36}$$

$$\sqrt{\mathbf{k'}_s^2 + m_i^2} = \frac{m_j^2 - m_i^2 - {p^0_{ji}}^2}{2p^0_{ji}}, \tag{3.37}$$

$$\Longrightarrow \mathbf{k'}_s^2 = \frac{1}{4{p^0_{ji}}^2}(m_i^4 + m_j^4 + {p^0_{ji}}^4 - 2m_i^2{p^0_{ji}}^2 - 2m_j^2{p^0_{ji}}^2 - 2m_i^2m_j^2). \tag{3.38}$$

Therefore, the integrand gets singular at

$$\mathbf{k}_s = \frac{\lambda^{\frac{1}{2}}({p^0_{ji}}^2, m_i^2, m_j^2)}{2|p^0_{ji}|}, \tag{3.39}$$

the surface of a sphere with radius $\mathbf{k}_s$. The kinetic function λ is defined in (3.28). To get to equation (3.39), two conditions have to be met to satisfy equations (3.37) and (3.38):

$$\frac{m_j^2 - m_i^2 - {p^0_{ji}}^2}{2p^0_{ji}} > 0, \tag{3.40}$$

$$\lambda({p^0_{ji}}^2, m_i^2, m_j^2) > 0. \tag{3.41}$$

The function $\lambda({p^0_{ji}}^2, m_i^2, m_j^2)$ is positive for ${p^0_{ji}}^2 < (m_i - m_j)^2$ and ${p^0_{ji}}^2 > (m_i + m_j)^2$. Condition (3.41) therefore defines the three kinematic ranges for $p^2_{ji} > 0$, depicted in figure 3.1. If the kinetic function λ is positive we have to check if condition (3.40) is fulfilled. We also check the similar condition of propagator P_i getting singular if propagator P_j is cut. This condition reads

$$\frac{m_i^2 - m_j^2 - {p^0_{ji}}^2}{2p^0_{ji}} < 0. \tag{3.42}$$

- II: $0 < p^2_{ji} < (m_i - m_j)^2$

  Suppose $m_j < m_i$. Then condition (3.40) simplifies to $p^0_{ji} < 0$. The numerator of (3.42) is:

$$m_i^2 - m_j^2 - {p^0_{ji}}^2 > m_i^2 - m_j^2 - (m_i^2 - 2m_im_j + m_j^2) = -2m_j(m_j - m_i) > 0. \tag{3.43}$$

  Thus, condition (3.42) is now $p^0_{ji} < 0$, the same as (3.40). Therefore, if these conditions are fulfilled, we will get a singularity in both terms, when propagator P_i is cut and propagator P_j gets singular and vice versa. Again, this is the situation

described in the introduction to this section, when both zero components of the on-shell momenta are positive. This can be seen in the following. If propagator P_i is cut, the denominator of propagator P_j can be written as:

$$\left(\sqrt{\mathbf{k}^2+m_i^2}+p_{ji}^0-\sqrt{\mathbf{k}^2+m_j^2}\right)\left(\sqrt{\mathbf{k}^2+m_i^2}+p_{ji}^0+\sqrt{\mathbf{k}^2+m_j^2}\right). \tag{3.44}$$

The first factor is the one coming originally from the pole in the lower k_0 half plane. Its vanishing indicates the coincidence of the original poles of the two propagators. We have

$$\sqrt{\mathbf{k}^2+m_i^2}+p_{ji}^0=\frac{m_j^2-m_i^2+{p_{ji}^0}^2}{2p_{ji}^0}>\frac{m_j^2-2m_im_j+m_j^2}{2p_{ji}^0}=\frac{2m_j(m_j-m_i)}{2p_{ji}^0}>0. \tag{3.45}$$

Therefore, the second factor is strictly positive and the singularity can only arise from the first factor. Thus, the two poles of the lower half plane fall together and the corresponding peaks cancel each other as shown above. The analysis for $m_j > m_i$ is analogous and leads to the same result.

- III: $(m_i-m_j)^2<p_{ji}^2<(m_i+m_j)^2$

  In this region condition 3.41 is not fulfilled. Therefore the integrand does not get a singular contribution form propagator j.

- IV: $(m_i+m_j)^2<p_{ji}^2$

  In this case the numerator of condition (3.40) as well of condition (3.42) is strictly negative. Thus, exactly one of the two condition is fulfilled. Note also that if condition (3.40) is fulfilled, meaning $p_{ji}^0<0$, the second factor of (3.44) vanishes. Thus, while one propagator gets on-shell with a positive zero component, the other has a negative zero component. Here, the singularity is not compensated by another term in the integrand, and we will add a fix function to cancel this singularity, as will be shown in section 3.2.2. In this kinematic range, the final result also gets a contribution from the double delta terms in equation (3.15). This adds to the imaginary part of the integral. Here, we have exactly the situation of the optical theorem, where to calculate the imaginary part of a forward scattering amplitude two propagators are set on-shell at the same time.

- $\lambda = 0$

There are two more cases which we have not discussed yet: $p_{ji}^2=(m_i-m_j)^2$ and $p_{ji}^2=(m_i+m_j)^2$. In case the two points fall together, we either have $m_i = 0$ or $m_j = 0$ or both at the same time. These are so-called mass singularities, where the integrand is not just singular but divergent. These divergences are compensated by the addition of real emission graphs. We will discuss this in section 3.3.

If the kinetic function λ gets zero at two different values of p_{ji}^2, which happens if both masses are non-zero, the argumentation of the case $p_{ji}^2 < (m_i - m_j)^2$ does not change in the limit $p_{ji}^2 = (m_i - m_j)^2$ and we do not encounter any peaks in the integrand. However, if $p_{ji}^2 = (m_i + m_j)^2$, we are at the threshold where the two real particles with masses m_i and m_j can be produced at the same time. These are so-called Coulomb singularities, where higher order corrections in perturbation theory can become equally important. To get meaningful results, resummation methods can be applied, e.g. cf. [58]. In general, these peaks are pointlike and integrable, setting the origin of the integration variables to this point and using spherical coordinates will smooth these peaks.

3.2.2. Fix Functions

We are now going to calculate the fix functions which will compensate the singularities of the integrand without adding a real part to the result[4]. In chapter 4, we will give an overview of several integration methods. It will then become clear, that although the singularities are analytically integrable, numerical integration algorithms will in general not be able to adapt to the singular peaks and give stable results.

Suppose we have replaced propagator P_i with Δ_i^l and propagator P_j gets singular at a hypersurface in the integration volume, thus conditions (3.40) and (3.41) are fulfilled. The integrand is then

$$\int \frac{d^3k}{2\sqrt{(\vec{k}+\vec{p_i})^2 + m_i^2}} \frac{R(k)}{(k + p_i + p_j - p_i)^2 - m_j^2}, \tag{3.46}$$

where $R(k)$ is the analytic rest of the integrand. We now change the integration momentum to the momentum $k'_\mu = \Lambda_{\mu\nu}(k + p_i)^\nu$ in the rest frame of $p_j - p_i$ and switch to spherical coordinates with radial coordinate $\mathbf{k}'$

$$\int \frac{\mathbf{k}'^2 d\mathbf{k}' d\Omega}{2\sqrt{\mathbf{k}'^2 + m_i^2}} \frac{R(\Lambda^{-1}k' - p_i)}{m_i^2 - m_j^2 + 2p_{ji}^0\sqrt{\mathbf{k}'^2 + m_i^2} + {p_{ji}^0}^2}. \tag{3.47}$$

Here we used the Lorentz invariance of the integration measure $d^3k/2E_i$. In this system the peak lies on a surface of a sphere with radius $\mathbf{k}_s$ given by (3.39). Expanding the denominator around $\mathbf{k}_s$ yields

$$\int \frac{\mathbf{k}'^2 d\mathbf{k}' d\Omega}{2\sqrt{\mathbf{k}'^2 + m_i^2}} \frac{R(\Lambda^{-1}k' - p_i)}{\frac{2p_{ji}^0 \mathbf{k}_s}{\sqrt{\mathbf{k}'^2_s + m_i^2}}(\mathbf{k}' - \mathbf{k}_s) + \mathcal{O}\left((\mathbf{k}' - \mathbf{k}_s)^2\right)}. \tag{3.48}$$

Taking the limit $\mathbf{k}' \to \mathbf{k}_s$ the residue of the integrand is

[4] The idea of adding a zero to the integrand which smooths the peaks is taken from [54]. In this section we will give an elaborate construction of single fix functions and also derive fix functions in case of overlapping peaks.

$$\mathrm{Res}(k'_s) = \frac{\mathbf{k_s}}{4p^0_{ji}} R(\Lambda^{-1}k'_s - p_i). \tag{3.49}$$

Here, k'_s is a four-vector with the spatial part fixed onto the surface with radius $\mathbf{k}_s$:

$$k'_s = (\sqrt{\mathbf{k}_s^2 + m_i^2}, \mathbf{k}_s \frac{\vec{k'}}{|\vec{k'}|}). \tag{3.50}$$

If we subtract

$$\frac{\mathrm{Res}(k'_s)}{\mathbf{k}' - \mathbf{k}_s} \tag{3.51}$$

from the integrand, this additional term does not add to the principal value of the integral if it is integrated over a region with symmetrical borders around the singular point $\mathbf{k}_s$. The peak of the original integrand vanishes.

Thus, we can define a fix function, which in the rest frame of $p_j - p_i$ reads

$$\mathrm{Fix}(\mathbf{k}', k'_s) \equiv \frac{\mathbf{k}_s R(\Lambda^{-1}k'_s - p_i)}{4p^0_{ji}} \left(\frac{1}{\mathbf{k}' - \mathbf{k}_s} - \frac{\mathbf{k}' - \mathbf{k}_s}{c^2} \right) \theta(\mathbf{k}' - (\mathbf{k}_s - c))\theta((\mathbf{k}_s + c) - \mathbf{k}'), \tag{3.52}$$

with $\theta(x)$ being the step function. Here, we also subtracted a term proportional to the odd function $(\mathbf{k}' - \mathbf{k}_s)$ to make the joined integrand continuous at the artificial borders introduced by the theta functions. Since the integration over the radial coordinate $\mathbf{k}'$ runs from zero to infinity, the width c of this subtraction term can maximally be taken to be the radius $\mathbf{k}_s$. In the numerical evaluation stable results were obtained, when we took the width of the subtraction term equal to the infrared cutoff, $c = \Delta E_s$. We can also add a term proportional to $(\mathbf{k}' - \mathbf{k}_s)^3$, to also make the derivative continuous at the borders. In this case, the terms in the brackets in (3.52) are:

$$\left(\frac{1}{\mathbf{k}' - \mathbf{k}_s} - 2\frac{\mathbf{k}' - \mathbf{k}_s}{c^2} + \frac{(\mathbf{k}' - \mathbf{k}_s)^3}{c^4} \right). \tag{3.53}$$

Transforming back to the original momentum of integration, we get

$$\int d\mathbf{k}' d\Omega \mathrm{Fix}(\mathbf{k}', k'_s) = \int \frac{d^3k'}{\mathbf{k}'^2} \mathrm{Fix}(\mathbf{k}', k'_s) = \int \frac{\|\Lambda\| d^3k}{\overrightarrow{\Lambda(k+p)}^2} \mathrm{Fix}(|\overrightarrow{\Lambda(k+p)}|, k'_s(\overrightarrow{\Lambda(k+p)})), \tag{3.54}$$

where $\overrightarrow{\Lambda(k+p)}$ is the spatial part of the transformed four-vector and $\|\Lambda\|$ the corresponding Jacobian. Explicit formulae for these can be found in appendix A.3. In (3.54), we also indicated the dependence of the fixed four-vector k'_s on the spatial integration momentum $\mathbf{k}'$ in the second argument of the fix function.

When added to the integrand, the subtraction term (3.54) smooths the peak which arises when a pole in the lower k^0 half plane and a pole in the upper half plane fall together in

the original loop integrand. Note that the double delta term in (3.15) including Δ_i^l and Δ_j^u is supported at $\mathbf{k}' = \mathbf{k}_s$ and adds an imaginary part to the result.

Overlapping Peaks

If propagator P_i is cut, there might also exist a further propagator P_k fulfilling the conditions (3.40) and (3.41) in addition to propagator P_j[5]. If this is the case, another fix function has to be added to the same integrand smoothing the second peak. In a general inertial frame the peaks have the form of rotational ellipsoids. In principle, these two peaks may overlap, leading to a line in the integration volume where both propagators P_j and P_k can get singular at the same time. This is equivalent to a non-vanishing contribution of a term with one Δ_i^l, Δ_j^u and Δ_k^u in (3.15). In this case we have to add a further fix function.

The conditions for the occurrence of the two peaks, (3.40) and (3.41), as well as the condition for an intersection of these peaks can be checked numerically. When cutting propagator P_i in the rest frame of $p_j - p_i$, the radius of the sphere where propagator P_j gets singular is given by (3.39). With this we can construct the on shell four-vector (3.50). We now transform into the rest frame of $p_k - p_i$:

$$k_s^{\mu\prime} = \Lambda^{\mu\nu} k_{s\nu} \ , \qquad k_s^\mu = (\sqrt{\mathbf{k}_s^2 + m_i^2}, \mathbf{k}_s \frac{\vec{k}}{|\vec{k}|}). \tag{3.55}$$

Similar to (3.36), propagator P_k gets singular if

$$m_i^2 - m_k^2 + 2\sqrt{p_{ki}^2}\frac{p_{ki}^0}{|p_{ki}^0|}\sqrt{\mathbf{k}'^2_s + m_i^2} + p_{ki}^2 \stackrel{!}{=} 0, \tag{3.56}$$

where $\mathbf{k}'_s$ is the absolute value of the spatial part of the four-vector $k_s^{\mu\prime}$ in (3.55) and p_{ki}^0 is the non-transformed zero component of $p_{ki} = p_k - p_i$. Using equation (A.24) of appendix A, we get

$$m_i^2 - m_k^2 + 2\sqrt{p_{ki}^2}\frac{p_{ki}^0}{|p_{ki}^0|}\gamma(k_s^0 - \vec{\beta}\vec{k}_s) + p_{ki}^2 \stackrel{!}{=} 0. \tag{3.57}$$

Using $\gamma = \frac{|p_{ki}^0|}{\sqrt{p_{ki}^2}}$ and equation (3.37) to replace k_s^0 we obtain:

$$\vec{\beta}\vec{k}_s \stackrel{!}{=} \frac{m_i^2 - m_k^2 + p_{ki}^2}{2p_{ki}^0} + \frac{m_j^2 - m_i^2 - p_{ji}^2}{2p_{ji}^0}. \tag{3.58}$$

This condition is fulfilled if the righthand side is between the bounds $+|\beta k_s|$ and $-|\beta k_s|$. If this is the case, we have to add a third fix function in the region where the two singularities overlap. This will be shown in the following.

[5]The kinetic function $\lambda(p^2, m_1^2, m_2^2)$ of two adjacent loop propagators can only be positive if p^2 is off-shell or the invariant mass of an unstable particle. It follows that the above possibility of two propagators going on shell at the same time is given in $2 \to n$ processes with $n \geq 4$ or $2 \to 2$ processes with at least two off-shell or instable external particles.

For better readability, we are now changing to a more symbolic notation. Suppose the integrand has the form:

$$\frac{f(r,\theta,\phi)}{(r-a)(r'(r,\theta,\phi)-b)}, \tag{3.59}$$

where r, θ, ϕ are spherical coordinates in the integration system and r' a function of these coordinates which is the radial coordinate in another coordinate frame. The function $f(r,\theta,\phi)$ represents the non-singular rest of the integrand. The two fix functions which smooth the first and second peak separately are given by:

$$\mathrm{Fix}_1 = \frac{f(a,\theta,\phi)}{\overline{(r-a)}(r'(a,\theta,\phi)-b)}, \quad \mathrm{Fix}_2 = \left.\frac{f(r,\theta,\phi)}{(r-a)}\right|_{r'=b} \frac{1}{\overline{(r'(r,\theta,\phi)-b)}}. \tag{3.60}$$

Here, the first factor of the second fix function is fixed at $r' = b$, which translates to a relation of the coordinates r, θ, ϕ. The line over the factors in the denominator indicates that the fix function is to be subtracted from the original integrand in a region symmetric around the corresponding singularity. Since in the overlapping region, defined by the width parameter c in the theta functions included in (3.60), two fix functions are subtracted from the integrand, one could add another function which fixes the numerator to points on the intersection line and projects each singular factor onto the singular surfaces of the other factor:

$$\mathrm{Fix}_3 = \left.\frac{f(a,\theta,\phi)}{\overline{(r-a)}}\right|_{r'=b} \frac{1}{\overline{(r'(a,\theta,\phi)-b)}}. \tag{3.61}$$

However, this third fix function does not cancel the remaining peaks but gives even rise to new singularities. These occur at points where the opening angle of the two normals to the singular surfaces is small. Here, the two factors in the denominator will become very small if projected onto the surfaces. Being of second order in that small distances, this peaks will not be canceled by the fix functions (3.60), where only one of the two factors will be small at this point. Therefore, this naive approach cannot be used.

We therefore have to find an alternative way to fix the peaks. If only the second singularity in (3.59) was present, the expression for the fixed integrand would read:

$$\frac{f(r,\theta,\phi) - f(r,\theta,\phi)|_{r'=b}}{(r'(r,\theta,\phi)-b)}. \tag{3.62}$$

In the limit $r' \to b$, this is equivalent to the derivative of f with respect to r' at $r' = b$ and we can interpret (3.62) as a result of an operation on f similar to differentiation without taking the limit $r' \to b$. If we assume f to be differentiable, no singularities are introduced. Using the construction of the fix function introduced in the beginning of this section, expression (3.62) is continuous and differentiable. We can therefore again operate on (3.62) to get the difference equation with respect to r:

$$\frac{f(r,\theta,\phi)}{(r-a)(r'(r,\theta,\phi)-b)} - \frac{f(r,\theta,\phi)|_{r'=b}}{(r-a)(\overline{r'(r,\theta,\phi)-b})}$$
$$-\frac{f(a,\theta,\phi)}{\overline{(r-a)}(r'(a,\theta,\phi)-b)} + \frac{f(a,\theta,\phi)|_{r'=b}}{\overline{(r-a)}(\overline{r'(a,\theta,\phi)-b})}. \tag{3.63}$$

This expression is again continuous and does not have any peaks. The last three terms can therefore be interpreted as fix function to the original integrand. However, the second and forth term are not zero anymore. The factor $(r-a)$ is not fixed to a constant r' and gives asymmetric contributions if the fix function is subtracted in a region symmetric around $r'=b$. To get proper results, the region where these fix functions are used should therefore be small.

In appendix C, we present the calculation of a simple three point function which develops overlapping peaks due to unphysical kinematic parameters. Here, we use (3.63) to construct the fix functions. We examine the dependence of the results on the width of the fix functions and the efficiency of the numerical integration. A satisfactory trade-off between accuracy and efficiency can be found. Here, also terms in (3.15) with three Δ contribute to the final result. We also give their explicit calculation.

The above analysis extends to any number of propagators which get singular simultaneously. We can always start with a non-singular function f and apply the difference equation (3.62), transform into another frame and again using (3.62) with respect to another variable and so on. However, an accurate estimation of the inflicted error by adding these fix function is still missing.

Higher Order Fix Functions

The subtraction terms (2.40) added by the renormalization scheme to cancel the UV divergent terms sometimes contain squared propagators. Here, when one performs the k^0 integration, one has to take the derivative of the analytic rest of the integrand with respect to k^0 before replacing it according to the delta function obtained from the cut propagator. It can happen that another propagator gets singular and the resulting peak would be of second order. In this case one can construct a further fix function. The relevant term of the integrand in the rest frame, similar to (3.47), is

$$I_2 = \frac{\mathbf{k'}^2}{2\sqrt{\mathbf{k'}^2+m_i^2}} \frac{R(\Lambda^{-1}k'-p_i)}{\left(m_i^2-m_j^2+2p_{ji}^0\sqrt{\mathbf{k'}^2+m_i^2}+{p_{ji}^0}^2\right)^2}. \tag{3.64}$$

Expanding numerator and denominator separately around $\mathbf{k'}-\mathbf{k}_s$ we get

$$I_2 = \frac{(\mathbf{k}_s^2+m_i^2)^{\frac{3}{2}}}{8{p_{ji}^0}^2(\mathbf{k'}-\mathbf{k}_s)^2} \frac{\mathbf{k}_s R(\mathbf{k}_s)+(2R(\mathbf{k}_s)+\mathbf{k}_s R'(\mathbf{k}_s))(\mathbf{k'}-\mathbf{k}_s)+\mathcal{O}((\mathbf{k'}-\mathbf{k}_s)^2)}{\mathbf{k}_s(\mathbf{k}_s+m_i^2)+(\mathbf{k}_s^2+2m_i^2)(\mathbf{k'}-\mathbf{k}_s)+\mathcal{O}((\mathbf{k'}-\mathbf{k}_s)^2)}, \tag{3.65}$$

where we wrote $R(\mathbf{k}_s)$ for $R(\Lambda^{-1}k'_s - p_i)$. Multiplying by $(\mathbf{k}' - \mathbf{k}_s)^2$ we get the coefficients of the poles in the Laurent series by taking the limit $\mathbf{k}' \to \mathbf{k}_s$ or taking the derivative with respect to $\mathbf{k}'$ and then taking the limit:

$$I_2 = \frac{r_{-2}}{(\mathbf{k}' - \mathbf{k}_s)^2} + \frac{r_{-1}}{(\mathbf{k}' - \mathbf{k}_s)} + \dots, \tag{3.66}$$

$$r_{-2} = \frac{\sqrt{\mathbf{k}_s^2 + m_i^2} R(\mathbf{k}_s)}{8 {p_{ji}^0}^2}, \tag{3.67}$$

$$r_{-1} = \frac{\mathbf{k}_s R(\mathbf{k}_s) + (\mathbf{k}_s^2 + m_i^2) R'(\mathbf{k}_s)}{8 {p_{ji}^0}^2 \sqrt{\mathbf{k}_s^2 + m_i^2}}. \tag{3.68}$$

For the first order peak we can construct a fix function equivalent to (3.52) with the new residue r_{-1}. For the second order pole we define the fix function as:

$$\mathrm{Fix}_2(\mathbf{k}', k'_s) \equiv r_{-2} \left(\frac{1}{(\mathbf{k}' - \mathbf{k}_s)^2} + \frac{2}{c^2} - \frac{3(\mathbf{k}' - \mathbf{k}_s)^2}{c^4} \right) \Theta(\mathbf{k}' - (\mathbf{k}_s - c)) \Theta((\mathbf{k}_s + c) - \mathbf{k}'). \tag{3.69}$$

Here, the expression in the brackets results from taking the derivative of the corresponding expression of an already fixed first order function with respect to $\mathbf{k}$. Since we defined the first order fix function in (3.53) such that after addition to the singular function the resulting expression is differentiable, also the derivative does not develop a singularity. Transforming the two fix functions back to the initial momentum frame and subtracting them from the integrand removes the peaks. Note that applying the difference equation (3.62) twice at the same point in the same coordinate frame would have lead to the same result.

When all peaks discussed above are removed from the integrand with the help of the fix functions introduced in the last section, there are still peaks left corresponding to virtual infrared and collinear singularities. We will discuss these in the next section.

3.3. Mass Singularities

Up to now we examined singularities of Feynman diagrams which were dependent on directions of external momenta and lead to the threshold singularities discussed above. A further set of solutions to the Landau equations (3.21) and (3.22) are the so called mass singularities which occur independently of the external momenta, cf. [33]. These can lead to divergences of the diagrams.

As discussed in [4], for non-vanishing κ_i in (3.21) and (3.22) only up to two neighboring propagators can go on-shell simultaneously, independent of directions of external momenta. Starting with one non-zero κ_i, equation (3.22) implies $q_i = 0$ and thus $m_i = 0$. This singularity can then be enhanced by singularities of other propagators P_j with $\kappa_j = 0$.

Not allowing for scalar products of different external momenta, this can only occur for the two adjacent propagators P_{i-1} and P_{i+1} leading to the divergent infrared singularity:

$$m_i = 0, \quad p_{i+1}^2 = m_{i+1}^2, \quad p_{i-1}^2 = m_{i-1}^2. \tag{3.70}$$

Thus, we encounter an infrared divergence when a massless particle is exchanged between two external on-shell particles. This singularity can be suppressed by a zero in the numerator at the same point in the integration region, which is the case for the exchange of massless fermions. We will investigate the IR divergences in the next subsection.

If we allow for two non-vanishing κ_i in the Landau equations, we have the conditions:

$$(q_i^2 - m_i^2) \stackrel{!}{=} 0, \quad (q_{i+1}^2 - m_{i+1}^2) \stackrel{!}{=} 0, \quad (\kappa_i q_i + \kappa_{i+1} q_{i+1}) \stackrel{!}{=} 0. \tag{3.71}$$

It follows that the two momenta q_i and q_{i+1} are proportional to each other. This is a collinear singularity and, after analytic evaluation of the integrals, leads to terms with a logarithm of the masses m_i or m_{i+1}. If these masses are small compared to other kinematic parameters of the process, these singularities are enhanced. The line attached to the vertex between the two singular propagators has momentum squared:

$$(q_{i+1} - q_i)^2 = (m_{i+1} - m_i)^2. \tag{3.72}$$

Thus, it can be an external on-shell particle with one of the two masses and the second mass being zero, which for example is the case in QED when a photon line in a loop is collinear to the momentum of the external particle it is attached to. Analytically, these singular terms drop out when the real emission of collinear photons are added to the process. In section 3.3.3, we will give a detailed study of the collinear peaks.

The particle connected to the two singular propagators can also be off-shell. In this case the momentum (3.72) marks the onset of a branch cut from where on the two particles described by the propagators P_i and P_{i+1} could go on-shell. This leads to an imaginary or absorptive part of the amplitude. As mentioned before in section 3.2.1, the onset point of this cut is a Coulomb singularity, where higher order contributions should also be included by resummation. The peaks arising from points somewhere on the branch cut can be eliminated by the fix function introduced in the last section.

In the following we will examine the cancellation of infrared divergences between loop and real emission diagrams and give a definite construction of the counterterms from the BPHZ mechanism.

3.3.1. Infrared Divergences

The infrared divergent part of a loop arises from massless propagators connecting two external on-shell particles, as was described above. As an example, consider the photon exchange of two charged incoming fermions depicted in figure 3.2. Before cutting any propagator the relevant part of the integrand reads:

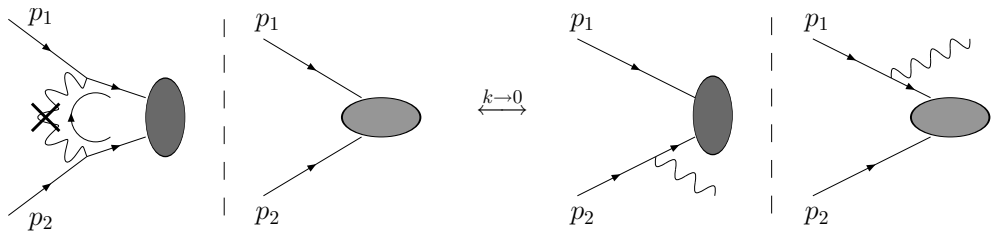

Figure 3.2: Infrared divergent contribution of a loop-born interference term: In the limit $|\vec{k}| \to 0$, the loop integral with the cut photon line diverges. This divergence is compensated by the product of the two corresponding real emission diagrams.

$$\frac{d^4k}{(2\pi)^4} \frac{\dots(\not{k}+\not{p}_1+m_1)\gamma^\mu u_\lambda(p_1)}{k^2+2kp_1} \cdot \frac{-ig_{\mu\nu}}{k^2} \cdot \frac{\dots(-\not{k}+\not{p}_2+m_2)\gamma^\nu u_\kappa(p_2)}{k^2-2kp_2}, \tag{3.73}$$

where for better readability we shifted the integration momentum such that it is equivalent to the momentum flowing through the photon line. Cutting this line, we get

$$\frac{d^3k}{(2\pi)^3 2|\vec{k}|}\sum_\sigma \frac{\dots(\not{k}+\not{p}_1+m_1)\gamma^\mu u_\lambda(p_1)}{2kp_1} \cdot \epsilon_\mu(k,\sigma)\epsilon^*_\nu(k;\sigma) \cdot \frac{\dots(-\not{k}+\not{p}_2+m_2)\gamma^\nu u_\kappa(p_2)}{-2kp_2}\Bigg|_{k_0=|\vec{k}|} \tag{3.74}$$

which is logarithmically divergent in the limit $|\vec{k}| \to 0$. This loop amplitude is multiplied with a Born amplitude $\mathcal{M}_{\text{Born}}{}^\dagger$. Neglecting the term $\not{k}$ in the numerator we can shift the incoming photon line on the upper leg to the Born matrix element, whose relevant part is just the Dirac wave function $\bar{u}_\lambda$ of this particle connected to a γ matrix:

$$\frac{\dots(\not{p}_1+m_1)\gamma^\mu u_\lambda(p_1)\bar{u}_\lambda(p_1)\gamma^\rho\dots}{2kp_1}\cdot\epsilon_\mu(k,\sigma) \to \frac{\dots u_\lambda(p_1)\bar{u}_\lambda(p_1)\gamma^\mu(\not{p}_1+m_1)\gamma^\rho\dots}{2kp_1}\cdot\epsilon_\mu(k,\sigma). \tag{3.75}$$

Here, we used the contraction identity $(\not{p}+m)\gamma^\mu u(p) = 2p^\mu u(p)$. Taking the hermitian conjugate of the right part and adding another $\not{k}$ term in the numerator, we get

$$\dots\frac{\bar{u}_\lambda(p_1)\gamma^\mu(\not{p}_1+m_1)\gamma^\rho\dots}{2kp_1}\cdot\epsilon_\mu(k,\sigma) \to \frac{\dots\gamma^\rho(-\not{k}+\not{p}_1+m_1)\gamma^\mu u_\lambda(p_1)}{2kp_1}\epsilon^*_\mu(k,\sigma). \tag{3.76}$$

This corresponds to the Born diagram with an additional outgoing on-shell photon attached to one external line times an overall factor -1. This comes from the propagator after the emission of the photon. In the real emission graph, the denominator is given by

$$(k-p_1)^2 - m^2 = -2kp_1. \tag{3.77}$$

After the above transformations, the original loop becomes also a born graph with photon emitted from particle 2. Thus, in the limit $|\vec{k}| \to 0$ the divergent piece of the one loop

contribution is exactly canceled by the product of two real emission diagrams. A detailed analysis of infrared phenomena can be found in [59].

If we obtain the two real emission diagrams from the loop diagram in the way shown above, momentum conservation is violated in both graphs at some vertex. This happens, because the initial delta function conserving the momenta of the external particles in the initial loop diagram is still present in the real emission diagrams. The additional particle violates momentum conservation. Although the integration measure is the same in both cases, the true real emission diagrams are accompanied by a delta function $\delta(P-\sum q_f - q_\gamma)$ conserving overall momentum.

Momentum conservation at some vertices is also violated in the soft photon approximation, e.g. cf [21, 59]. Here, following the same reasoning as above, the contribution of real emission diagrams in the soft limit is approximated by the born amplitude times a prefactor. This factor can be evaluated analytically when regulated by a photon mass. Adding this result to the analytic results of loop graphs, the divergent terms, logarithms of the photon mass, cancel.

If we want to evaluate the soft real emission diagrams and the loop corrections under the same integral, we need a method of implementing the projection of the, say $2 \to n + \gamma$ graphs onto the $2 \to n$ graphs. Following the soft photon approximation, we could add the product of two real emission diagrams with momentum violation at the first vertex after the emission of the massless particle. However, adding the product of the two diagrams will only cancel the infrared divergence in the product of the loop graph with the born amplitude.

We intend to apply the Feynman Tree Theorem to single amplitudes and compute the interference with the born terms after summation of all contributing amplitudes. Applying the Tree Theorem to products of loop and Born amplitudes would lead to a drastic increase of the number of terms, if a process with several Born terms is considered.

We therefore would like to have a prescription of incorporating the effect of real emission diagrams in single amplitudes. A rather drastic step would be to set the term with the cut propagator associated with the massless particles to zero for $|\vec{k}| < \Delta E_s$. In a sense this is close to what is done in the soft photon approximation, where only the singularity in the denominator is contributing and all further dependences on the momentum of the massless particle are neglected [21]. Setting the cut loop integral zero in the soft region transfers this method of approximation also to this amplitude. A more elegant way would be to change the numerator of the propagator adjacent to the incoming massless particle to

$$\not{p} + \not{k} + m \to \theta(|\vec{k}| - \Delta E_s)(\not{p} + m) + \not{k}, \tag{3.78}$$

This mimics the addition of a real emission diagram with k dependence only in the singular propagator times a real emission diagram where the momentum k is kept through

almost all lines of the diagram. Since in our calculations, cf. chapters 5 and 6, we used a rather small value for the soft energy cutoff ΔE_s of about 1% of the center of mass energy $\sqrt{s}$, the error resulting from the proposed methods as well as the differences between their contributions to the final result are negligible. In the results presented in chapter 5, we set the term of cut photons to zero below ΔE_s. A comparison with the FeynArts result shows no deviation.

There is a one to one correspondence between the interference terms of Born amplitudes with loop diagrams with a cut massless particle and the product of two diagrams with real emission of this particle. This means that for any virtual infrared divergence in an unrenormalized loop we have a product of two real emission diagrams with emission of this particle from external legs. If these legs are not identical, the product of the two real emission diagrams comes with a factor 2, which is the case for the interference term of the loop corrections with the Born matrix elements as well. However, there are still infrared divergent terms left. On the one hand those which correspond to the square of one real emission diagram and therefore would correspond to the self-energy correction to an external particle, which we set to zero in the on-shell renormalization scheme. On the other hand, further infrared divergent contributions are coming from subtraction diagrams. In the following section we will argue that by a certain choice of the subtraction diagrams all infrared divergences cancel.

3.3.2. UV Subtraction Terms

In QED, there are three primitively ultraviolet divergent graphs Γ, cf. section 2.4. These are the photon and electron self-energy and the vertex correction. The renormalized one loop photon self-energy is given in appendix B. It is infrared finite. In the following we will argue that the infrared divergent terms of the square of real emission diagrams and of the electron self-energy will be compensated by the subtraction diagrams of the vertex correction.

Consider an amplitude $\mathcal{M}_0$ with an incoming on-shell electron with momentum p and mass m. It is attached to a vertex v. If we radiate off a photon from the electron line and square the amplitude, the infrared divergent term can be obtained from soft photon approximation and reads:

$$I_{re} = -e^2|\mathcal{M}_0|^2 \cdot \int^{\Delta E_s} \frac{d^3k}{(2\pi)^3 2|\vec{k}|} \frac{m^2}{(pk)^2}. \tag{3.79}$$

The radiative correction to the vertex v is infrared divergent if the outgoing fermion line is on-shell. As shown in section 3.3.1, this divergence is canceled by the product of two real emission diagrams with the photon attached to the incoming and outgoing fermion line, respectively. As argued in section 2.4, to relate experimental results with theoretical calculations we subtract the vertex correction at the Thomson limit where the momentum of the photon attached to the vertex v is zero and the fermion going through the vertex is on-shell. If we split the subtraction term in two pieces, where in one term the on-shell

fermion line through the vertex v is aligned with the incoming electron and in the second term aligned with the outgoing fermion, the loop contribution of one of these terms is

$$\frac{1}{2}(ie^2)\int \frac{d^4k}{(2\pi)^4}\cdots\frac{\gamma_\alpha(\not{p}+\not{k}+m)\gamma_\mu(\not{p}+\not{k}+m)\gamma^\alpha}{k^2(k^2+2pk)^2}\cdots, \tag{3.80}$$

where we explicitly pulled out the couplings $-ie$ from the γ_α and the factors $i, -i$ coming from the propagators. As can be seen from (3.80), the ultraviolet contribution of the subtraction terms are independent from the external momenta of the vertex correction. Thus, the subtraction graph can be split in parts with different momentum assignments without harming the cancellation of the UV divergence.

Cutting the photon line of the loop with momentum k and neglecting terms proportional to k in the numerator we get:

$$\frac{e^2}{2}\int \frac{d^3k}{(2\pi)^3 2|\vec{k}|}\cdots\frac{-4mp_\mu}{(2pk)^2}\cdots. \tag{3.81}$$

If we *straighten* the fermion line such that throughout the graph it has the on-shell momentum p, this fermion line can be written as a chain of products of Dirac wave functions and γ-matrices:

$$\ldots\bar{u}(p)\gamma_\kappa u(p)\bar{u}(p)\gamma_\lambda u(p)\bar{u}(p)p_\mu u(p)\bar{u}(p)\ldots \tag{3.82}$$

where at the place of the former vertex correction only a factor proportional to p_μ remains. Making use of the Gordon identity

$$\bar{u}(p)p_\mu u(p) = m\bar{u}(p)\gamma_\mu u(p), \tag{3.83}$$

the infrared divergent term can be factored out of the amplitude and is a Lorentz scalar:

$$-\frac{e^2}{2}\int \frac{d^3k}{(2\pi)^3 2|\vec{k}|}\frac{4m^2}{(2pk)^2}\cdot\mathcal{M}_0'. \tag{3.84}$$

Here, $\mathcal{M}_0'$ is the matrix element $\mathcal{M}_0$ with all lines attached to the fermion line bearing zero momentum. Since we factored out the infrared divergent part, we can divide by the amplitude $\mathcal{M}_0'$ and multiply by $\mathcal{M}_0$. In explicit calculations we therefore subtract the amplitude with the vertex correction holding the fermion line straight and neglecting the denominator of the rest of the amplitude which does not belong to the loop. We then divide by the same amplitude without vertex correction and multiply by the basic amplitude $\mathcal{M}_0$. Doing so, we apply the correct subtraction terms to the unrenormalized loop graph in the sense that in the limit, where the momentum of the photon attached to v vanishes, the one loop graph and the subtraction graphs cancel each other. This leaves the born graph, which just contains the electric charge at the vertex, $ie\gamma_\mu$, as required by the renormalization conditions. Since the ultraviolet contributions of the subtraction graphs are independent of the external momenta ab initio, this procedure does not invalidate the UV cancellation.

The resulting infrared divergent term of the interference with the amplitude $\mathcal{M}_0$, which comes with a factor 2 in the final cross section, becomes:

$$I_{v_1} = -e^2|\mathcal{M}_0|^2 \cdot \int \frac{d^3k}{(2\pi)^3 2|\vec{k}|} \frac{m^2}{(pk)^2}, \tag{3.85}$$

which exactly cancels the above infrared divergent term (3.79) of the soft real emission when subtracted from the unrenormalized vertex correction. The second half of the subtraction term I_{v_2} is equivalent to I_{v_1} with p replaced by the on-shell momentum $\bar{q}$ of the outgoing fermion. If this is an external particle, the infrared divergence is canceled by the corresponding real emission diagrams and we are finished. This case is summarized in figure 3.3. On the left hand side we depicted the renormalized vertex correction. The coefficients are given by $c_i = \mathcal{M}_0 \mathcal{M}_0^{'-1}(p_i)$. When the photon lines of the loops are cut, the infrared divergences arising in the interference term are canceled by the real emission diagrams shown on the right hand side.

If the outgoing fermion belongs to an internal line, we will show in the following that the infrared divergent part is canceled by the subtraction terms to the self-energy correction to this internal line.

As was shown in section 2.4, in the case of an self-energy correction to an internal charged fermion line, we need two subtraction terms to cancel the UV divergence. We subtract the same graph at an on-shell momentum $\bar{q}$ aligned to the original momentum q and the derivative of the self-energy with respect to q at $\bar{q}$. The relevant part of this diagram is given by the electron self-energy

$$-e^2 \cdot \int \frac{d^4k}{(2\pi)^4} \cdots \frac{\gamma_\alpha(\not{q} + \not{k} + m)\gamma^\alpha}{k^2((k+q)^2 - m^2)} \cdots . \tag{3.86}$$

Replacing q by $\bar{q}$ does not even lead to an infrared singular term, since the singularity in the denominator is canceled by the integration measure. Making use of the identity

$$\frac{\partial}{\partial q^\mu} \frac{i}{(\not{k} + \not{q} - m)} = \frac{i}{(\not{k} + \not{q} - m)} i\gamma_\mu \frac{i}{(\not{k} + \not{q} - m)}, \tag{3.87}$$

the second subtraction term can simply be obtained by straightening the fermion line through the self-energy part, insertion of a Dirac gamma matrix γ_μ in the fermion line and multiplying by $(q - \bar{q})^\mu$:

$$-e^2 \cdot \int \frac{d^4k}{(2\pi)^4} \cdots \frac{\gamma_\alpha(\not{\bar{q}} + \not{k} + m)(\not{q} - \not{\bar{q}})(\not{\bar{q}} + \not{k} + m)\gamma^\alpha}{k^2((k+\bar{q})^2 - m^2)^2} \cdots . \tag{3.88}$$

Cutting the photon line and simplifying the numerator, the divergent part is

$$-ie^2 \cdot \int \frac{d^3k}{(2\pi)^3 2|\vec{k}|} \frac{q\bar{q} - m^2}{(\bar{q}k)^2} \cdots (\not{\bar{q}} - 2m) \cdots . \tag{3.89}$$

We can again interpret the fermion line as a chain of Dirac wave functions. Thus, the factor $(\not{\bar{q}} - 2m)$ simplifies to $(-m)$. With the use of the Gordon identity (3.83), the term

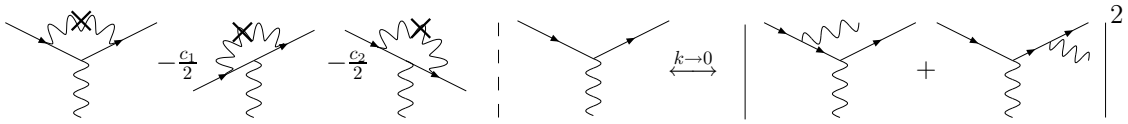

Figure 3.3: UV-IR Subtraction Terms: The vertex correction is renormalized by the subtraction of two graphs with zero incoming photon momentum. When the photon propagator of the loops is cut, the arising infrared divergences in the interference term are compensated by the product of real emission diagrams depicted on the right hand side.

$q\bar{q} - m^2 = (q - \bar{q})^\mu \bar{q}_\mu$ can be seen as m times $\mathcal{M}_0'$, the amplitude with an insertion of $i\gamma_\mu$ times $(q - \bar{q})^\mu$ at the place of the original self-energy correction. Like in the case of the vertex correction we then have a Lorentz scalar factored out of the amplitude $\mathcal{M}_0'$ with a straight fermion line. Dividing by this amplitude, multiplying the Born amplitude $\mathcal{M}_0$ and again with $2\mathcal{M}_0$ to calculate the interference term contributing to the cross section, the infrared divergent part of the subtraction terms to the electron self-energy is

$$I_\Sigma = 2e^2 |\mathcal{M}_0|^2 \cdot \int \frac{d^3k}{(2\pi)^3 2|\vec{k}|} \frac{m^2}{(\bar{q}k)^2}. \tag{3.90}$$

When subtracted from the unrenormalized self-energy correction, half of the infrared divergent term cancels the contribution coming form the subtraction graph of the vertex correction I_{v_2}, obtained from (3.85) by replacing p with $\bar{q}$. Following the fermion line further we again come to a vertex and its correction terms will cancel the second half of the infrared divergent term of the subtraction graphs of electron self-energy. This goes on until the last vertex, where the second infrared contribution of its subtraction graphs will then be compensated by the squared amplitude of the real emission of a photon of the external line following this vertex.

This completes our renormalization prescription, which trivially extends to processes with multiple born graphs. We constructed subtraction graphs which cancel all possible ultraviolet divergences and give further infrared divergent contributions such that in the sum of all graphs contributing to a given process the infrared divergences cancel. Furthermore the renormalized vertex functions obey the renormalization conditions (2.31-2.34) such that the experimentally measured observables can directly be related to the theoretical predictions without any further analytic correction.

We showed that in QED we have a complete prescription to incorporate the on-shell renormalization scheme and cancel all infrared and ultraviolet divergences. Although not rigorously proven, this method should also be applicable to the electroweak standard model. Subtraction graphs to only ultraviolet divergent vertices can be found by the introduced BPHZ mechanism. In case of a photonic correction, where infrared divergences are expected, the proposed method of this section should also lead to finite results. Specifically, we checked this for a eWν vertex, where the infrared divergence coming from the

real emission of the charged external particles is canceled by the subtraction terms if the momentum of the W-boson is aligned with the electron momentum: $p_W = \frac{M_W}{m_e} p_e$. Then the mass factors out and is canceled by terms in the numerator coming from the WWA coupling and we get a squared propagator leading to the same contribution as in the real emission diagrams.

3.3.3. Collinear Peaks

Consider the part of a loop graph depicted in figure 3.4. In the following we will examine the peak structure of the collinear peaks. We will see that both, terms with a cut fermion and a cut photon in (3.15) can develop a collinear peak. In the sum, these cancel except in parts of the phase space, where only one of the peaks is developed. We will also show explicitly the occurrence of several of the singularities discussed in the previous sections. The interesting part of the denominator reads:

$$\left[(k+p_a)^2 - m_1^2\right]\left[(k+p_b)^2 - m_2^2\right]\left[(k+p_c)^2\right], \tag{3.91}$$

where

$$p_a - p_c = a p_1, \tag{3.92}$$
$$p_b - p_c = -b p_2, \tag{3.93}$$
$$p_1^2 = m_1^2, \tag{3.94}$$
$$p_2^2 = m_2^2, \tag{3.95}$$

and (a, b) are $+1$ for incoming and -1 for outgoing particles, respectively. p_1 and p_2 are external on-shell particles with $p_i^0 > 0$.

Threshold Singularity

We begin with the internal singularity which might occur when one of the fermion propagators is cut and the second gets singular at a hypersurface in the integration volume. In section 3.2.1, we stated the two conditions 3.40 and 3.41 which have to be fulfilled in this case. For the invariant square of $p_{ji} = p_j - p_i$ we get:

$$\begin{aligned} (p_a - p_b)^2 &= (a p_1 + p_c - p_c + b p_2)^2, & (3.96)\\ &= m_1^2 + m_2^2 + 2ab p_1 p_2. & (3.97) \end{aligned}$$

The scalar product of two on-shell four-vectors is always equal or bigger than the product of the two masses:

$$p_1 p_2 \geq m_1 m_2. \tag{3.98}$$

With this we get:

$$p_{ji}^2 = m_1^2 + m_2^2 + 2ab p_1 p_2 \begin{cases} > (m_1+m_2)^2 & \text{for} \quad (ab) = (ii, oo) \\ < (m_1-m_2)^2 & \text{for} \quad (ab) = (io, oi) \end{cases} \tag{3.99}$$

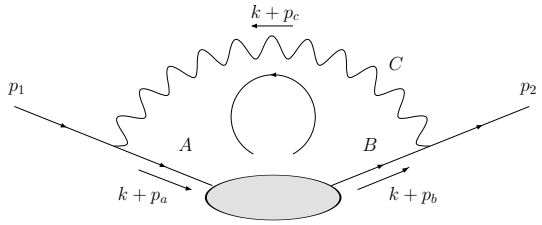

Figure 3.4: Typical example for the occurrence of infrared, collinear and threshold singularities. p_1 and p_2 may be incoming or outgoing on-shell particles.

The kinetic function λ is therefore strictly positive and in the case of one incoming and one outgoing particle if there are singularities, they cancel each other as shown in section 3.2.1. This corresponds to the region II in figure 3.1. The result also extends to the case $p_{ji}^2 < 0$ (I). For positive p_{ji}^2, we can find a rest frame of $p_j - p_i$ and replace p_{ji}^2 with ${p_{ji}^0}^2$ in (3.99).

If both particles are incoming or outgoing the integral develops an imaginary part (IV). Note that $(p_a - p_b)^0$ is negative for two outgoing particles and condition (3.40) is fulfilled and vice versa $(p_b - p_a)^0$ is negative for two incoming particles. This means that the singularity will show up when we cut the propagator with the loop momentum flowing in the same direction as the four momentum of the adjacent external particle. In the upper example of figure 3.4 this is propagator A for two incoming and propagator B for two outgoing particles.

In the rest frame of the two momenta $\vec{p}_a = \vec{p}_b$, which is also the rest frame of the two external particles, the peak is given by (3.39). For equal masses this simplifies to:

$$\mathbf{k}_s = \mathbf{p}, \tag{3.100}$$

where $\mathbf{p}$ is the absolute value of the three momentum of the external particles in this rest frame.

In the following we will investigate in which regions the terms of the integrand become large due to virtual collinear singularities.

Collinear Structure

Cutting the photon propagator, the denominator of propagator A reads:

$$\begin{aligned}(k+p_a)^2-m_1^2 &= (k+p_c+p_a-p_c)^2-m_1^2,\\ &= 2ap_1(k+p_c),\\ &= 2a\left[p_1^0\sqrt{(\vec{k}+\vec{p}_c)^2}-\vec{p}_1(\vec{k}+\vec{p}_c)\right].\end{aligned} \tag{3.101}$$

This becomes zero iff $\vec{k}=-\vec{p_c}$. Since it is the product of two on-shell four-vectors with positive zero component it is always greater than zero except for the vanishing of one of the four-vectors. In this limit we have the expected IR-divergence. Its occurrence is independent of a and is equally valid for incoming and outgoing particles. Propagator B has the same structure. It gets singular iff the momentum of the photon in the loop vanishes: $\vec{k}=-\vec{p_c}$. Together with the phase space factor $\frac{1}{2}|\vec{k}+\vec{p_c}|^{-1}$, which remains after cutting the photon propagator we have a singularity proportional to $|\vec{k}+\vec{p_c}|^{-3}$ yielding a logarithmic divergence.

The peak structure in (3.101) is not symmetric around $\vec{k}=-\vec{p_c}$. It is the endpoint of a collinear peak. If the momentum of the photon is in the direction of the external particle, the relevant part of the integrand gets proportional to the squared mass of the fermion and therefore very small for high energy reactions involving light fermions. We parameterize the loop momentum by $\vec{k}+\vec{p}_c=xa\vec{p}_1$, getting:

$$A^C_{coll_1}=2a\left[\sqrt{\mathbf{p}_1^2+m_1^2}\mathbf{p}_1|x|-\mathbf{p}_1^2xa\right], \tag{3.102}$$

where $A^C_{coll_1}$ stands for the denominator of propagator A along the direction of $\vec{p}_1$ when propagator C is cut. This is of $\mathcal{O}(m_1^2)$ if $ax>0$, when the momentum of the photon propagator is pointing in the same direction as the momentum of the external particle. In this case the part of the integrand which develops a peak is:

$$2\sqrt{(\vec{k}+\vec{p}_c)^2}\,A^C_{coll_1}=...=2x^2a\mathbf{p}_1\cdot m_1^2+\mathcal{O}(m_1^4),\quad \text{for } ax>0. \tag{3.103}$$

We can perform the same analysis on the photon propagator when propagator A is cut.

$$\begin{aligned}C^A_{coll_1} &= (k+p_c+p_a-p_a)^2,\\ &= 2m_1^2-2ap_1(k+p_a),\\ &= ...\\ &= 2m_1^2-2a\sqrt{\mathbf{p}_1^2+m_1^2}\sqrt{(x+1)^2\mathbf{p}_1^2+m_1^2}+\mathbf{p}_1^2(x+1).\end{aligned} \tag{3.104}$$

This is of $\mathcal{O}(m_1^2)$ if $a(x+1)=|x+1|$. In the regions where both conditions are fulfilled the two singularities cancel. The singular part, when propagator A is cut, is given by (3.104) and the phase space factor:

$$2\sqrt{(xa\vec{p}_1 + a\vec{p}_1)^2 + m_1^2}\, C^A_{coll_1} = ... = -2x^2 a\mathbf{p}_1 \cdot m_1^2 + \mathcal{O}(m_1^4), \quad \text{for } a(x+1) = |x+1|. \tag{3.105}$$

The analytic rests of the integrands are multiplied by a delta function setting the momentum of the cut propagator on-shell. The resulting integrands of the two cuts differ only by terms of $\mathcal{O}(m_1^2)$. Setting $s = 2x^2 a\mathbf{p}_1$ and writing r for the non-singular rest of one of the integrand, we have:

$$\frac{r}{sm_1^2 + \mathcal{O}(m_1^4)} + \frac{r(1+\mathcal{O}(m_1^2))}{-sm_1^2 + \mathcal{O}(m_1^4)} = \frac{r \cdot \mathcal{O}(m_1^4)}{-s^2 m_1^4 + \mathcal{O}(m_1^6)} = \mathcal{O}(m_1^0). \tag{3.106}$$

Thus, the former enhancement of the integrand due to the factor m^{-2} vanishes if the two conditions are fulfilled. The region where only one condition is fulfilled is given by

$$-1 < x < 0. \tag{3.107}$$

Therefore, the peak arises on the line $\vec{k} + \vec{p}_c = (0, -a\vec{p}_1)$.

The form of propagator B along the collinear peak is also of interest. If the photon propagator is cut this contribution is, in the limit of zero masses,

$$B^C_{coll_1} = -2b\,(\mathbf{p}_1\mathbf{p}_2|ax| - ax\vec{p}_1\vec{p}_2) + \mathcal{O}(m_1^2, m_2^2). \tag{3.108}$$

In the region where the integrand develops a peak, $ax > 0$, this becomes:

$$B^C_{coll_1} = -2abx\,(\mathbf{p}_1\mathbf{p}_2 - \vec{p}_1\vec{p}_2) + \mathcal{O}(m_1^2, m_2^2). \tag{3.109}$$

If propagator A is cut, we have:

$$B^A_{coll_1} = 2\mathbf{p}_1^2\,(1 + x - a|1+x|) + 2abx\vec{p}_1\vec{p}_2 + 2b\mathbf{p}_1\mathbf{p_2}(a - |1+x|) + \mathcal{O}(m_1^2, m_2^2), \tag{3.110}$$

which, in the region where $a(x+1) = |x+1|$, simplifies again to

$$B^A_{coll_1} = -2abx\,(\mathbf{p}_1\mathbf{p_2} - \vec{p}_1\vec{p}_2) + \mathcal{O}(m_1^2, m_2^2). \tag{3.111}$$

Note that this contribution is odd in x. This means, if $a = 1$ for an incoming particle, $x = 0$ is in the allowed range and the peak changes sign at this point. Thus, we do not have a divergent term as could be inferred from the x^3 factor. In the case of the cut photon line the collinear peak starts at $x = 0$ and goes either in the direction of $\vec{p}_1$ for an incoming particle or $-\vec{p}_1$ for an outgoing particle.

In the case of the second collinear peak along the direction of p_2, the above analysis repeats if we interchange $x \leftrightarrow y$, $1 \leftrightarrow 2$, $p_a \leftrightarrow p_b$, and $a \leftrightarrow -b$. We summarized this in table 3.1.

	Singular Factor	Photon Cut	Fermion Cut	Range of Peak
Peak 1	$4abx^3\vec{p}_1^2 m_1^2 \left(\lvert\vec{p}_1\rvert\lvert\vec{p}_2\rvert - \vec{p}_1\vec{p}_2\right)$	$ax > 0$	$a(x+1) = \lvert x+1\rvert$	$\vec{k} + \vec{p}_c = (0, -a\vec{p}_1)$
Peak 2	$4abx^3\vec{p}_2^2 m_2^2 \left(\lvert\vec{p}_1\rvert\lvert\vec{p}_2\rvert - \vec{p}_1\vec{p}_2\right)$	$by < 0$	$-b(y+1) = \lvert y+1\rvert$	$\vec{k} + \vec{p}_c = (0, b\vec{p}_2)$

Table 3.1: Contributions to the collinear peaks from the cuts of the photon line and the fermion lines, respectively.

The point with $x = 0$ or $y = 0$, is critical for the numerical evaluation. In case of the photon cut we obtain the infrared divergence discussed in section 3.3.1. This was canceled by the addition of real emission diagrams. However, if we do so we might get a further rapidly varying term from the fermion cuts in this region. In the above analysis this would be the case for $a = 1$ and $b = -1$, whenever the loop momentum is in the same direction as the external particle for a given propagator. Originally, the two enhanced contributions coming from the photon cut and the fermion cut canceled each other for $x, y < 0$. Adding the real emission graphs or cutting out the contributions from the photon cut at $k < \Delta E_s$ leaves the enhanced contribution from the fermion cut. Then, the peak changes sign at $x = 0$ or $y = 0$, respectively. Sometimes, these peaks can be avoided by changing the sign of the loop momentum. Then, at the infrared pole the collinear peak only stems from the photon cut and subtraction methods for the IR divergence can be applied without concern. But in many cases this problem is just shifted to another infrared pole of the original loop.

If it is unavoidable that the collinear peak gets a contribution from the fermion cut at the infrared pole, as discussed in section 3.3.1 we can again argue that the main contribution in this region is given by the peak. Since this is an odd function in x or y this main contribution vanishes if integrated over a small region $k < \Delta E_s$. Therefore, the error would be small if we again cut this region out of the integrand. If the origin of the three-dimensional integration momentum would coincide with the infrared point and we aligned the z-axis with the collinear peak and evaluated the integrand in spherical coordinates, the peak would be suppressed by the integration measure and the integrand could be evaluated rather easily. In general, there are several collinear peaks and infrared poles in the integrand. A method to evaluate such integrands which still makes use of the cancellation of peaks by the integral measure is the multi channel approach. We will discuss this in the next chapter.

In the case of two incoming or two outgoing particles, it often happens that $\vec{p}_1 = -\vec{p}_2$, as is the case for $2 \to n$ scattering evaluated in the center of mass system. Here, the two peaks coincide. Furthermore, a threshold singularity arises around the endpoint of the collinear peak at $x = -1$ or $y = -1$ with radius given by (3.39) or by $\mathbf{k}_s = \mathbf{p}_1$ if the two masses coincide. In this case we add a fix function to the integrand. However, at the infrared point $x = 0$ this function does not smooth the peak structure, because here, the collinear peak and the peak from the threshold singularity meet. Again we can cut the integrand around this point.

The endpoints $x = -1$ and $y = -1$ can be the starting points of further collinear peaks if the corresponding propagators are again connected to another external on-shell particle and a massless boson. From this, one can deduce the peak structure of a Feynman graph. We will do this for several box and triangle graphs in QED, when we discuss Bhabha scattering in chapter 5.

Summary

This concludes the body of this thesis. In the preceding chapter, we presented a method to compute loop integrals from a sum of tree graphs. We gave the construction of subtraction terms from the BPHZ mechanism to cancel ultraviolet divergences and showed the cancellation of infrared divergences when real emission graphs are added to the tree graphs originating from cutting a photon propagator in the original loop diagram. We studied the peak structure from threshold singularities and gave the construction of fix functions to smooth these peaks.

The resulting integrand will in general still have a peak structure due to collinear singularities. In the next section, we will review different integration algorithms, which can adapt to these peaks and allow for an efficient numerical evaluation.

In chapters 5 and 6, we will, as a proof of principle, apply the presented method to cross section integration and event generation for NLO Bhabha scattering. This will include box graphs as the most complicated loop integrals. However, as can be seen from the preceding chapter, this method is in general not restricted to any number of external legs.

4. Phase Space Integration

After creation of the matrix element in the form discussed in the previous chapter, the integration over the loop momentum has to be performed. The aim is to find an algorithm such that the integration of the loop momentum and of the phase space of the final states can be performed in parallel. Thus, instead of the $(3n-4)$-dimensional integral of the squared Born level matrix element, we have a $(3n-1)$-dimensional integration of the interference term of the one loop correction with the Born amplitude. The final goal is to implement the one loop corrections into a Monte Carlo event generator such that for a set of possible final state momenta also a loop momentum is drawn and the matrix element evaluated. This will be presented in chapter 6.

In the following, we will give a brief introduction to Monte Carlo integration techniques, which is mainly based on [60, 61]. We will also discuss the decomposition of an n-particle phase space and its parameterization for an efficient integration. The integration over the loop momentum of the matrix element obtained by the Feynman Tree Theorem is essentially a phase space integration of one additional particle in the initial and final state. Therefore, the methods presented in this chapter will also apply for the loop integration.

4.1. Monte Carlo Integration

We want to give an estimate of the d-dimensional integral:

$$I = \int du f(u), \tag{4.1}$$

where $u = (u_1, \ldots, u_d)$. For simplicity we assume u to lie in the unit hypercube, which can always be accomplished by a suitable mapping or rescaling of the integration variables:

$$u \in [0,1]^d. \tag{4.2}$$

In usual high energy applications the integral (4.1) cannot be evaluated analytically. The integrand $f(u)$ often includes experimental cut functions and acceptances for the external momenta and the phase space measure also gets a complex structure when going to higher dimensions. In one dimension there exist many algorithms to numerically approximate I with errors proportional to N^{-p}, where N is the number of samples and p a low integer dependent on the chosen algorithm. Applying these methods in every dimension to a d-dimensional integral, the error then becomes proportional to $N^{-\frac{p}{d}}$ and the convergence gets poor for higher d.

If we evaluate the integrand $f(u)$ of (4.1) at N uniformly distributed random values of u, we get the estimate:

$$\langle f \rangle = \frac{1}{N} \sum_{n=1}^{N} f(u_n). \tag{4.3}$$

In the limit of $N \to \infty$ this converges to the value I. The variance of $f(u)$ is given by:

$$\sigma^2(f) = \int du\,(f(u) - I)^2\,. \tag{4.4}$$

The variance of the Monte Carlo result can then be estimated by:

$$\int \left(\prod_{n=1}^{N} du_n\right) \left(\frac{1}{N}\sum_{n=1}^{N} f(u_n) - I\right)^2 = \frac{\sigma^2(f)}{N}. \tag{4.5}$$

Thus, the error of the Monte Carlo estimate is proportional to $N^{-\frac{1}{2}}$ and independent of the dimension d. Therefore, from a certain amount of dimensions on, the Monte Carlo method is preferable to most other algorithms. Since we do not know the underlying distribution $f(u)$, in practical applications the sample variance is used:

$$s^2(f) = \frac{1}{N-1}\left(\langle f^2\rangle - \langle f\rangle^2\right). \tag{4.6}$$

The factor of $(N-1)^{-1}$ instead of N^{-1} corrects the bias coming from the fact that the mean and the variance are estimated from the same sample. The estimate of the sample variance is equal to the variance of the underlying distribution. In typical high energy processes integrands vary over many order of magnitudes mainly due to singular and collinear peaks. It becomes necessary to increase the performance of the algorithm by reducing the variance. In the following, we will discuss two widely used techniques for this reduction.

4.1.1. Stratified Sampling

The idea of stratified sampling is to split the integration volume into k sub-volumes and perform a Monte Carlo integration in each sub-volume with N_i samples. The expectation value for the integral I is just the sum of the expectation values of the integrand in the sub-volumes times the size of the volume:

$$\langle f\rangle = \sum_i V_i \langle f\rangle_i. \tag{4.7}$$

However, the variance is now given by:

$$\sigma^2 = \sum_i V_i^2 \frac{\sigma_i^2}{N_i}, \tag{4.8}$$

where σ_i^2 is the variance of the sampled sub-volume i. It then turns out that the total variance is minimized if the number of samples N_i in sub-volume i is proportional to σ_i. The number of sub-volumes rises exponentially with the number of dimensions. For multi-dimensional integrals this method can therefore get inefficient in terms of computing time.

4.1.2. Importance Sampling

Changing the integration measure du to a new one $dG(u)$, with the corresponding Jacobian

$$g(u) = \frac{d^d G(u)}{du_1 \dots du_n}, \tag{4.9}$$

we get for the integral (4.1):

$$I = \int dG(u) \frac{f(u)}{g(u)}. \tag{4.10}$$

If we use a positive definite function $g(u)$ normalized to unity, it can be interpreted as a probability density function. Instead of uniformly distributed random numbers u_i, we can then generate numbers according to the distribution $g(u)du$. This gives the probability of generating a random number between u and $u + du$. Comparing with a uniformly distributed density we have:

$$g(u)du = dx \tag{4.11}$$

We therefore get $x = G(u)$ and $u(x) = G^{-1}(x)$, where $G(u)$ is the indefinite integral of $g(u)$. Thus, we need the inverse of the integral of $g(u)$ to generate random numbers according to the distribution $g(u)du$.

The expectation value then reads:

$$\left\langle \frac{f}{g} \right\rangle = \frac{1}{N} \sum_{n=1}^{N} \frac{f(u_n)}{g(u_n)}, \tag{4.12}$$

and still converges to I in the limit $N \to \infty$. The sample variance now reads:

$$s^2 \left(\frac{f}{g} \right) = \frac{1}{N-1} \left(\left\langle \frac{f^2}{g^2} \right\rangle - \left\langle \frac{f}{g} \right\rangle^2 \right). \tag{4.13}$$

Thus, the variance is reduced if $g(u)$ is close to $f(u)$. To find an adequate function $g(u)$ requires a detailed knowledge of the function $f(u)$. Furthermore, the integral of $g(u)$ is needed for its normalization. The optimal function requires the knowledge of the integral I:

$$g(u) = \frac{|f(u)|}{\int f(u) du}. \tag{4.14}$$

Therefore, for an efficient Monte Carlo integration, a probability density $g(u)$ is favorable which is simple and close in shape to $f(u)$ at the same time.

4.1.3. Adaptive Monte Carlo Algorithms - VEGAS

In case the peak structure of the integrand is not known very well, an adaptive algorithm for integration can be used. Here, the density $g(u)$ is fit iteratively to the integrand. In one dimension this is done by using a step function with variable size of bins:

$$g(x) = \frac{1}{N} \sum_{n=1}^{N} \frac{\theta(x_n - x)\theta(x - x_{n-1})}{x_n - x_{n-1}}. \tag{4.15}$$

Decreasing the size of a bin therefore increases the magnitude of $g(u)$ in this bin and in this way the probability density can be adapted to approximate the optimal value (4.14). For multi dimensional integrals this is implemented in the widely used VEGAS routine [62,63]. Here, for each dimension the probability density is separately adapted according to (4.15). The overall probability function is then given by

$$g(u) = g_1(u_1) \cdots g_d(u_d) \tag{4.16}$$

and defines a hypercubic grid. This grid is adjusted in several iterative stages according to the results in the different cells. The size of the bins is decreased where the integrand has dominant contributions and vice versa. After the grid adaption, the integration with the probability density given by the grid is performed with a larger number of samples. This again can be done iteratively, however, often a further adaption of the grid does not lead to a higher efficiency from a certain iteration on. This fact can be accounted for by a damping factor which avoids a high fluctuation of the state of the grid towards higher iterations.

The method described above resembles importance sampling. The integrand is evaluated with emphasis on the dominant regions. The method of stratified sampling is also implemented in VEGAS. Here, the grid is further divided into sub-cells such that finally in each cell only two samples are taken. This leads to a more uniform distribution of the sample points.

Due to the factorized ansatz (4.16), the VEGAS routine can only adapt to integrands, where peaks lie along the axis of the hypercube. As an example, consider a uniform peak along the bisector $u_2 = u_1$ in the $u_1 - u_2$ plane. Then all points along the u_1- and the u_2-axis will lead to the same contribution and the grid can not be adapted to the peak. In this simple example one can rotate the coordinate system such that the peak is aligned with one axis u_1' of the new coordinates and orthogonal to another, u_2'. Then the grid can be adapted to the peak by decreasing the bin size accordingly on the axis u_2' orthogonal to the peak. Thus, in applications where the peak structure of the integrand factorizes in the sense that the integrand can be mapped onto a coordinate system such that the peaks are located at distinct points or small regions of one of the coordinates the grid can be adapted and the resulting integration is very efficient.

In usual high energy processes, typical integrands have a large number of peaks which do not factorize anymore. In this case the simple factorization ansatz (4.16) of the VEGAS

routine does not lead to a sufficient adaption of the grid to the peak structure of the integrand.

4.1.4. Multi Channel Algorithms

If the integrand does not allow for a simultaneous mapping of the peaks onto a coordinate system where the peaks factorize and one adaptive grid can be used for efficient integration, one has to refer to a generalization of the adaptive Monte Carlo algorithm [14, 64]. These are known as Multi Channel algorithms. For each peak a coordinate transformation is applied such that in this *channel* the considered peak can be adapted to.

We again start with a normalized probability density $g(u)$ and rewrite integral (4.1) as:

$$I = \int \frac{f(u)}{g(u)} g(u) du. \tag{4.17}$$

Suppose we have m different transformations of the integration volume $\Phi_i(x) = u$. We can rewrite $g(u)$ as a sum of probability densities g_i,

$$g(u) = \sum_{i=1}^{m} \alpha_i g_i(\Phi_i^{-1}(u)) \left| \frac{\partial \Phi_i^{-1}(u)}{\partial u} \right|. \tag{4.18}$$

Here, the $g_i(x)$ as well as the sum of the weights α_i are again normalized to unity. Substituting (4.18) in (4.17), we get

$$I = \sum_{i=1}^{m} \alpha_i \int \frac{f(\Phi_i(x))}{g(\Phi_i(x))} g_i(x) dx, \tag{4.19}$$

where $g(\Phi_i(x))$ is then given by

$$\begin{aligned} g(\Phi_i(x)) &= \sum_{j=1}^{m} \alpha_j g_j(\Phi_j^{-1}(\Phi_i(x))) \left| \frac{\partial \Phi_j^{-1}(\Phi_i(x))}{\partial \Phi_i(x)} \right|, \\ &= \left| \frac{\partial \Phi_i}{\partial x} \right|^{-1} \left(\alpha_i g_i(x) + \sum_{j \neq i}^{m} g_j(\pi_{ji}(x)) \left| \frac{\partial \pi_{ji}(x))}{\partial x} \right| \right), \end{aligned} \tag{4.20}$$

with the mappings $\pi_{ji}(x) = \Phi_j^{-1}(\Phi_i(x))$ of the two transformations $\Phi_i(x)$ and $\Phi_j(x)$ from channel j to channel i. The estimate of (4.19) is given by:

$$\left\langle \frac{f}{g} \right\rangle = \frac{1}{N} \sum_{k=1}^{m} \sum_{i=1}^{N_k} \frac{f(x_i)}{g(x_i)}, \tag{4.21}$$

where the number of samples N_k in the channels are distributed according to the weights α_k. This estimate is independent of the weights α_k and these can therefore be adapted to reduce the overall error estimate. We therefore have to minimize the α-dependent part of the variance:

$$W = \sum_{i=1}^{m} \alpha_i \int \left(\frac{f(\Phi_i(x))}{g(\Phi_i(x))} \right)^2 g_i(x) dx. \tag{4.22}$$

The set of α_i which solve the resulting equations for the minimum of (4.22) can be approximated by an iterative adaption, cf. [14]:

$$\alpha_i^{new} = \frac{\alpha_i^{old} W_i^{\beta}}{\sum_i \alpha_i^{old} W_i^{\beta}}. \tag{4.23}$$

The fixed point of this prescription minimizes the overall variance with respect to the weights α_i. Here, W_i is given by:

$$W_i = \left\langle \frac{f(\Phi_i(x))}{g(\Phi_i(x))} \right\rangle_i, \tag{4.24}$$

where the subscript i on the angles indicates the distribution of the sample points according to the probability density $g_i(x)$ of channel i. The parameter β is commonly chosen to lie between $\frac{1}{4}$ and $\frac{1}{2}$, cf. [14, 64]. The update of the weights (4.23) guarantees that channels with a higher variance are emphasized during the sampling which results in a faster convergence of the estimate (4.21).

If the channels are chosen such that each peak structure of the integrand factorizes in at least one channel the resulting gain of the faster convergence of the integral estimate can exceed the additional computation costs of the transformations Φ_i and the corresponding Jacobians and mappings to other channels as well as the adaption of the weights α_i.

The multi channel algorithms are only useful if the peak structure of the integrand is roughly known. In the next section we will discuss the parameterization of the phase space of the external particles in scattering processes, which is used to the define the channels in the algorithm VAMP.

4.2. Phase Space Decomposition

For a $2 \to n$ scattering process even the tree level matrix elements have a rich peak structure in specific regions of the phase space. This structure results mainly from propagators of single Feynman amplitudes. If the phase space can be mapped such that the peaks of an amplitude are correlated only to a single integration variable, the integration routines described in the previous section are able to adapt to the peak structure of this amplitude. Performing the phase space parameterization for each Feynman diagram of the given process, one can use the multi channel approach to adapt to the peak structure of the whole integrand by using in each channel a suitable coordinate parameterization for one Feynman graph, therefore leading to an efficient integration or event generation [65, 66]. This decomposition of the phase space and subsequent automatic multi channel integration is widely used in general purpose event generators. In the following we will shortly review

the phase space decomposition and the construction of appropriate weights to distribute the samples of the phase space close to the integrand.

n-Particle Phase Space

The n-particle phase space $d\Pi(P; q_1, \ldots, q_n)$ as given in (2.54) can be described as a convolution of phase spaces with less particles in the final states:

$$d\Pi_n(P; q_1, \ldots, q_n) = \prod_{i=1}^{m} dQ_i^2 \; d\Pi_m(P; Q_1, \ldots, Q_m) \times \\ d\Pi_{n_1}(Q_1; r_1^1, \ldots, r_{n_1}^1) \ldots d\Pi_{n_m}(Q_m; r_1^m, \ldots, r_{n_m}^m), \quad (4.25)$$

where we suppressed any factors of 2π. The initial four momenta q_i are arbitrarily distributed among the subsets r_i^1 to r_i^m. Using this decomposition iteratively, we can build the n-particle phase space of a given Feynman graph according to its vertex structure out of separate two- or three-body phase spaces.

As an example consider the graph depicted in figure 4.1. Here, the four particle phase space of the final state particles can be decomposed into:

$$d\Pi_n(s; q_1, \ldots, q_4) = dQ_{12}^2 dQ_{34}^2 d\Pi_2(s; Q_{12}, Q_{34}) d\Pi_2(Q_{12}; q_1, q_2) d\Pi_2(Q_{34}; q_3, q_4). \quad (4.26)$$

The lower and upper limits on the invariant mass squared Q_{12}^2 are given by $(m_1+m_2)^2$ and $s-(m_3+m_4)^2$ and analogous for Q_{34}^2. The two particle phase spaces can be parameterized as

$$d\Pi_2(Q_{12}; q_1, q_2) = \frac{1}{2Q_{12}^2} \lambda^{\frac{1}{2}}(Q_{12}^2, q_1^2, q_2^2) d\cos\theta_{12} d\phi_{12}. \quad (4.27)$$

Here, λ is the kinetic function defined in (3.28) and $\cos\theta_{12}$ and ϕ_{12} are the polar and azimuthal angle in the rest frame of Q_{12}, where θ_{12} is the angle between particle 1 and the direction of the spatial part of Q_{12} before the boost into the rest frame. In case of a t-channel propagator, one can use the Mandelstam variable t of the transferred momentum instead of the polar angle θ, cf. [65] for details and corresponding limits. Another possibility, which is used in `WHIZARD`, is to flip the t-channel graph into the corresponding s-channel one, use the same parameterization as before and flip back again, cf. [32].

Construction of Probability Densities

The decomposition of the phase space (4.25) allows us to construct probability densities which are close in shape to the peak structure of the integrand. Propagators of graphs can show singular behavior in the invariant mass square or as a function of an angular parameter.

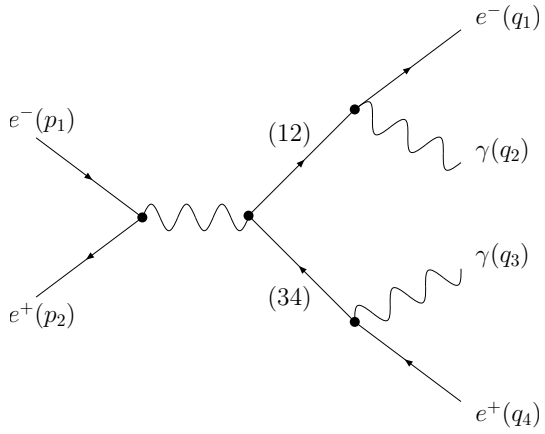

Figure 4.1: Simple graph of $e^+e^- \to e^+e^-\gamma\gamma$ with two collinear peaks.

In the example of figure 4.1, we expect collinear peaks of the propagators (12) and (34). These will lead to a peak in the limit $\cos\theta_{12} \to 1$ and $\cos\theta_{34} \to 1$, respectively. With the help of the phase space decomposition (4.26) and the subsequent parameterization of the two body decays (4.27) we can change the integration variable such that the collinear peak structure is compensated by the Jacobian of this transformation. The peak is of the form:

$$g(\cos\theta) = \frac{1}{(a - \cos\theta)}, \tag{4.28}$$

with $a \geq 1$. Following the prescription for importance sampling in section 4.1.2, we change to a new variable of integration y by calculating the integral of $g(\cos\theta)$:

$$y(\cos\theta) = \int_{-1}^{\cos\theta} g \; d\cos\theta' = \log\frac{a+1}{a-\cos\theta}. \tag{4.29}$$

Dividing $y(\cos\theta)$ by $y(1)$, we get a new variable of integration with borders given by the unit interval $[0, 1]$:

$$x(\cos\theta) = \frac{\log(a+1) - \log(a-\cos\theta)}{\log(a+1) - \log(a-1)}. \tag{4.30}$$

Thus, changing integration variables from $\cos\theta$ to x, the Jacobian of this transformation will cancel the collinear peak of the integrand. The variable $\cos\theta$ will be replaced by the inverse of (4.30):

$$\cos\theta(x) = a - (a+1)\left(\frac{a-1}{a+1}\right)^x. \tag{4.31}$$

Starting with a uniform probability distribution of samples of x among the interval $[0, 1]$, we get a distribution of $\cos\theta$ given by (4.31) which dominates in the region of the collinear

peak of the integrand. We will make use of this mapping of integration variables in the next chapter.

Any variable of integration of the phase space integral can be mapped to the unit interval $[0, 1]$. The emerging Jacobian can be used to smooth peaks of the integrand in the way shown above. This procedure is widely used in Monte Carlo integration routines or event generators. Specific mappings and corresponding weights can for example be found in [65–67]. For each Feynman graph of a process, a channel can be setup. This consists of the transformations of the integration variables of the given graphs to the uniform variables x and the corresponding Jacobians. A final integration of the whole process can then be performed with multi channel algorithms as described in section 4.1.4.

Parameterization of Loop Momentum

The form of the integrands of loop graphs obtained by applying the Feynman Tree Theorem suggests to decompose the phase space including the loop momentum equivalently to the Born level diagrams. This, however, is complicated by the fact that we have a third (in the case of a $2 \to n$ process) incoming particle and an additional outgoing particle with the same momentum. Therefore, the simple limits of the integration of intermediate transferred momenta, which are based on a fixed incoming total energy would become unbounded due to the infinite range of the loop momentum. Furthermore, since the momentum of the additional incoming and outgoing particle are identical the simple decomposition into two body decay phase spaces does not work anymore since there still remains a relation between two different parts of the diagram making it difficult to give a clear definition of a polar and azimuthal angle.

Taking the example of figure 4.1 and interpreting it as one part of the vertex correction to an s-channel $e^+e^- \to e^+e^-$ graph, we would have an additional delta function $\delta(q_2 + q_3)$ relating the photon momenta. Taking, say q_3, as incoming momenta, it becomes clear that a parameterization, which takes the collinear or t-channel peak structure of propagator (34) into account does not help to smooth the peak structure of propagator (12), which is usually taken care of by the 2-particle phase space of the subsequent decay of (12).

Nevertheless, due to the delta function setting the momenta of the incoming and outgoing particle equal, the phase space integration of the loop momentum decouples from the phase space of the real external particles. In the previous chapter, we examined the peak structure of the integrand in the integration volume of the loop momentum. In applications of the Tree Theorem we will use this analysis to construct appropriate channels for the loop momentum. These will be merged with the phase space parameterization of the underlying Born graph.

In the next chapter, we will apply the Feynman Tree Theorem to the one loop QED corrections to Bhabha scattering. Here, we will also compare different approaches to an efficient phase space integration of the loop momentum, which the knowledge of the peak structure of the integrand makes possible.

5. Bhabha Scattering

In this chapter we will as a first application evaluate the massive QED one loop cross section of Bhabha scattering. This $e^+e^- \to e^+e^-$ scattering process is of great importance in electron-positron colliders like the upcoming ILC for the precise measurement of the luminosity at the interaction point. For small angles, this process is dominated by the kinematic singularity of the photon exchanged in the t-channel. The differential cross section in this limit is

$$\frac{d\sigma}{d\Omega} \propto \theta^{-4}, \tag{5.1}$$

and therefore gives a high event rate and allows for a precise determination of the luminosity. For the ILC, also large angle Bhabha scattering is of interest, since here the acollinearity of the scattered particles can be used to study beam-beam interactions, which result in a spread of the center of mass energy [68]. The experimental accuracy aimed for the luminosity measurement is below 1‰, cf. [69]. To match this experimental precision, theoretical predictions of the Bhabha scattering cross section should have at least the same accuracy. Therefore, higher order corrections have to be included in the calculations and implemented in the Monte Carlo event generators. The QED $\mathcal{O}(\alpha)$ corrections were calculated long ago [70–72], followed by the one loop electroweak corrections [73]. At $\mathcal{O}(\alpha^2)$ in QED, the virtual massive two loop corrections are still not known completely. To get an overview of Bhabha scattering and the present status of NNLO calculations, cf. [74–76] and references therein. A recent calculation of the photonic one loop corrections in terms of master integrals can be found in [77].

The Bhabha scattering process is ideally suited to test the evaluation of loops by the Feynman Tree Theorem. For the QED one loop corrections there are ten graphs, which we can also evaluate by FeynArts to compare our results with an established technique. We can check the cancellation of ultraviolet and infrared divergences by the subtraction diagrams from the BPHZ mechanism and real emission diagrams. Threshold singularities will be canceled by additional fix functions. The final integrands will still have a rich structure due to collinear peaks. In the following, we will reduce this structure by suitably folding the integrand and mapping of the integration measure. At the end of this chapter we also show the application of a multi channel integration routine, for which the integrands do not need to be manipulated in this way. We will calculate with a finite fermion mass. The occurrence of different scales for the electron mass $\mathcal{O}(1\,\mathrm{MeV})$ and the center of mass energy $\mathcal{O}(100\,\mathrm{GeV})$ will then pose a further challenge to the integration algorithm.

Since we do not take off-shell external particles into account and the one loop corrections will at most include four-point functions, we do not face overlapping threshold peaks in the integration volume, as argued in section 3.2.2. We demonstrate the construction of fix functions in this case in appendix C.

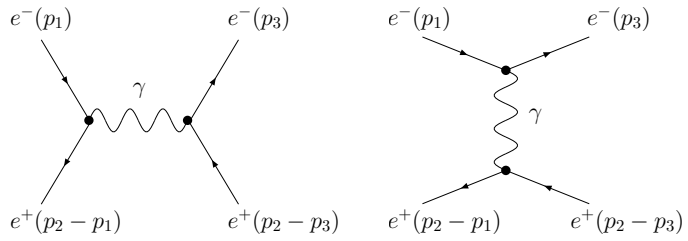

Figure 5.1: QED Born level graphs for Bhabha scattering.

5.1. Born Level

In QED, the Born process is given by the photon exchange in the s- and t-channel. The two graphs are depicted in figure 5.1. We assign the momenta as

$$e^-(p_1) + e^+(p_2 - p_1) \to e^-(p_3) + e^+(p_2 - p_3), \tag{5.2}$$

with

$$p_1 = \begin{pmatrix} \frac{1}{2}\sqrt{s} \\ 0 \\ 0 \\ \mathbf{p} \end{pmatrix}, \quad p_2 = \begin{pmatrix} \sqrt{s} \\ 0 \\ 0 \\ 0 \end{pmatrix}, \quad p_3 = \begin{pmatrix} \frac{1}{2}\sqrt{s} \\ \mathbf{p}\sin\theta \\ 0 \\ \mathbf{p}\cos\theta \end{pmatrix}. \tag{5.3}$$

The absolute momentum $\mathbf{p}$ and the scattering angle between the outgoing electron and the incoming electron, can be expressed in terms of the Mandelstam variables:

$$\mathbf{p} = \sqrt{\frac{s}{4} - m_e^2}, \quad \theta = \arccos\frac{s + 2t - 4m_e^2}{s - 4m_e^2}. \tag{5.4}$$

Thus, we get

$$p_2^2 = s > 4m_e^2, \quad -(s - 4m_e^2) < (p_1 - p_3)^2 = t < 0, \tag{5.5}$$

and further scalar products are:

$$p_1^2 = p_3^2 = m_e^2, \quad p_2^2 = s, \quad p_1 p_2 = p_2 p_3 = \frac{s}{2}, \quad p_1 p_3 = m_e^2 - \frac{t}{2}. \tag{5.6}$$

The unpolarized tree level amplitude is:

$$\begin{aligned} \mathcal{M}^{\text{Born}} &= \mathcal{M}_s^{\text{Born}} + \mathcal{M}_t^{\text{Born}} && (5.7) \\ &= -\frac{e^2}{s}\bar{v}(p_2 - p_1)\gamma_\mu u(p_1)\bar{u}(p_3)\gamma^\mu v(p_2 - p_3) && (5.8) \\ &\quad -\frac{e^2}{t}\bar{u}(p_3)\gamma^\mu u(p_1)\bar{v}(p_2 - p_1)\gamma_\mu v(p_2 - p_3). && (5.9) \end{aligned}$$

After summing over final state spins and averaging over initial spins, the squared amplitude reads

$$|\mathcal{M}^{\text{Born}}|^2 = 4e^2 \left\{ \frac{1}{s^2}\left[(t-2m_e^2)^2 + st + \frac{s^2}{2}\right] + \frac{1}{t^2}\left[(s-2m_e^2)^2 + st + \frac{t^2}{2}\right] + \frac{1}{st}\left[(s+t)^2 - 4m_e^2\right]\right\}, \tag{5.10}$$

where we kept the dependence on the electron mass m_e. In the case of two final particles, the phase space integral (2.54) simplifies to:

$$d\Pi_2(P, p_3, p_2 - p_3) = \int d\Omega \cdot \frac{\mathbf{p}}{16\pi^2\sqrt{s}}. \tag{5.11}$$

Together with the flux factor, this yields for the differential cross section for equal masses:

$$\frac{d\sigma^{(0)}}{d\Omega} = \frac{|\mathcal{M}^{\text{Born}}|^2}{64\pi^2 s} = \frac{\alpha^2}{s}\left\{ \cdots \right\}, \tag{5.12}$$

with the terms in the brackets taken from (5.10).

5.2. One Loop QED Corrections

To create a Fortran code providing the matrix elements of Bhabha scattering at $\mathcal{O}(\alpha)$ in QED, we used the procedure described below. The loop diagrams and the corresponding subtraction and real emission graphs will be created. The loops will be opened according to the Feynman Tree Theorem and the integrands further manipulated, such that even a single channel adaptive algorithm can be used for an efficient integration.

We wrote a Mathematica program which automatically calculates the integrands of the squared unpolarized QED one loop matrix elements in terms of scalar products. For each loop diagram also the corresponding real emission diagrams are created and their product calculated. This program makes use of the Mathematica- and FORM-based packages FeynArts and FormCalc [15, 16]. These allow for an automated creation of Feynman diagrams and the reduction of tensor integrals in various models. We inserted an additional flag in FormCalc.m and CalcFeynAmp.frm such that the call of CalcFeynAmp returns the amplitudes in terms of scalar products and the tensor reduction is not executed.

The resulting expressions for the loop diagrams are then further manipulated by a second Mathematica program. Here, a suitable integration momentum is determined. The direction of the loop momentum is chosen such that, if possible, the collinear peaks arise only from photon cuts and not fermion cuts. As discussed at the end of section 3.3.3, after addition of the real emission graphs, this would lead to a residual peak structure around the infrared singularity coming from the fermion cut. The center of the momentum of integration is chosen to be a point with high symmetry, which for example can be the point of an infrared divergence or the center of a threshold singularity. This will be explained

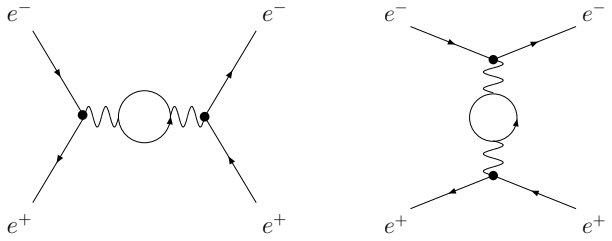

Figure 5.2: Vacuum Polarization Diagrams.

in more detail when the different loop contributions are discussed.

After assigning the integration momentum, the momentum distribution of the real emission graphs is accordingly matched and the subtraction graphs are created in the case of vertex corrections. The loops are cut and, if needed, fix functions are calculated and added to the resulting terms. Then, the integrand is folded such that collinear peaks and infrared divergent points fall on top of each other. The resulting expressions are then written out in Fortran code.

The above procedure is not fully automated yet. Simplifications of algebraic expressions are desirable. We have not found a satisfactory method of simplification which on the one hand acts on all the different expressions for the loop graphs and returns simple expressions on the other hand. Furthermore, the folding of the integrand is highly dependent on the peak structure and was mainly done by hand for the different loops. In light of an automated creation and evaluation of NLO matrix elements, it will therefore be more convenient to hand over the information about the peak structure of the integrands to the integration algorithm and use a versatile multi channel adaptive routine to evaluate the integrands instead of a manipulation of the code such that a single channel routine can be used. In the end of this section, we present the evaluation of a box graph with an unmodified peak structure by the integration routine VAMP. For this, we also present the evaluation of a single polarized amplitude.

5.2.1. Photon Self-Energy

The two contributions from the vacuum polarization are shown in figure 5.2. In the standard model, the loops may contain any electrically charged particle. The photon self-energy therefore gets contributions from leptons, charged bosons and ghosts, and hadrons. In the hadronic part strong interaction effects may play an important role, which can be included in calculations via a dispersion integral over the hadrons-to-muons production rate R, e.g. cf. [78]. Since we are only interested in the applicability of the Feynman Tree Theorem to loop integral evaluations, we restrict ourselves to the pure electron loop, although some QED evaluations include all nine fermion flavors summed over in perturbation theory, see [77]. We state the final integrands we used in appendix B. This also involves a constant part which is not integrated over. We included this part

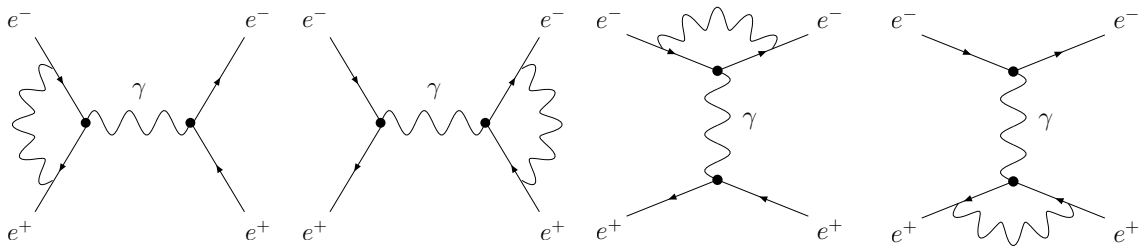

Figure 5.3: Vertex Corrections: Subtraction graphs have to be added to cancel the ultraviolet divergence and retain the definition of the electric charge.

by dividing it by the integration volume and add it to the integrand. This integrand does not have a particularly difficult peak structure. It is also infrared finite, so we did not apply any further cuts or mappings to it except the fix function to smooth the peak in the s-channel.

5.2.2. Vertex Corrections

The four vertex corrections are depicted in figure 5.3. The integrands each contain one infrared point, where the momentum through the photon line vanishes. We chose this point as the origin of a spherical coordinate system we integrate over. As discussed in section 3.3.3, we expect collinear peaks starting at this point.

In the case of the t-channel vertex corrections, we have the possibility to chose the direction of the loop momentum such that the collinear peaks arise from the photon cuts. This is the case if in each fermionic propagator the loop momentum is opposite to the direction of the momentum of the adjacent external particle, cf. table 3.1. Taking as an example the corrections to the electron vertex, the collinear peaks are then situated on a line from the origin to $\vec{p}_1$ and $\vec{p}_3$, respectively. In the limit $t \to 0$ the two peaks merge. To fold the integrand such that the collinear peaks fall on top of each other, we set the k_z-axis along the bisecting line of the two peaks such that the peaks are located in the $k_x - k_z$ plane. We then added the integrands $I(k_x, k_y, k_z)$ and $I(-k_x, k_y, k_z)$ and cut out one half of the resulting expression by setting the integrand for $k_x < 0$ to zero. A new coordinate system was then obtained by rotating the k_z-axis such that it is aligned with the remaining collinear peak. In this way the original integrand was mapped such that only one collinear peak remained. An adaptive integration method can therefore efficiently give reliable results.

In the case of the s-channel corrections, the collinear peaks fall on top of each other, since we calculate the matrix elements in the center of mass frame of the two incoming and outgoing particles. The resulting peak starts at $\vec{k} = 0$ and extends to $\vec{k} = \pm\vec{p}_1$, or $\vec{k} = \pm\vec{p}_3$ for the second correction, respectively. The sign depends on the direction of the loop momentum. Since effectively only one peak is present, we do not have to apply any mapping procedures to the integrand. We only take the k_z-axis of the integration

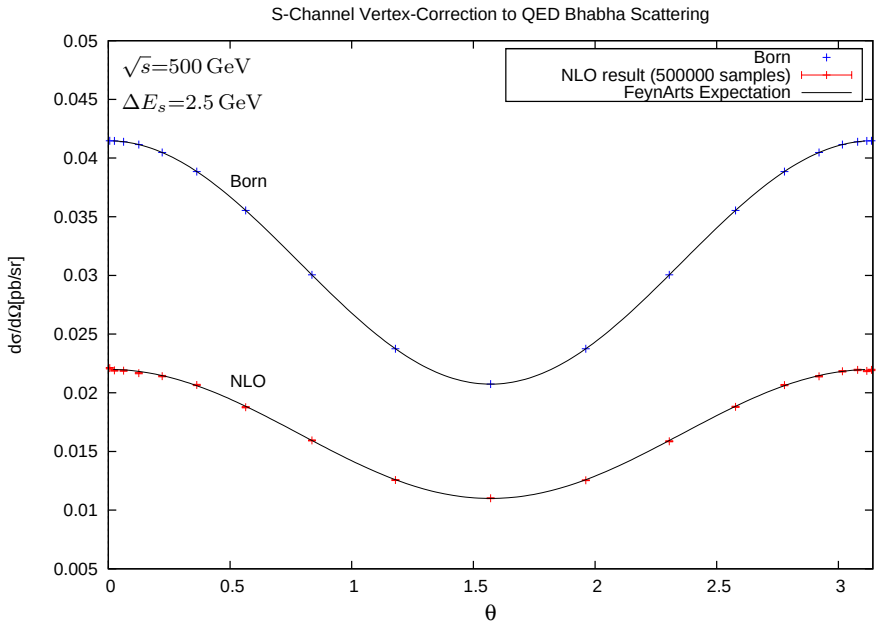

Figure 5.4: One loop vertex correction to s-channel. Lines are obtained from FeynArts. Points are results from the Feynman Tree Theorem, numerically evaluated using Vegas.

momentum along the collinear peak. However, a threshold singularity arises if one of the two fermionic propagators is cut and we added a fix function to smooth this peak.

The integrands of the subtraction graphs were calculated by first neglecting all denominators of non-loop propagators and then aligning the momenta of the two fermion lines of the vertices as was described in section 3.3.2. In case of the s-channel corrections this was done by flipping the line of one incoming (outgoing) fermion to an outgoing (incoming) antifermion. Explicitly, the relevant Dirac chain of the second s-channel vertex correction in figure 5.3 reads:

$$\bar{u}(p_3)\gamma_\alpha(\not{k}+\not{p}_3+m)\gamma_\mu(\not{k}+\not{p}_3-\not{p}_2+m)\gamma^\alpha v(p_2-p_3). \tag{5.13}$$

Aligning the fermion momenta means either replacing p_2-p_3 with $-p_3$ or vice versa. We then have the crossing symmetry relations:

$$\bar{u}(-p_2+p_3)\to\bar{v}(p_2-p_3), \quad \text{or} \quad v(-p_3)\to u(p_3). \tag{5.14}$$

Note that our Mathematica program using FeynArts and FormCalc only returned squared amplitudes. Thus, to calculate the subtraction graphs, we replaced the relevant momenta in the whole expression of our vertex corrections. After that, we divided by the corresponding product of Born amplitudes with the same replacements of momenta and neglection of denominators of propagators and multiplied by the original Born amplitude without replacements. As a verification of this approach, we calculated the s-channel

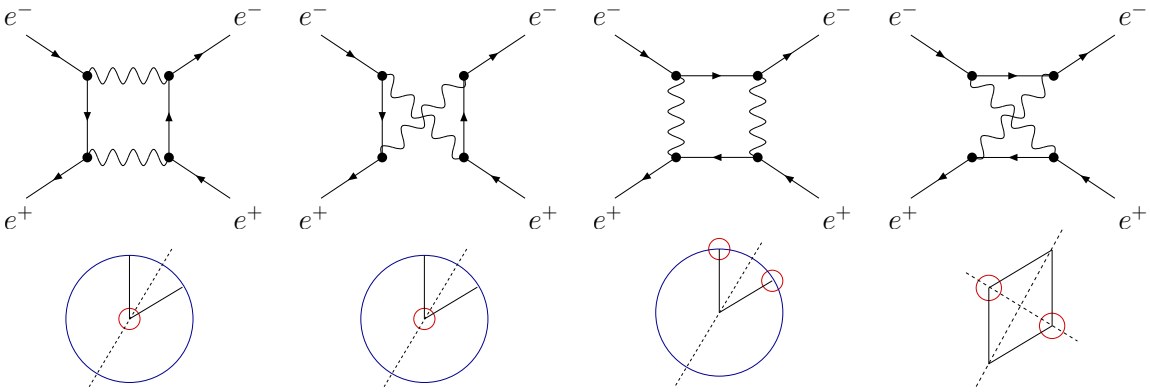

Figure 5.5: Box Graphs and sketch of corresponding peak structure in the $x - z$ plane. Small (red) circles indicate infrared points. Lines collinear peaks. Big (blue) circles threshold singularities. The dashed lines indicate the planes at which the integrands are mirrored such that infrared singular points and collinear peaks fall on top of each other. The resulting expressions can then be evaluated by a single channel adaptive integration routine.

vertex correction at a rather high precision of 500000 samples for each point. The results, together with the Born cross section, is shown in figure 5.4. We used a center of mass energy of $\sqrt{s} = 500\,\text{GeV}$ and a soft energy cutoff $\Delta E_s = 2.5\,\text{GeV}$ and compared our results with those obtained from FeynArts.

5.2.3. Box Graphs

The box graph contributions are depicted in figure 5.5. These are ultraviolet finite and no subtraction graphs have to be added. Since there are two photon lines we have two infrared peaks in the integration volume. These might fall on top of each other. According to the analysis in section 3.3.3, we can also have up to four different collinear peaks. We schematically sketched the peak structure of each of the box graphs in figure 5.5. Here, the small circles indicate infrared singular points, which are the endpoints of collinear peaks indicated by lines. Threshold singularities are pictured by big circles. Like in the case of the vertex corrections, we fold the integrands according to the peak structure such that infrared points and collinear peaks fall on top of each other and the final integrand consists only of one peak each. The planes at which the integrands are mirrored are indicated as dashed lines. After folding the integrands, the origin of the coordinate system of the integration momentum is taken to be the remaining infrared point and the k_z-axis is aligned to the collinear peak. Fix functions are added if needed.

5.3. Integration Parameters and Results

Having prepared the integrand in the way described above, we can use an adaptive integration routine for its evaluation. For this, we used the single channel routine of the VAMP package, which essentially is the Vegas algorithm. At the end of this chapter, we present

the evaluation of a box graph using a multi channel approach, cf. section 4.1.4.

5.3.1. Coordinate System and additional Mappings

We use a coordinate system with the z-axis aligned with the remaining collinear peak, as described above. The y-axis is not changed and the x-axis is orthogonal to the y- and z-axis. Applying spherical coordinates, we map the radial coordinate r onto the unit interval by

$$r = a\left(\frac{1}{1-x_1} - 1\right), \tag{5.15}$$

with a set to $\frac{1}{2}\sqrt{s}$. Using x_1 as new integration variable, this choice will map the region of the threshold singularities into the center of the unit interval. This will enhance the grid adaption, since the interesting region with the remaining peak structure is spread over a significant part of the integration interval.

To further increase the efficiency of the grid adaption, we change the coordinate of the polar angle according to the analysis in section 4.2. The almost singular part of the collinear propagators encountered in the graphs for Bhabha scattering is:

$$P_{coll} = \left(\frac{\sqrt{s}}{\sqrt{s-4m_e^2}} - \cos\theta_{\text{Int}}\right)^{-1}. \tag{5.16}$$

Using equation (4.31), we change to the new coordinate x_2 by replacing:

$$\theta_{\text{Int}} = \arccos\left(\frac{\sqrt{s}}{\sqrt{s-4m_e^2}} - \left(1 + \frac{\sqrt{s}}{\sqrt{s-4m_e^2}}\right)\left(\frac{\sqrt{s}-\sqrt{s-4m_e^2}}{\sqrt{s}+\sqrt{s-4m_e^2}}\right)^{x_2}\right). \tag{5.17}$$

The arising Jacobian determinant will then cancel the singular part (5.16) such that the integrand is considerably smoothed even before the grid adaption.

Making a further replacement of the azimuthal coordinate

$$\phi = 2\pi x_3, \tag{5.18}$$

we have a new set of integration variables in the unit hypercube

$$(x_1, x_2, x_3) \in [0,1]^3. \tag{5.19}$$

5.3.2. Input Parameters

We evaluated all of the following results at a center of mass energy of $\sqrt{s} = 500\,\text{GeV}$. This lies in the typical energy region of the ILC. Although results of Bhabha scattering have to incorporate the Z-boson exchange and electroweak corrections to give accurate predictions, we nevertheless use this process and the stated energy to test the applicability of loop evaluations via the Feynman Tree Theorem to realistic scenarios with a large

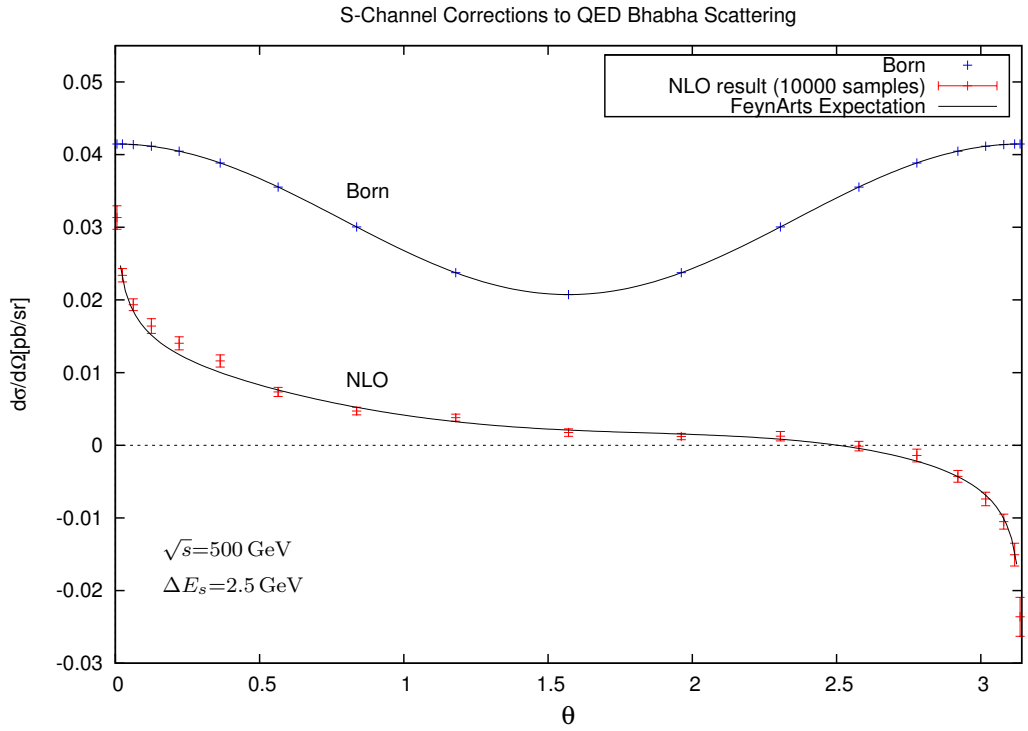

Figure 5.6: Differential cross section of $O(\alpha)$-correction to s-channel Bhabha scattering. Here, the cross section becomes negative for large back-scattering angles.

difference in scales of the fermion masses and the kinematic variables.

The infrared cutoff ΔE_s is set around 1% of the center of mass energy as is the width of the fix functions added to smooth threshold peaks. To take the contributions of the real emission graphs into account, we set the integrand of the corresponding photon cut to zero for soft photons with energy below ΔE_s. As argued in section 3.3.3, we similarly cut out contributions from fermion cuts in the cases where it was unavoidable that a peak at the infrared singular point is developed.

5.3.3. Results

In the following we present results for the differential and total cross section of NLO Bhabha scattering. The final integration was done with the single channel integration routine of VAMP. Results were cross checked with FeynArts.

S-Channel Contribution

In figure 5.6, we separately plotted the differential cross section of the s-channel corrections. Here, we used a rather small number of 10000 samples for each point. Even with this small amount of samples, the differential cross section is close to the result obtained by FeynArts. This and a rather small error estimate indicate that the initial integrand

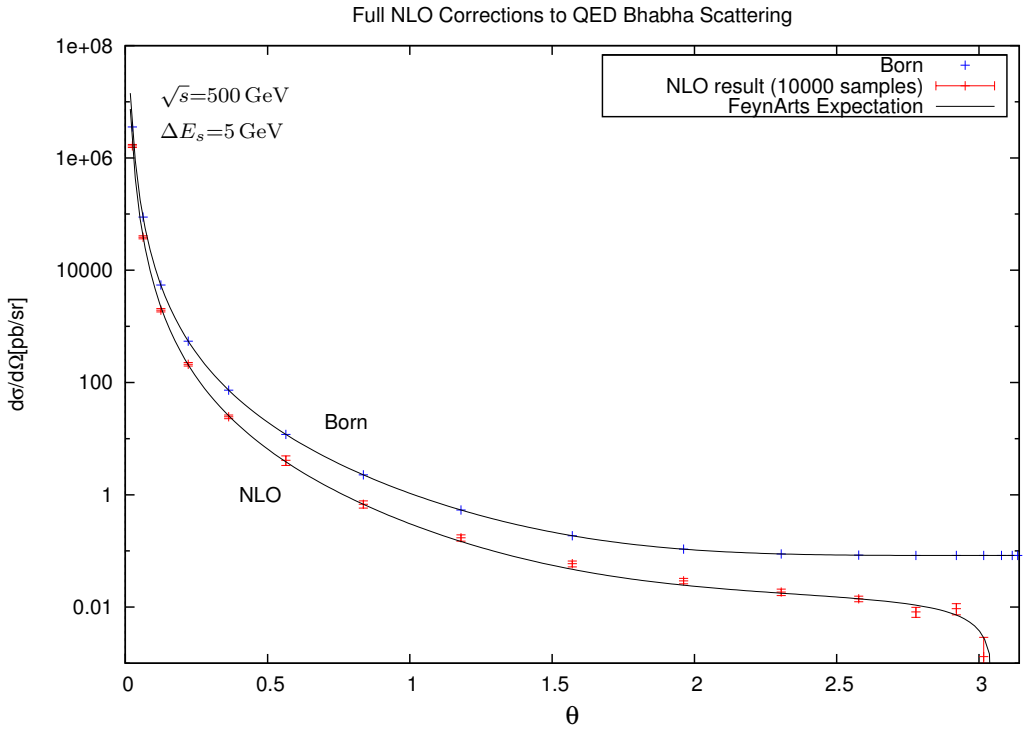

Figure 5.7: Complete $\mathcal{O}(\alpha)$-correction to QED Bhabha scattering.

is sufficiently smooth and the integration grid can quickly adapt to it.

We used a small value for the soft photon cutoff $\Delta E_s = 2.5\,\text{GeV}$. This cutoff acts as a regulator for the infrared divergence. Adding the hard real emission contributions at the same order in perturbation theory, the full NLO result is not dependent on this cutoff [35]. However, the single $2 \to 2$ cross section depends on the cutoff which can lead to the unphysical situation of a negative probability distribution. If experimental quantities are sensitive to such low photon energies, one has to take further higher order contributions into account [78].

All virtual $\mathcal{O}(\alpha)$ Contributions to QED Bhabha Scattering

In figure 5.7, we plotted the full 1-loop QED contribution to Bhabha scattering. We again used a very small number of 10000 samples to demonstrate the rather fast convergence to the expected results. Almost throughout the whole region of the scattering angle θ, the differential cross section is dominated by the t-channel exchange and corrections to it. This time we used a soft energy cutoff of $\Delta E_s = 5\,\text{GeV}$. Nevertheless, in the very backwards region the cross section again drops below zero.

In figure 5.8, we plotted the ratio of the 1-loop corrections to the Born result, this time using a rather high precision with $5 \cdot 10^6$ calls for each sampled point. The agreement

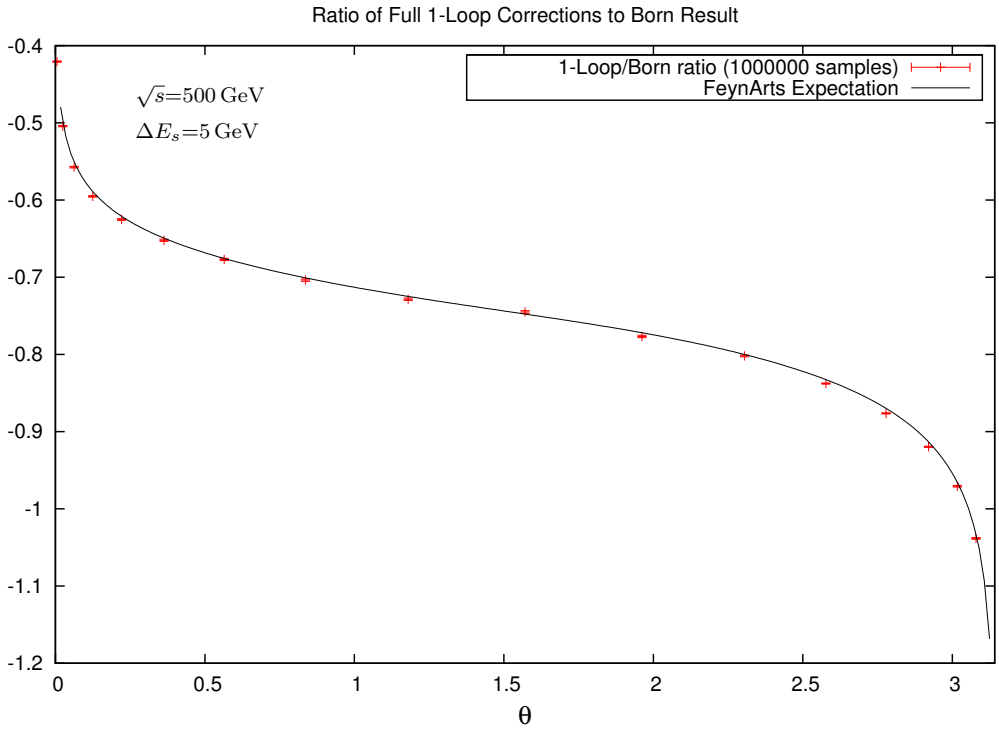

Figure 5.8: Ratio of $\mathcal{O}(\alpha)$-correction to Born contribution.

between the two calculations is at the per mil level. Since these are deviations from the $\mathcal{O}(\alpha)$ corrections, this is a very satisfactory result. Since the treatment of infrared divergences differs to that used in FeynArts, we do not expect the results to coincide completely. Instead of using it for cross section integration, we are more interested in applying this method to event generation, which requires a rather smooth integrand. The previous results showed that the expectation value is approximated quite well after a few calls, indicating a good adaption of the grid to the integrand.

Total Cross Section

To obtain results for total cross sections, we applied a further mapping of the scattering angle to a new integration variable, by replacing:

$$\theta = 2 \arcsin \frac{1}{\sqrt{\frac{1-x_4}{\sin^2\frac{\theta_l}{2}} + \frac{x_4}{\sin^2\frac{\theta_h}{2}}}}, \tag{5.20}$$

where $\theta_{l,h}$ are the lower and upper cut on the scattering angle. For the numerical evaluations we set those to 1 deg. Making this replacement, the resulting Jacobian cancels the factors of t in the denominator and therefore smooths the peak considerably. The numerical results are shown in figure 5.9 and again compared with results from FeynArts.

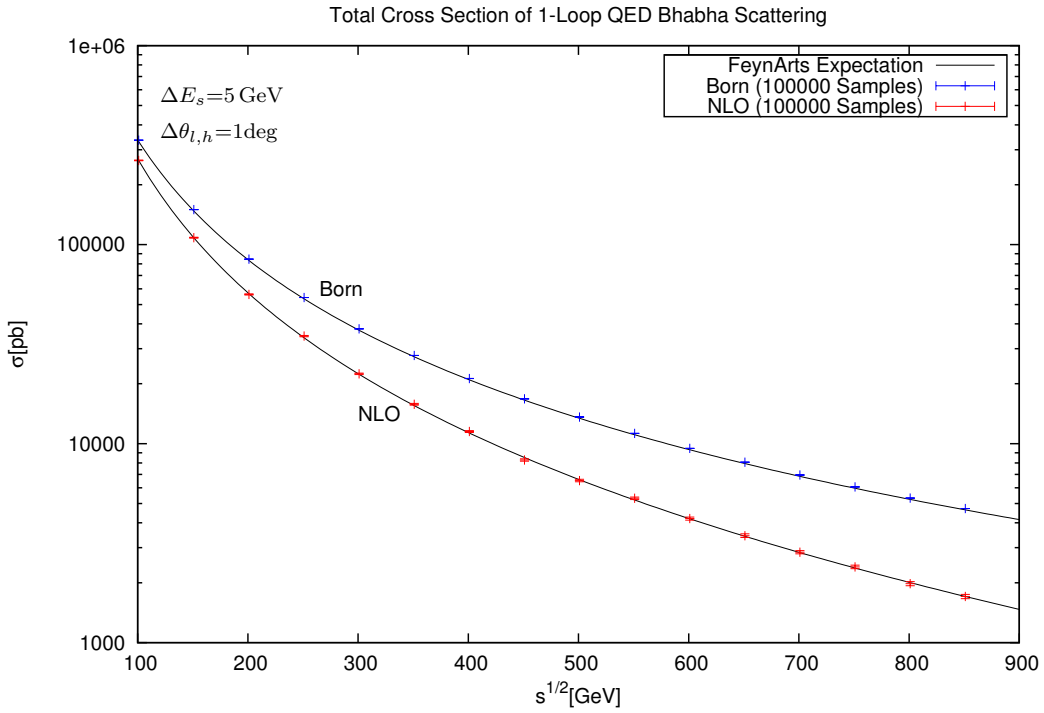

Figure 5.9: Integrated Cross Section of $\mathcal{O}(\alpha)$-corrections to QED Bhabha Scattering.

Alternative Evaluations

To go a step further towards an automated generation of matrix elements and subsequent numerical evaluation, we tested the applicability of the multi channel integration routine VAMP to our method of loop evaluation. We examined the contribution of the first box depicted in figure 5.5 to the s-channel photon exchange. In a first approach, we used the code produced by the Mathematica programs without applying any mappings, such that the two collinear peaks remain in the integrand. We used two channels with a spherical coordinate system, with the z-axis aligned to one of the peaks, respectively. The result is shown in the upper plot of figure 5.10.

In a second approach, we used the matrix element generator O'MEGA, to produce the box graph as a helicity amplitude. For this, we created the four associated tree graphs which would be obtained by opening the loop of the box at each of its propagators:

$$e^-(p_1)e^+(p_2-p_1) \to e^-(p_3)e^+(p_2-p_3)e^+(k'_{1,2})e^-(-k'_{1,2}), \tag{5.21}$$
$$e^-(p_1)e^+(p_2-p_1) \to e^-(p_3)e^+(p_2-p_3)\gamma(k'_{3,4})\gamma(-k'_{3,4}). \tag{5.22}$$

Here, we assigned the momenta k_i such that they correspond to the momentum of the associated loop propagator. We again used the same two channels as in the first application of the multi channel routine. By using this approach, the one loop and Born amplitudes

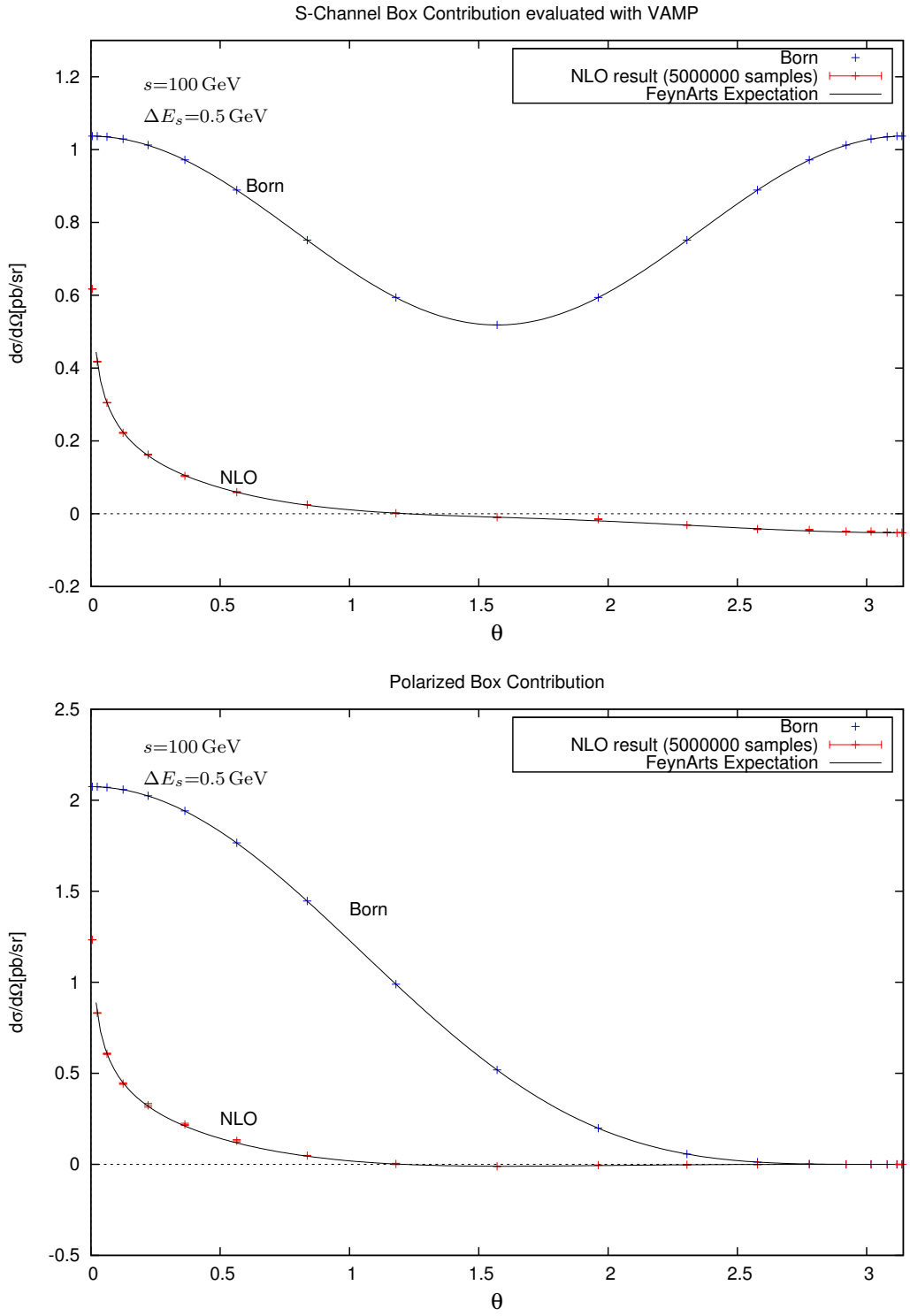

Figure 5.10: Box graph evaluated with the multi channel routine VAMP. Upper Plot: Result from Mathematica for unpolarized contribution. Lower plot: Polarized box graph created with O'MEGA.

are evaluated separately and the product is taken afterwards. In particular, this means we can compute single polarized amplitudes, which in the case of processes with several Born amplitudes increases the efficiency compared to the evaluation of products of amplitudes because of the smaller number of terms. In the lower plot of figure 5.10, we showed the box contribution to the $e_L^- e_R^+ \to e_L^- e_R^+$ scattering amplitude. The results are in agreement with the FeynArts predictions.

6. Monte Carlo Event Generation

Monte Carlo event generators serve as an interface between theory and experiment. They combine theoretical knowledge of different fields of particle physics to simulate events in high energy collision processes as close to nature as possible. These simulations are needed to understand the complicated multi particle structure of scattering events, to efficiently design detector components and to compare experimental data with predictions from theory. The center of such generators is the hard partonic sub-process. It is described by a matrix element accounting for all quantum field theoretical effects. Integration techniques similar to those introduced in chapter 4 are used to generate events, samples of partonic final states with the same probability as expected from real collision events. The initial states of an event can also be convoluted with structure functions describing initial state radiation and parton distribution functions. All initial and final state partons can be evolved to lower energies by parton shower algorithms. Finally, phenomenological models of hadronization of the partons can be applied as well as subsequent decays of short lived hadrons. Ideally, a general purpose Monte Carlo event generator package should contain all these different building blocks to simulate full events of a collision process. An introduction to the different methods used in the simulations and an overview of some packages implementing these techniques can be found in [79].

To get a higher predictivity of the simulated events, it is mandatory to go from the tree level matrix elements to one loop. There exist packages which implement some processes at next to leading order precision, however, a fully automatized general purpose Monte Carlo at NLO has not been developed yet. In this chapter we will give a brief overview of the techniques of event generation and discuss problems to be expected when using matrix elements at NLO. We will finally present event samples for pure QED Bhabha scattering generated with the code introduced in chapter 5 based on the Feynman Tree Theorem.

6.1. Cross Section Integration and Event Generation

In the previous chapter we used the Monte Carlo integration technique to calculate differential and total cross sections. This was done by sampling the phase space with a uniform distribution or a distribution of the integration variables close to the peak structure of the integrands. In the following we define the weight w_i of a uniformly sampled point in phase space x_i as the value of the integrand containing the original function and all Jacobians from transformations as well as grid adaptations. Thus, adding up these weights w_i of each sampled point and dividing by the number of calls the expectation value of the integral is obtained:

$$\langle I \rangle = \frac{1}{N} \sum_i w_i. \tag{6.1}$$

One sampled point of the phase space is called an event. The event weights obtained in the above procedure can be used to fill histograms. In the limit of a large number of events, the resulting histograms converge to the physical distribution of the considered process.

However, a single event has no physical meaning, since it originates from a uniform distribution of sampled phase space points.

The main virtue of Monte Carlos in particle physics is the simulation of collision processes. Here, contrary to the method described above, events are generated with a distribution predicted by theory. All of the events will have the same uniform weight, however the frequency is given by the probability of the events to occur. Thus, a set of events generated by a Monte Carlo reflects the set of real events to be expected in the collision process under consideration.

6.1.1. Unweighted Event Generation

The procedure of generating events according to a physical distribution is called *unweighting* of events. The mainly used technique is the acceptance-rejection method. Starting again from a uniform distributed sampling of phase space, each event's weight is divided by the maximal weight $w_{\max}$. This ratio is compared with a uniformly chosen random number $r \in [0, 1]$ and the event is accepted if

$$r \leq \frac{w_i}{w_{\max}}. \tag{6.2}$$

Otherwise, the event is rejected and a new phase space sample is chosen. The accepted events are then distributed according to the probability given by the matrix element and have a uniform weight. For this procedure the maximal weight of the integrand has to be known. For simple processes this can be inferred from the kinematics. However, for more complicated functions and adaptive integration algorithms a scan over the parameter space is the usual way to approximate the maximal weight.

For tree level matrix elements this procedure is automatized in several Monte Carlo event generators [31, 80–82]. First, the matrix element of the hard partonic sub-process is created. Here, the incoming particles can be dressed with initial state radiation and parton distribution functions in the case of interacting quarks or gluons. Then an integration over the whole parameter space is performed to obtain the total cross section. In `WHIZARD` this is done by the multi channel routine `VAMP` described in chapter 4. In several iterations the grid is adapted to the integrand and a set of integrations with a higher number of calls returns the desired cross section. Here, it is trivial to keep the highest weight encountered in the sampling procedure. Using this approximated maximal weight and the total cross section one can generate unweighted events with a physical distribution and quantity according to a given luminosity. These events can then be further processed with parton shower and hadronization algorithms to mimic a full event in a collision.

6.2. Event Generation at NLO

Several problems arise when extending calculations from tree to loop level. Obvious problems are the drastic increasing number of Feynman diagrams contributing to a given process, which even worsens in the case of hadron collisions, where a given set of final

states can be the outcome of several different partonic initial states. A gain in accuracy is therefore related to an increase in computer time, which in some cases tips the scales towards the simpler tree level calculations. Furthermore, the peak structure of the integrands gets more complicated and methods for efficient numerical evaluation have to be developed, like those shown in chapter 4.

More subtle problems of NLO calculations are emerging negative weights and the technically difficult matching of the fixed order matrix element calculations with resummed expressions taking enhanced higher order contributions into account.

6.2.1. Negative Weights

We have seen in chapter 5 that the differential cross section of the $2 \to 2$ NLO contribution can become negative in certain regions of the phase space. This is an artefact of the fixed order method. The full $\mathcal{O}(\alpha)$-result involves the $2 \to 2$ virtual correction, the real emission of a soft photon and a hard photon[1]:

$$\sigma_{\text{tot}} = \sigma_{\text{Born}} + \sigma_{\text{virt.}}(\Delta E_s) + \sigma_{\text{soft}}(\Delta E_s) + \sigma_{\text{hard}}(\Delta E_s). \tag{6.3}$$

The energy cut ΔE_s serves as a regulator of the infrared divergences appearing separately in the $2 \to 2$ and $2 \to 3$ part. It is reasonable to assume for the ILC a detector sensitivity of $\Delta E_s \approx 10^{-4} \ldots 10^{-3}\sqrt{s}$, furthermore our approximation of the soft photon part violates momentum conservation and therefore neglects terms of $\mathcal{O}(|\vec{k}|)$ in the photon momentum and a small value of ΔE_s is preferable. Using ΔE_s as a regulator the $2 \to 2$ and $2 \to 3$ parts are enhanced by a factor proportional to $\log \frac{\Delta E_s}{\sqrt{s}}$, which eventually can lead to negative differential cross sections. Generating events with a negative weight in these regions of phase space is not physical in the sense that nature produces events only with a positive probability. Here, a negative event weight has the same physical meaning as a negative differential cross section - none.

Matching

A possibility to lift the cross section again above zero, is to combine the $2 \to 2$ calculation with parton showers or initial state radiation [10, 83–85]. Here the logarithmically enhanced parts of a collision process, the soft and collinear real and virtual radiation, can be approximated to all orders in perturbation theory and summed up in a structure function convoluted with the matrix element. Since real and virtual contributions are taken into account this is an infrared safe procedure. Including these functions in the simulation one has to subtract from the structure functions the parts which are already included in the explicit matrix element calculations of the hard partonic sub-process. Matching these two parts as well as the $2 \to 3$ real emission part such that no contribution is counted twice

[1] Here, the hard photon cross section can further be divided in a collinear and a non-collinear part by a cutting parameter θ_c. The collinear part can then be approximated by an analytic structure function convoluted with the Born matrix element. Since we did not make this distinction in the virtual part and left the evaluation to the numerical integration algorithm, we also do not introduce a cut on the angle in real emissions.

anywhere in phase space is a highly non trivial task and a very active field of research. We will not dwell any deeper on this issue in this thesis, since we are mainly interested in the applicability of our method of calculating loop diagrams for event generation. Nevertheless, in [83,86] a resummation method was introduced for chargino production at the ILC within the event generator `WHIZARD` and an adaption of this method should be feasible at a later stage of our work.

6.3. Event Generation for Bhabha Scattering

Using the integrand obtained from the Feynman Tree Theorem, we will generate unweighted events on the level of the hard partonic sub-process, without further dressing of the initial and final state particles with parton shower algorithms.We will sample the phase space of the external particles at the same time as the phase space of the additional incoming and outgoing particles from the cutting procedure. Thus, we will set the loop momentum integration and the phase space integration of the external particles on equal footing without any preference for one of the two integrations. This differs from many other applications of event generation at NLO, where for a given set of external momenta the matrix element is fully evaluated which usually involves the numerical integration over several parameters in different terms of the integrand or the evaluation of polylogarithms. Even in the case of an analytic result of the loop corrections this can be a time consuming procedure, especially in the case of multi leg amplitudes.

Negative Weights - II

When generating events by sampling the full phase space, we will very likely encounter negative weights. These arise from regions of the phase space where the integrand is negative. Even for a well adapted grid and a resulting smooth integrand this might not always be avoidable. However, these negative weights differ form those mentioned above in the sense that for a sufficiently large sample the amount of events with a negative weight will be outnumbered by positive events with a similar configuration of the external momenta. This holds true except for the regions mentioned above where the differential cross section becomes negative by itself. We will therefore keep all generated events and assign a uniform weight to them which is either positive or negative. In resulting histograms we will subtract the number of negative events from the positive events in each bin.

Error Expectation

The momentum of the additional incoming and outgoing particle is a purely inclusive parameter. Thus, when a set of generated events is used to fill a histogram, each bin contains events with a non trivial distribution of the inner momentum. Although it does not increase the statistical error, taking the additional phase space of the loop momentum into the sampling procedure lowers the efficiency of event generation. This can be seen in the simplified model of figure 6.1. Suppose we want to generate unweighted events and fill two bins with the relative weight distribution of $2 : 3$, indicated in the first picture.

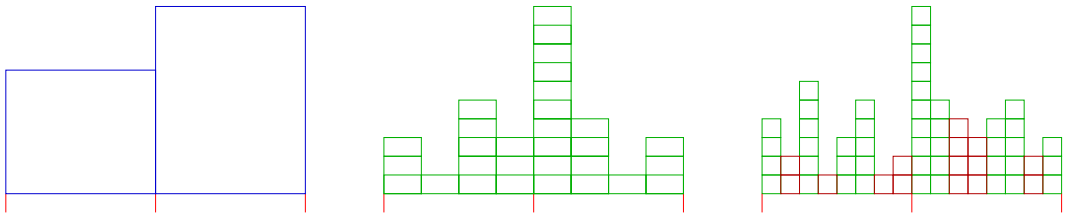

Figure 6.1: Simplified polynomial model to describe the origin of the statistical error when sampling over an inclusive parameter (second and third picture) and negative weights (red/dark gray) is included.

If we sample a point in the right bin, the corresponding event is always taken, since this bin contains the highest weight and therefore $p_2 = 1$. A candidate event in the first bin is accepted with probability $p_1 = \frac{2}{3}$. The overall efficiency is $\frac{1}{2}p_1 + \frac{1}{2}p_2 = \frac{5}{6}$. Sampling n_0 times, the expectation value and variance are given by

$$\langle n_i \rangle = n_0 p_i, \qquad v_i = n_0 p_i (1 - p_i), \tag{6.4}$$

being a polynomial distribution. In the second picture we sketched the situation of event generation with a non-constant integrand over an inclusive parameter with absent negative weights. The relative weight distribution of the two bins is still $2 : 3$. The probability of accepting an event in the first bin adds up to $p_1 = \frac{3}{20}$, in the second $p_2 = \frac{9}{40}$. The overall efficiency is therefore $\frac{3}{8}$, being lower than in the first case. The expectation values as well as the corresponding variances are still given by equation (6.4), which is a statistical property of the polynomial distribution. Thus, sampling over an additional inclusive parameter only lowers the efficiency of event generation, not the statistical error. The continuous case can be seen as limiting case of the polynomial distribution. Note also, that in the case of a large number of samplings n_0 and a typical number of bins, p_i is low enough to approximate the error estimation by the upper bound $\sqrt{\langle n_i \rangle}$.

The inclusion of negative weights does not necessarily lower the efficiency of event generation. However the error estimate rises. We accept an event with a negative weight, if its absolute value divided by the absolute maximal weight is higher than a randomly chosen number between zero and one. In the third picture of figure 6.1 we depicted negative weights as red (dark grey) columns. Here, we chose the distribution such that the efficiency of event generation is the same as in the second case. The probability of finding a positive/negative event in bin i is given by: $p_1^+ = \frac{18}{160}$, $p_1^- = \frac{6}{160}$, $p_2^+ = \frac{27}{160}$, $p_2^- = \frac{9}{160}$. The expectation value of the number of events in each bin and the corresponding variance are still given by equation 6.4, however the notion of p_i differs:

$$\langle n_i \rangle = n_0 (p_i^+ - p_i^-), \qquad v_i = n_0 (p_i^+ + p_i^-)(1 - (p_i^+ + p_i^-)). \tag{6.5}$$

Thus, in the given example we have to sample with twice n_0 to obtain the same number of events in each bin, which results in a variance twice as large as in the second case. Table

	n_0	bin 1	bin 2
I	12000	4000 ± 52	6000 ± 55
II	26667	4000 ± 58	6000 ± 68
III	53334	4000 ± 82	6000 ± 96

Table 6.1: Number of required samples to generate 10000 events and corresponding expectation values and errors for each of the situations depicted in figure 6.1. The inclusion of negative weights raises the amount of samples needed and increases the error.

6.1 summarizes by giving the number n_0 of needed samples to generate 10000 events and also stating expectation value and error of events in each bin.

6.3.1. Implementation

For the generation of unweighted events we used as integrand the code described in section 5.2. This was mainly created in a Mathematica environment and written out to FORTRAN. Since this code was created such that just one grid is needed to adapt to the peak structure of the integrand, we used a single channel adaptive routine. We made use of procedures for grid creation and adaption, event generation and filling of histograms already present in our version of VAMP. We extended these routines to the inclusion and bookkeeping of possible negative events. We accept an event w_i, if

$$r \leq \frac{|w_i|}{w_{\max}^{\pm}}, \tag{6.6}$$

with random number $r \in [0,1]$ and $w_{\max}^{\pm} = \max(|w_{\max}|, |w_{\min}|)$ being the maximal weight of the absolute value of the integrand encountered in the grid adaption and integration steps. If an event is accepted, it gets an additional flag $+1$ or -1, indicating whether its weight was positive or negative. Histograms are then filled according to the sign of the events.

Unweighted event generating was done by the following steps:

- Setting up a grid and allow for adaption in several iterations.
- Use grid to estimate total cross section with a high number of samples. Keep highest and lowest, possibly negative weight.
- Use grid to generate events with the acceptance/rejection method described above. Keep sign of weight.

For Bhabha scattering at NLO, we used the generated events to create histograms showing number of events as a function of the polar angle between the initial and final electron. We also generated events distributed according to the Born cross section. We used the total cross sections to compute the amount of generated events for a given luminosity.

6.3.2. Results

External Parameters

Although for a practical use of event generation for Bhabha scattering in terms of a precise measurement of luminosity, it is mandatory to include the full electroweak corrections and higher order real and virtual corrections as well as a resummation of enhanced higher order contributions, we nevertheless use the created code to simulate events with parameter settings taken for typical processes at the upcoming ILC [69, 87].

S-Channel Distribution

To demonstrate the handling of negative events, we generated events for electron-positron annihilation and the corresponding photonic corrections. We used a small infrared cutoff $\Delta E_s = 2.5\,\mathrm{GeV}$, which is 0.5% of the center of mass energy $\sqrt{s} = 500\,\mathrm{GeV}$. Here, the differential cross section is negative in parts of the phase space. Results for Born and NLO event generation are shown in figure 6.2. The total Born and NLO cross sections are obtained from Monte Carlo integration of the grids set up for event generation:

$$\sigma^{tot}_{\mathrm{Born}} = 0.34744(29)\mathrm{pb}; \qquad \sigma^{\mathrm{tot}}_{\mathrm{NLO}} = 0.03434(91)\mathrm{pb}. \tag{6.7}$$

Using only the Born level result, we generated 100000 unweighted events which corresponds to an integrated luminosity of about $\mathcal{L} = 290\mathrm{fb}^{-1}$. Since the Born result is strictly positive, we did not encounter any negative weights. Here, the efficiency of event acception is:

$$\mathrm{eff}_{\mathrm{Born}} = \frac{n^{\mathrm{evts.}}}{n^{\mathrm{calls}}} = 66\%, \tag{6.8}$$

where we adapted the grid in 6 iterations using 1000 samples each, discarded the integral and performed an integration with a total number of 15000 samples in three iterations. Since we used only few samples to set up the grid and extract the total cross section, it is quite natural that higher weights than the original maximal weight are encountered while sampling for event generation. Nevertheless, in this simple one dimensional integration, these weights are very close to the maximum and do not alter the overall result.

Comparing the NLO with the Born cross section, we want to generate 9887 unweighted events. If we allow for events with a negative weight, it follows that we have to generate events until the difference of positive and negative events equals 9887. Since in this case the integrand is rather equally distributed among positive and negative values, we had to generate a total amount of about 150000 events (78770 positive and 68883 negative). The effectivity for generating all events is

$$\mathrm{eff}^{\mathrm{p+n}}_{\mathrm{NLO}} = 1.8\%, \tag{6.9}$$

however, the efficiency of generating events which finally show up in the histogram after the negative events are subtracted from the positive ones in each bin, namely 11655 events, is at the per mil level: $\mathrm{eff}^{\mathrm{hist}}_{\mathrm{NLO}} = 0.14\%$. Clearly, this is a rather extreme case where the differential cross section is small and even negative in some regions of the phase space.

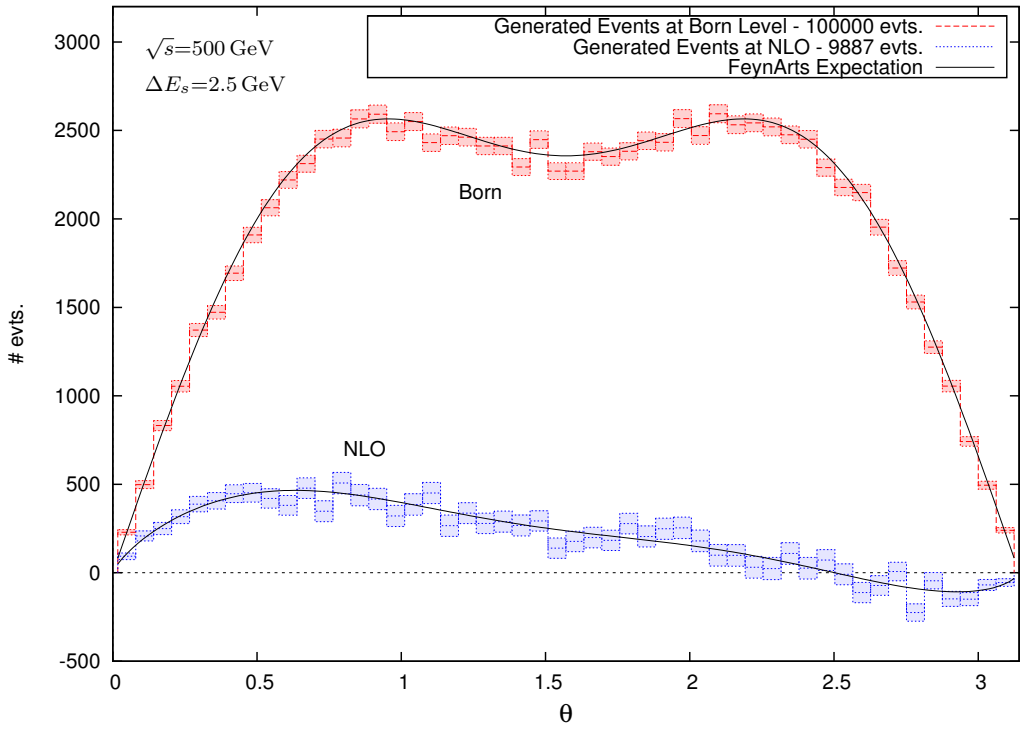

Figure 6.2: Generated events for s-channel Bhabha scattering. Born (red/dashed) and NLO (blue/dotted) results are shown with corresponding statistical error. Results are compared with the expectation from FeynArts (black/solid) calculation.

Therefore, it is natural that the integrand is spread among positive and negative values which hampers an efficient event generation. Here, a further manipulation of the integrand like mapping the negative onto the positive parts might be necessary in some cases. We added the Born cross section to the one loop corrections spread over the whole integration volume. Concentrating only on parts of the phase space where the integrand is negative can also help to increase the efficiency of event generation. However, both methods require a more detailed knowledge of the integrand.

Event Generation in Forward Region

A more physical application is event generation in the forward region. At the ILC, the luminosity will be measured via Bhabha scattering in this region. The values for the covered regions of the LumiCal differ for the detector concepts and beam crossing angle at the interaction point. Here, we take $r_{\min} = 26\,\text{mrad}$ and $r_{\max} = 154\,\text{mrad}$, cf. [87]. Again, we will use $\sqrt{s} = 500\,\text{GeV}$. The infrared cutoff is set to $\Delta E_s = 5\,\text{GeV}$. This time, we use the full $\mathcal{O}(\alpha)$ result.

The integrated cross sections are:

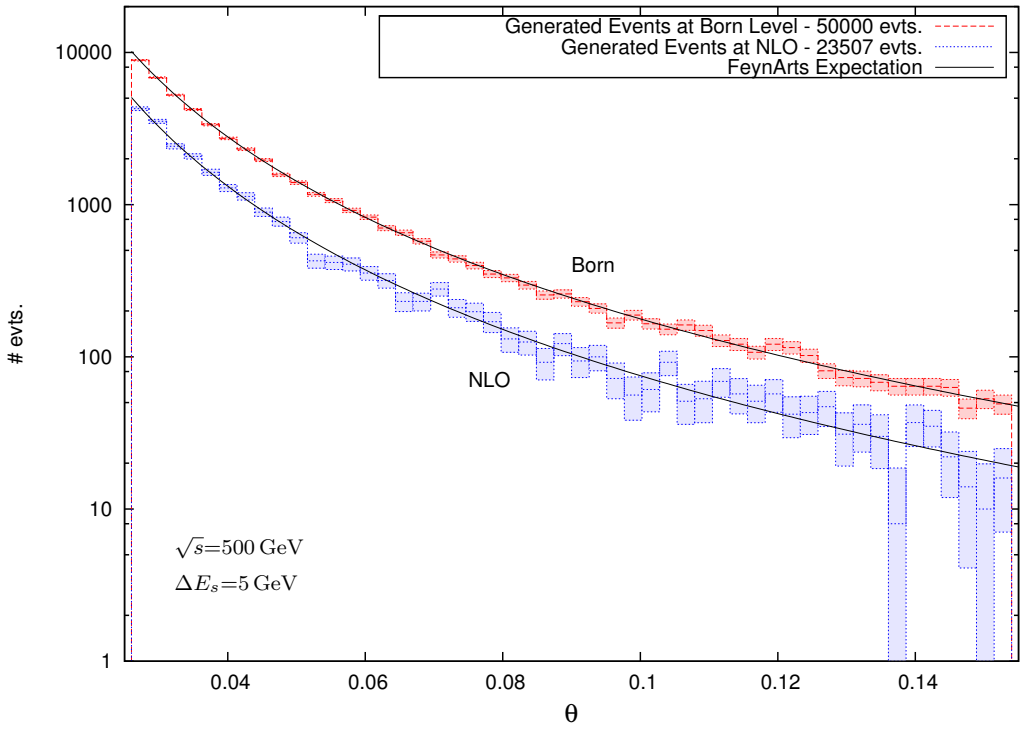

Figure 6.3: Generated events for Bhabha scattering in the forward region. Born (red/dashed) and NLO (blue/dotted) results are shown with corresponding statistical error. Results are compared with the expectation from FeynArts (black/solid) calculation.

$$\sigma^{\text{tot}}_{\text{Born}} = 5981.3(3.3)\text{pb}; \qquad \sigma^{\text{tot}}_{\text{NLO}} = 2812(24)\text{pb}. \tag{6.10}$$

To take the steep fall of the cross section over the polar angle into account, we generate 50000 events for the Born distribution, leading to 23507 events for the NLO result. For the Born result, the efficiency of sampling events was

$$\text{eff}_{\text{Born}} = 65\%, \tag{6.11}$$

similar to the pure s-channel result. Again, the integrand of the NLO result gets negative for some regions of the phase space. To sample 23507 events filling the histogram of figure 6.3, we needed 84859 events, 54183 positive and 30676 negative. The resulting efficiency for accepting events was

$$\text{eff}^{\text{p+n}}_{\text{NLO}} = 3.0\%, \tag{6.12}$$

counting only events in the histogram of figure 6.3, the efficiency drops down to 0.8%.

Summary of the Results

As was anticipated in the simple example above, the extension of the phase space sampling to the inclusive momentum of the additional incoming and outgoing particle of the cutting procedure of the Feynman Tree Theorem lead to a decrease of the efficiency of event generation. While the efficiency of event generation decreases, the speed of sampling the phase space increases considerably. For each sampled point the integrand of the cross section, consisting of rather simple rational functions is evaluated only once. This does not include integrations over internal parameters or the evaluation of complicated functions like multiple polylogarithms or harmonic sums. We expect this gain in speed to outweigh the decrease in efficient event generation for multi leg amplitudes, when the analytic expressions, if any are available at all, get too large and involve expressions like those mentioned before.

A further decrease in the efficiency was encountered by the generation of negative events. Since in any final analysis, these events have to be subtracted from those with positive uniform weight, the effective number of events is lower than the number of all generated events. In general, further manipulation of the integrands allowing for a better grid adaption and less number of negative events are a possibility to optimize unweighted event generation with the suggested method.

7. Summary and Outlook

The upcoming experiments at the LHC and the ILC require precise theoretical predictions for the analysis of the final states in collision processes. Therefore, calculations of matrix elements with many legs and beyond leading order in perturbation theory are needed. Because of the increasing number of terms, the complicated expressions for loop integrals, and the occurrence of divergences, the level of complexity of these computations rises with the number of external legs and the number of loops. Even for four particles in the final state only few processes are completely evaluated at NLO. The computation of higher order scattering amplitudes and the development of automated tools for cross section integrations and event generation is a pressing task of theoretical high energy physics.

We developed a method for the numerical evaluation of loop integrals from tree graphs, which is well suited for automatization. As a key ingredient, we derived an improved version of the Feynman Tree Theorem, which states that one-loop diagrams can be expressed as a sum of tree graphs with additional on-shell particles. The tree graphs result from all possible replacements of a propagator by a delta function (cuts) of the loop. The original four dimensional loop integration is replaced by a phase space integration over the additional on-shell particle momenta. In the improved version of the Tree Theorem, no $i\epsilon$ terms are present, which allows for a direct numerical integration. In cross section calculations or event generation, this integration can be performed simultaneously with the phase space integrations of the external particles. For multi-leg amplitudes this is an advantage over methods where complicated expressions for the loop integrals have to be completely evaluated for each point in the phase space of the external particles. Furthermore, there exist automated matrix element generators for tree level graphs, which considerably simplifies an implementation of the proposed method in a Monte Carlo event generator.

A similar method, which also allows for a full numerical evaluation, was presented in [46–48]. Contrary to that, we exclusively work in real momentum space and apply our method to massive graphs. Furthermore, no contour deformation is needed to avoid on-shell singularities.

These singularities can arise in parts of the phase space, after propagators of a loop are cut. We gave a detailed analysis of the peak structure of the tree graphs and showed a correlation between the peaks and the terms resulting from multiple cuts of the loop. We showed the construction of fix functions, acting as subtraction terms to cancel the on-shell singularities such that the integrand can be efficiently evaluated by Monte Carlo integration routines. In the case of overlapping peaks in the integration region, an approximative subtraction method was presented. We demonstrated the explicit construction of the fix functions as well as the calculation of terms with multiple delta functions in a diagram with a complicated peak structure. The numerical evaluation agreed with results from LoopTools.

The infrared divergent structure of the cut loops was examined. We showed a direct relation of tree graphs with an additional massless on-shell particle and the associated soft real emission graph. Adding both graphs under the phase space integral, the infrared divergences cancel. We presented a modified BPHZ regularization procedure and showed the explicit construction of subtraction terms, such that ultraviolet divergences and remaining infrared divergences are canceled and the renormalization conditions are fulfilled.

As a proof of principle, we applied the presented method to Bhabha scattering in QED. We wrote a Mathematica program which creates loop graphs and the associated real emission graphs and calculates the interference with the Born terms. The loops are cut and fix functions constructed. To achieve an efficient numerical evaluation with a single channel routine, we applied further mappings of the integrand and the integration variables. Using the same process, we also presented results of a simplified event generator. We simulated events for Bhabha scattering at energies typical for the ILC. In both cases, the cross section integration and the event generation, the results are in agreement with those obtained from FeynArts, which proves the applicability of this method to computations in collider physics.

In the case of a four-point function, we also demonstrated the applicability of the Tree Theorem to loop evaluations by creating tree level amplitudes with the matrix element generator O'Mega and performing a multi channel integration with VAMP. Here, we used the information about the collinear peak structure of the tree graphs to set up proper channels for the integration routine.

Except for the subtraction graphs from the BPHZ procedure and the fix functions added to smooth internal peaks, no further additions or manipulations to the tree graphs have to be applied to prepare the integrands for the numerical evaluation. This does not change when scattering amplitudes with a higher number of external legs are considered. Thus, the level of complexity solely rises due to the increasing number of tree graphs, contrary to methods where algebraic reduction techniques or analytic evaluations have to become more and more sophisticated. We therefore expect this method to be an efficient tool for computing multi-leg processes.

Outlook

In this thesis, we gave a proof of concept for the evaluation of loop integrals from tree graphs. In the case of QED, we established a consistent procedure to cancel ultraviolet and infrared divergences such that the renormalization conditions are fulfilled simultaneously. For an extension to the electroweak standard model, an algorithm that automatically guarantees that the Slavnov-Taylor identities are fulfilled is still missing. An inclusion of propagators with a finite width should be possible within the presented framework. For the treatment of collinear divergences coming from two massless particles, we have to consider further subtraction terms or regularization procedures.

The simplicity of the proposed method calls for an implementation in a Monte Carlo event generator. We already showed the possibility of evaluation of a loop graph by tree

amplitudes created with O'MEGA. However, the matching of the momenta of the different tree graphs, the addition of a fix function and the creation of channels for the integration routine were carried out manually. The full implementation in the O'MEGA-WHIZARD framework will be the main focus of future work.

A. Conventions

A.1. Constants, Metric and Dirac Matrices

Throughout this thesis we use

$$\hbar = c = 1. \tag{A.1}$$

We use as metric tensor:

$$g_{\mu\nu} = g^{\mu\nu} = \mathrm{diag}(1, -1, -1, -1). \tag{A.2}$$

We take the Weyl basis for the Dirac Matrices:

$$\gamma^\mu = \begin{pmatrix} 0 & \sigma^\mu \\ \bar{\sigma}^\mu & 0 \end{pmatrix}, \quad \gamma^5 = \begin{pmatrix} -\mathbf{1} & 0 \\ 0 & \mathbf{1} \end{pmatrix}, \tag{A.3}$$

where $\sigma^\mu = (\mathbf{1}, \vec{\sigma})$ and $\bar{\sigma}^\mu = (\mathbf{1}, -\vec{\sigma})$ and σ_i are the Pauli matrices:

$$\sigma_1 = \begin{pmatrix} 0 & 1 \\ 1 & 0 \end{pmatrix}, \quad \sigma_2 = \begin{pmatrix} 0 & -i \\ i & 0 \end{pmatrix}, \quad \sigma_3 = \begin{pmatrix} 1 & 0 \\ 0 & -1 \end{pmatrix}, \tag{A.4}$$

such that the Dirac algebra is fulfilled:

$$\{\gamma^\mu, \gamma^\nu\} = 2g^{\mu\nu} \cdot \mathbf{1}, \quad \{\gamma^\mu, \gamma^5\} = 0. \tag{A.5}$$

Physical Input Parameters

In the numerical evaluations of this thesis, values for physical constants and masses are taken from [5].

A.2. Helicity Eigenstates

In the following we will list our conventions helicity eigenstates of the Dirac and bosonic wave functions. These are based on [88] and are also used in the matrix element generator O'MEGA [17].

We define the two-component spinors $\chi_\lambda(p)$ as helicity eigenstates:

$$\frac{\vec{\sigma}\vec{p}}{|\vec{p}|}\chi_\lambda(p) = \lambda\chi_\lambda(p), \tag{A.6}$$

with $\lambda = \pm 1$. Explicitly, we use:

$$\chi_+(p) = \frac{1}{\sqrt{2|\vec{p}|\,(|\vec{p}| + p_z)}} \begin{pmatrix} |\vec{p}| + p_z \\ p_x + ip_y \end{pmatrix}, \tag{A.7}$$

$$\chi_-(p) = \frac{1}{\sqrt{2|\vec{p}|\,(|\vec{p}| + p_z)}} \begin{pmatrix} -p_x + ip_y \\ |\vec{p}| + p_z \end{pmatrix}, \tag{A.8}$$

except in the case $|\vec{p}| + p_z = 0$, where we use

$$\chi_+(p) = \begin{pmatrix} 0 \\ 1 \end{pmatrix}, \tag{A.9}$$

$$\chi_-(p) = \begin{pmatrix} -1 \\ 0 \end{pmatrix}. \tag{A.10}$$

Using these spinors we can compose the upper and lower component of the Dirac four-spinors u and v:

$$\omega_\pm u(p,\lambda) = u_\pm(p,\lambda) \quad \omega_\pm v(p,\lambda) = v_\pm(p,\lambda), \tag{A.11}$$

with $\omega_\pm = \frac{1}{2}(1 \pm \gamma_5)$ being the projector on the chiral states $(L,R) \hat{=} (-,+)$. Taking

$$u_\pm(p,\lambda) = \pm v_\pm(p,\lambda) = \rho_{\pm\lambda}(p)\chi_\lambda(p), \tag{A.12}$$

$$\rho_{\pm\lambda}(p) = \sqrt{p_0 \pm |\vec{p}|}, \tag{A.13}$$

the resulting spinor wave functions fulfill the Dirac equation and are helicity eigenstates at the same time.

In the case of a bosonic wave function $\epsilon^\mu(p,m,\lambda)$, we use for general directions of the momentum $\vec{p}$:

$$\epsilon^\mu(p,m,+) = \frac{1}{\sqrt{2(p_x^2+p_y^2)}} \begin{pmatrix} 0 \\ \frac{p_x p_z}{|\vec{p}|} - ip_y \\ \frac{p_y p_z}{|\vec{p}|} + ip_x \\ -\frac{p_x^2+p_y^2}{|\vec{p}|} \end{pmatrix}, \qquad \epsilon^\mu(p,m,-) = \epsilon^{\mu *}(p,m,+). \tag{A.14}$$

In the case of a massive boson there exists a third physical helicity state:

$$\epsilon^\mu(p,m,0) = \frac{p_0}{m|\vec{p}|} \begin{pmatrix} \frac{|\vec{p}|^2}{p_0} \\ p_x \\ p_y \\ p_z \end{pmatrix}. \tag{A.15}$$

For particles moving along the positive z-axis, we use:

$$\epsilon^\mu(p,m,+) = \frac{1}{\sqrt{2}} \begin{pmatrix} 0 \\ 1 \\ i \\ 0 \end{pmatrix} \quad \epsilon^\mu(p,m,-) = \frac{1}{\sqrt{2}} \begin{pmatrix} 0 \\ 1 \\ -i \\ 0 \end{pmatrix}, \tag{A.16}$$

and change sign of the x-component of $\epsilon^\mu_\pm$ if the particle is moving in the negative z-direction. For massive particles at rest we define the helicity relative to the positive z-axis. Thus, in addition to the vectors of equation (A.16) we have

$$\epsilon^\mu(p,m,0)|_{\vec{p}=0} = \begin{pmatrix} 0 \\ 0 \\ 0 \\ 1 \end{pmatrix}. \tag{A.17}$$

These polarization vectors are orthogonal to each other and the four-vector p:

$$\epsilon^\mu(p,m,\lambda)\cdot\epsilon^*_\mu(p,m,\lambda') = -\delta_{\lambda\lambda'}, \quad \epsilon^\mu(p,m,\lambda)\cdot p_\mu = 0. \tag{A.18}$$

A.3. Lorentz Transformation

We use the following parameterization for a Lorentz boost into the rest frame of a four-vector. Define the three-velocity and the Lorentz-factor γ of a four-vector $p^\mu = (p^0, \vec{p})$ with positive invariant mass p^2 as:

$$\vec{\beta} = \frac{\vec{p}}{p^0}, \quad \gamma = \frac{|p^0|}{\sqrt{p^2}}, \tag{A.19}$$

the corresponding Lorentz boost into the rest frame can be written in matrix form as:

$$\Lambda_{\mu\nu}(\beta) = \begin{pmatrix} \gamma & -\gamma\beta_1 & -\gamma\beta_2 & -\gamma\beta_3 \\ -\gamma\beta_1 & 1+\frac{(\gamma-1)\beta_1^2}{\beta^2} & \frac{(\gamma-1)\beta_1\beta_2}{\beta^2} & \frac{(\gamma-1)\beta_1\beta_3}{\beta^2} \\ -\gamma\beta_2 & \frac{(\gamma-1)\beta_1\beta_2}{\beta^2} & 1+\frac{(\gamma-1)\beta_2^2}{\beta^2} & \frac{(\gamma-1)\beta_2\beta_3}{\beta^2} \\ -\gamma\beta_3 & \frac{(\gamma-1)\beta_1\beta_3}{\beta^2} & \frac{(\gamma-1)\beta_2\beta_3}{\beta^2} & 1+\frac{(\gamma-1)\beta_3^2}{\beta^2} \end{pmatrix}. \tag{A.20}$$

This transforms the four-vector p^μ into its rest frame:

$$\Lambda_{\mu\nu}(\vec{\beta}(p))p^\nu = \left(\frac{p^0}{|p^0|}\sqrt{p^2}, 0, 0, 0\right). \tag{A.21}$$

Often, the spatial part of a Lorentz transformed on-shell vector $k^\mu = (k_0, \vec{k})$, with $k^2 = m^2$, is needed:

$$\overrightarrow{\Lambda(\beta)k} = \left(\frac{\gamma-1}{\beta^2}\vec{\beta}\vec{k} - \gamma k_0\right)\cdot\vec{\beta} + \vec{k}. \tag{A.22}$$

From this, one can deduce the Jacobian

$$\left|\frac{d^3k'}{d^3k}\right| = \gamma\left(1 - \frac{\vec{\beta}\vec{k}}{k_0}\right). \tag{A.23}$$

Also of interest is the square of (A.22):

$$\overrightarrow{\Lambda(\beta)k}^2 = \gamma^2\left(k_0 - \vec{\beta}\vec{k}\right)^2 - m^2. \tag{A.24}$$

B. Renormalization of the Photon Self-Energy

In D dimensions, the photon self-energy, sometimes called vacuum polarization, is given by:

$$-i\Sigma_{\mu\nu} = -e^2\mu^{4-D}\int\frac{d^Dk}{(2\pi)^D}\frac{\mathrm{Tr}\{\gamma_\mu(\not{k}+m)\gamma_\nu(\not{k}+\not{p}+m)\}}{(k^2-m^2)((k+p)^2-m^2)}. \tag{B.1}$$

After evaluating the trace and subsequent tensor reduction we obtain an expression in terms of scalar integrals:

$$\begin{aligned} -i\Sigma_{\mu\nu} &= -i\frac{\alpha}{2\pi}\left[g_{\mu\nu}\left(4B_{00}(p^2,m,m)-2A_0(m)+p^2B_0(p^2,m,m)\right)\right. \\ &\quad \left.+4p_\mu p_\nu\left(B_{11}(p^2,m,m)+B_1(p^2,m,m)\right)\right]. \end{aligned} \tag{B.2}$$

This can further be reduced to

$$-i\Sigma_{\mu\nu} = \left(g_{\mu\nu}-\frac{p_\mu p_\nu}{p^2}\right)\Sigma_T^{AA}(p^2), \tag{B.3}$$

where

$$\Sigma_T^{AA}(p^2) = -i\frac{\alpha}{3\pi}\left[(p^2+2m^2)B_0(p^2,m,m)-2m^2B_0(0,m,m)-\frac{p^2}{3}\right]. \tag{B.4}$$

The longitudinal part vanishes as expected. We expand in a Taylor series around $\bar{p}=\epsilon p$ and take the limit $\epsilon\to 0$ afterwards, such that $\bar{p}^2\to 0$ and

$$\left(g_{\mu\nu}-\frac{\bar{p}_\mu\bar{p}_\nu}{\bar{p}^2}\right) = \left(g_{\mu\nu}-\frac{p_\mu p_\nu}{p^2}\right). \tag{B.5}$$

Taking the first derivative, we get:

$$\begin{aligned} p^\rho\frac{\partial}{\partial p^\rho}\left(g_{\mu\nu}-\frac{p_\mu p_\nu}{p^2}\right)\Sigma_T^{AA}(p^2)\Big|_{p=\bar{p}} &= p^\rho\left(-g_{\mu\rho}\bar{p}_\nu-g_{\rho\nu}\bar{p}_\mu+\frac{2\bar{p}_\mu\bar{p}_\nu\bar{p}_\rho}{\bar{p}^2}\right)\frac{1}{\bar{p}^2}\Sigma_T^{AA}(\bar{p}^2) \\ &\quad +p^\rho\left(g_{\mu\nu}-\frac{\bar{p}_\mu\bar{p}_\nu}{\bar{p}^2}\right)2\bar{p}_\rho\Sigma_T^{AA\prime}(\bar{p}^2). \end{aligned} \tag{B.6}$$

The limit

$$\lim_{\bar{p}^2\to 0}\frac{1}{\bar{p}^2}\Sigma_T^{AA}(\bar{p}^2) = -i\frac{\alpha}{3\pi}\left[B_0(0,m,m)+2m^2B_0'(0,m,m)-\frac{1}{3}\right] \tag{B.7}$$

is well defined and the first derivative vanishes for $\epsilon\to 0$. The second derivative is

$$\frac{p^\sigma p^\rho}{2}\frac{\partial^2}{\partial p^\rho\partial p^\sigma}\left(g_{\mu\nu}-\frac{p_\mu p_\nu}{p^2}\right)\Sigma_T^{AA}(p^2)\Big|_{p=\bar{p}} = \cdots = \left(g_{\mu\nu}-\frac{p_\mu p_\nu}{p^2}\right)p^2\Sigma_T^{AA\prime}(\bar{p}^2). \tag{B.8}$$

Thus, the renormalized photon self-energy is:

$$
\begin{aligned}
-i\hat{\Sigma}_{\mu\nu} &= \left(g_{\mu\nu} - \frac{p_\mu p_\nu}{p^2}\right)\left[\Sigma_T^{AA}(p^2) - \Sigma_T^{AA}(0) - p^2\Sigma_T^{AA\prime}(0)\right], \\
&\equiv \left(p^2\, g_{\mu\nu} - p_\mu p_\nu\right) i\hat{\Sigma}_T^{AA}, \qquad \text{(B.9)} \\
\hat{\Sigma}_T^{AA}(p^2) &= -\frac{1}{p^2}\frac{\alpha}{3\pi}\left[(p^2+2m^2)\left(B_0(p^2,m,m) - B_0(0,m,m)\right) - 2m^2p^2B_0'(0,m,m)\right]. \qquad \text{(B.10)}
\end{aligned}
$$

Multiplying the two adjacent propagators to the left and to the right of the transverse Lorentz structure, the self-energy part acts as projector onto the transverse propagator:

$$
i\Delta^{\rho\mu}(-i\hat{\Sigma}_{\mu\nu})i\Delta^{\nu\sigma} = \frac{i}{p^2+i\epsilon}\left(-g^{\rho\sigma} + \frac{p^\rho p^\sigma}{p^2}\right)\hat{\Sigma}(p^2). \qquad \text{(B.11)}
$$

This coincides with textbook results, e.g. cf. [4]. Thus, the one loop correction to photon propagators can be evaluated by adding the tree level amplitude times the correction factor $\hat{\Sigma}_T^{AA}(p^2)$:

$$
\mathcal{M}^{(1)} = \ldots + \hat{\Sigma}_T^{AA}(p^2)\mathcal{M}^{(0)} + \ldots. \qquad \text{(B.12)}
$$

The replacement of the Lorentz structure of the propagator is not necessary, since the photon propagator is connected to a Dirac field bilinear. Due to current conservation, only the part proportional to $g_{\mu\nu}$ contributes.

The renormalized photon self-energy B.10 is not only ultraviolet finite, but also infrared safe. We can choose to evaluate it analytically or by using the tree theorem.

Analytically, we get [4]:

$$
\begin{aligned}
B_0'(0,m,m) &= \frac{1}{6m^2}, \qquad \text{(B.13)} \\
B_0(p^2,m,m) - B_0(0,m,m) &= -\frac{m^2}{p^2}\left(\frac{1}{r} - r\right)\log r, \qquad \text{(B.14)} \\
r &= \frac{-p^2 + 2m^2 - i\epsilon \pm \sqrt{(p^2 - 2m^2 + i\epsilon)^2 - 4m^4}}{2m^2}. \qquad \text{(B.15)}
\end{aligned}
$$

Since the difference of the two scalar B_0 integrals is UV finite, we can re-express it in the form of one loop integral without the need of a regulator:

$$
B_0(p^2,m,m) - B_0(0,m,m) = -\frac{1}{i\pi^2}\int d^4k \frac{(p^2+2kp)}{(k^2-m^2)^2((k+p)^2-m^2)}. \qquad \text{(B.16)}
$$

We evaluate this integral in three different regions of the squared momentum p^2.

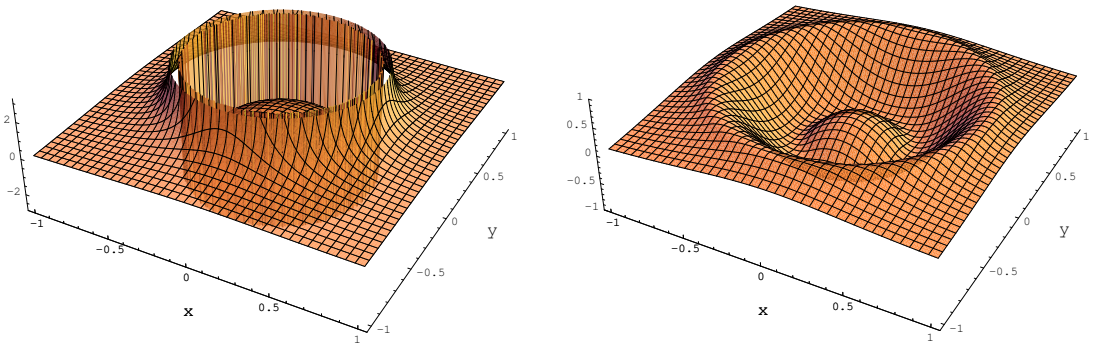

Figure B.1: Integrand of (B.16) after k_0-integration for $p^2 > 0$. The arising singularity is smoothed by addition of a fix function.

- $0 < p^2 < 4m^2$

  Here, the kinetic function λ (3.28) is always negative and we therefore do not encounter any singularities (cf. section 3.2). Since the vacuum polarization is only dependent on the momentum squared, we use the parameterization $p_\mu = (\sqrt{p^2}, 0, 0, 0)$. After k_0-integration the two terms of the integrand read:

$$I_1 = \frac{1}{\pi\sqrt{p^2}\sqrt{r^2+m^2}(2\sqrt{r^2+m^2}-\sqrt{p^2})}, \tag{B.17}$$

$$I_2 = -\frac{(\sqrt{r^2+m^2}+\sqrt{p^2})^2+(r^2+m^2)}{2\pi\sqrt{p^2}(r^2+m^2)^{3/2}(2\sqrt{r^2+m^2}+\sqrt{p^2})}. \tag{B.18}$$

  Here, we switched to spherical coordinates. Since the singularity of the first factor in the denominator of (B.16) is of second order, we had to take the derivative with respect to k_0 before picking up the pole to obtain I_2 . Adding the two terms yields

$$I = \frac{p^2}{2\pi(r^2+m^2)^{3/2}(4(r^2+m^2)-p^2)}, \tag{B.19}$$

  which can easily be integrated numerically.

- $p^2 < 0$

  In this region we cannot find a rest frame with $\vec{p} = 0$. Using $p_\mu = (0, 0, 0, \sqrt{-p^2})$, we get the following two terms after the k_0-integration.

$$I_1 = \frac{1}{\pi(p^2-2\sqrt{-p^2}r\cos\theta)\sqrt{r^2+m^2-p^2+2\sqrt{-p^2}r\cos\theta}}, \tag{B.20}$$

$$I_2 = -\frac{2(r^2+m^2)+p^2-2\sqrt{-p^2}r\cos\theta}{2\pi(r^2+m^2)^{3/2}(p^2-2\sqrt{-p^2}r\cos\theta)}. \tag{B.21}$$

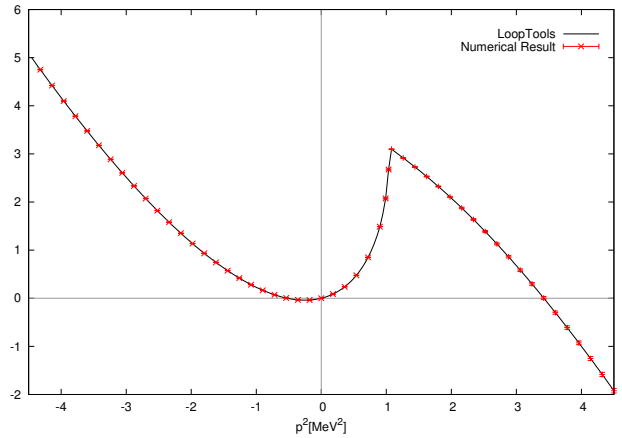

Figure B.2: Scalar 2pt integrals (B.16) from LoopTools and numerical evaluation.

Note that both terms become singular at a surface in the integration region. The two singularities cancel in the sum of both terms. One can therefore numerically integrate the sum of both terms. However, we can also use (B.19) in this region of p^2 since we do not encounter any singularities when we analytically continue from one regime to the other.

- $4m^2 < p^2$

  In this region (B.17) becomes singular on a spherical surface in the integration region. This peak indicates the existence of an imaginary part of the photon self-energy. The momentum through the two point function is high enough to produce two real fermions. This can also be seen from the analytical result (B.14), when r becomes negative. To get an integrand which can safely be evaluated numerically, we calculate the fix function with the procedure presented in section 3.2.2. Since we are already in the rest frame of p, we do not have to impose a Lorentz transformation. However, because of the second order pole the calculation of the residue involves again one derivative with respect to k_0. To illustrate the effect of the fix functions, we plotted the original integrand and the fixed integrand in figure B.1. Here, we used $p^2 = 9m^2$ with m being the mass of the electron such that the integrand gets singular at $r = \sqrt{5}m$.

The result after integration of (B.16) is shown in figure B.2 for the interesting range around $p^2 = 0$ and $p^2 = 4m^2$. On top of the same graph we also depicted the analytic result obtained by using LoopTools. The results coincide within the errors of the numerical calculation ($\approx .1\%$).

In chapter 5, we evaluated the contribution of the photon self-energy correction to Bhabha scattering. The constant term arising from (B.13) was incorporated by adding

$$\mathcal{M}^{(1)} = \cdots + \frac{\alpha}{3\pi}\frac{1}{3V}\mathcal{M}^{(0)} + \ldots \tag{B.22}$$

to the integrand, where V is the volume of the integration region.

C. Sample Calculation of a Function with Overlapping Peaks

To demonstrate the occurrence of peaks when propagators of loops are cut and the construction of fix functions to smooth these peaks, we will evaluate the scalar three-point function depicted in figure C.1. We will also calculate the contributions of the sub-leading terms of equation (3.15), which give rise to an imaginary part and a further real part. The integral we are going to calculate is

$$C_0 = \frac{1}{i\pi^2}\int d^4k \frac{1}{k^2-m^2}\frac{1}{(k-p_1)^2-m^2}\frac{1}{(k-p_2)^2-m^2}, \tag{C.1}$$

where we set the masses of all internal lines to m. In the final numerical calculations we will set this mass equal to 1. For the external momenta, will use the following settings:

$$p_1 = \begin{pmatrix} 3m \\ 0 \\ 0 \\ 0 \end{pmatrix}, \quad p_2 = \begin{pmatrix} 3m \\ 0 \\ 0 \\ m \end{pmatrix}. \tag{C.2}$$

The three-point function (C.1) has a rather simple analytic solution. Using LoopTools, the library included in the FormCalc package, we get the answer for $m = 1$:

$$C_0 = 0.274156 - \, i\,0.503924. \tag{C.3}$$

Opening the Loop and Construction of Fix Functions

We begin by cutting the second propagator in (C.1). From equation (3.8) we get the corresponding delta function

$$\Delta_1^l = -\frac{2\pi i}{2E_i}\delta(k^0 - (-3m + \sqrt{r^2+m^2})), \tag{C.4}$$

where we switched to spherical coordinates for the loop momentum. The additional factor i stems from the numerator of the propagators, which we set to 1 instead of i as in the analysis leading to (3.8). Since the square of the difference of the momenta of propagators 2 and 3, $p_{32}^2 = (p_2 - p_1)^2 = -m^2$ is negative, we expect a peak in the integration region where the third propagator gets singular. This is the case for $\cos\theta = 0$. The left plot of figure C.2 shows the integrand in the $x - z$ plane. As argued in section 3.2, we get another peak at the same position when the third propagator is cut. The two singularities cancel each other in the sum, which can be seen in the right plot of figure C.2.

When the first propagator is cut, the resulting integrand reads:

$$C'_{0,1} = -\frac{2}{\pi}\int \frac{r^2 dr d\Omega}{2\sqrt{r^2+m^2}} \frac{1}{9m^2 - 6m\sqrt{r^2+m^2}} \frac{1}{8m^2 - 6m\sqrt{r^2+m^2} + 2mr\cos\theta}. \tag{C.5}$$

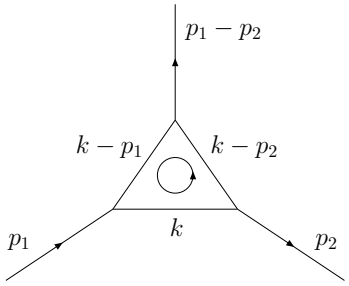

Figure C.1: Scalar 3pt-function at unphysical kinematic momenta p_i.

The prime at C_0' indicates the contribution to the integral C_0 if one propagator is cut. Here, the second and third propagator get singular on surfaces in the integration region, given by the following equations:

$$I: \qquad r_0 = \frac{\sqrt{5}}{2}m, \tag{C.6}$$

$$II: \qquad \frac{x_0^2}{m^2} + \frac{y_0^2}{m^2} + \frac{8(z_0 - \frac{m}{2})^2}{9m^2} = 1. \tag{C.7}$$

These two surfaces, a sphere and a rotational ellipsoid overlap. In the upper plot of figure C.3, we showed the integrand (C.5) in the $x - z$ plane.

Since we are already in the rest frame of the difference of the two momenta flowing through propagators 1 and 2, the fix function for the peak arising from the singularity of the second propagator is easily found:

$$\mathrm{Fix}_1 = -\frac{2}{\pi}\int dr d\Omega \frac{\sqrt{5}}{12m^2(2r - \sqrt{5}m)(1 - \sqrt{5}\cos\theta)}\left(1 - \frac{(2r - \sqrt{5}m)^2}{4c^2}\right)^2 \theta(r, r_0, c). \tag{C.8}$$

Here, $\theta(r, r_0, c)$ stands for the product of the two step functions:

$$\theta(r, r_0, c) = \theta\left(r - (r_0 - c)\right)\theta\left((r_0 + c) - r\right). \tag{C.9}$$

Subtracting this function from the original integrand (C.5), the peak coming from the singularity of the second propagator vanishes as can be seen in the second plot of figure C.3. Constructing the fix function for the second peak in the same manner will lead to a singular structure in the overlapping region which cannot be fully compensated as argued in section 3.2.2. We will therefore proceed along the line proposed in that section.

We fix the second peak by Lorentz transforming into the rest frame of $p_{31} = -p_2 + p_1$, where the rotational ellipsoid becomes a sphere with radius r_0' given by equation (3.39). Here,

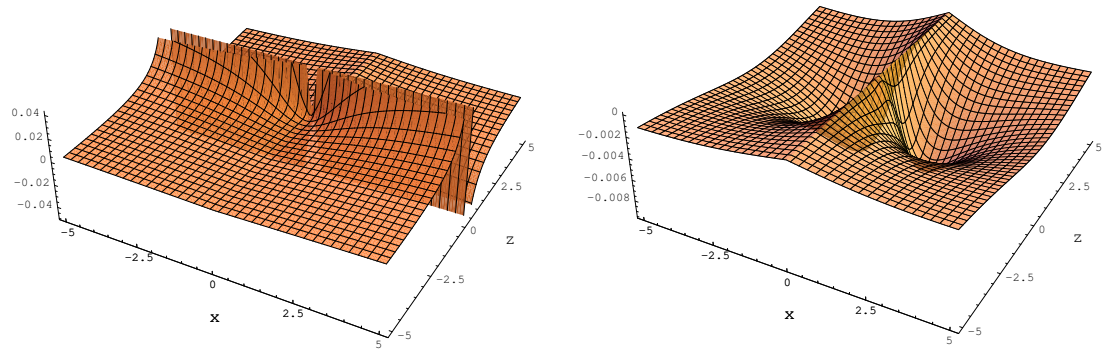

Figure C.2: Occurrence of a peak at $z = 0$ in the case $p_{ij}^2 < 0$ (left plot). The same peak with opposite sign arises when the respective second propagator is cut. The two peaks cancel in the sum as is shown in the right plot.

we calculate the fix function as usual, with the exception of not taking the limit $r' \to r'_0$ in the second propagator. Transforming back, we obtain a fix function which smooths the second peak. However, this fix function adds a non-zero value to the integrand which vanishes only in the limit of the width c going to zero. Explicitly, this fix function reads

$$\mathrm{Fix}_2 = \frac{2}{\pi}\int dr d\Omega \frac{2r^2(3\sqrt{r^2+m^2} - r\cos\theta)}{\sqrt{r^2+m^2}(2\sqrt{r^2+m^2}-3m)r'^2(r'-4m)}\left(1-\frac{(r'-4m)^2}{16c^2}\right)^2 \theta(r', r'_0, c), \tag{C.10}$$

where r' is given by:

$$r' = \sqrt{2m^2 + 19r^2 - 12r\sqrt{r^2+m^2}\cos\theta + r^2\cos 2\theta}. \tag{C.11}$$

The third fix function is obtained by taking the residue of the second fix function (C.10) at $r = r_0$ and again multiplying with (3.53) and the corresponding theta functions:

$$\mathrm{Fix}_3 = -\frac{2}{\pi}\int dr d\Omega \frac{\sqrt{5}(\sqrt{5}\cos\theta - 9)}{6m(\sqrt{5}m - 2r)r'^2_r(r'_r - 4m)}\left(1-\frac{(r'_r-4m)^2}{16c^2}\right)^2\left(1-\frac{(2r-\sqrt{5}m)^2}{4c^2}\right)^2$$
$$\cdot\theta(r'_r, r'_{r0}, c)\theta(r, r_0, c). \tag{C.12}$$

Here, r'_r is the radial coordinate in the rest frame of the third propagator at a fixed value of the radial coordinate of the integration system:

$$r'_r = \frac{m}{2}\sqrt{5\cos 2\theta - 36\sqrt{5}\cos\theta + 103}. \tag{C.13}$$

Subtracting the first two fix functions from (C.5) and adding the third we get a smooth integrand as depicted in the last plot of figure C.3.

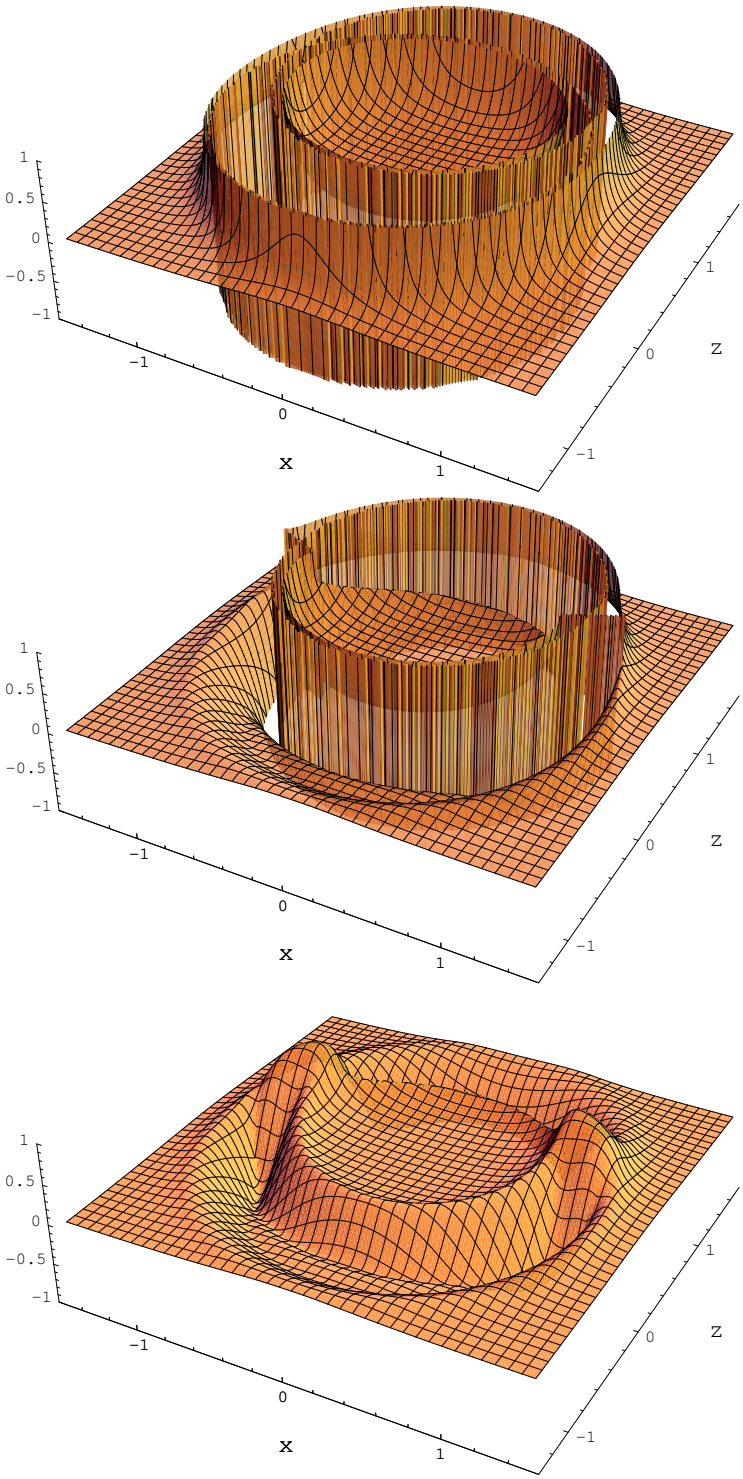

Figure C.3: Upper plot: When the first propagator of (C.1) is cut the two remaining propagators can become singular. The corresponding peaks overlap. Middle plot: A fix function is added to remove the first peak. Lower plot: Integrand after addition of three fix functions. All singular peaks vanish. For better illustration, we plotted the integrands without the integration measure $r^2 \sin\theta$.

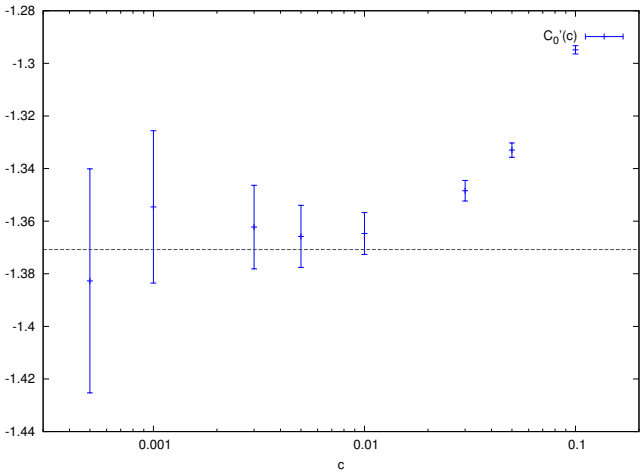

Figure C.4: Numerical evaluation of the three-point function C_0' for different values of the width c used by the fix functions. Towards a smaller width the true value of the integral is approximated, however, the numerical error increases due to the growing peak structure.

Integration

The fixed integrand has a rather smooth structure and therefore an adaptive integration method can give reliable results. However, the fix functions we used add a finite value to the integrand and only in the limit $c \to 0$ where effectively no fix function is added at all the true value of the integrand is reached. The smaller the width c, the more enhanced the peak structure gets, which hardens the adaption of the integration grid. Therefore more sample points are needed to obtain the same error estimation.

We integrated the fixed integrand, setting $m = 1$ and using the spherical coordinates introduced above. We used a simple mapping onto the unit interval $x \in [0, 1)$ for the radial coordinate

$$r = \frac{1}{1-x} - 1, \tag{C.14}$$

which sets the interesting region of about $r = 1$ in the center of the integration region of the new variable x. In figure C.4 we showed the numerical results dependent on the width c. For each integration we used the same amount of sampling points, 10^7, to show the increase of the error estimate of the numerical evaluation. In the evaluations of Feynman graphs for Bhabha scattering, cf. chapter 5, we set the width c equal to the infrared cutoff at about 1% of the center of mass energy. For the present analysis, the values in the percent region of the radii of the singularities also seem to give a reasonable trade-off between accuracy and efficiency of the numerical evaluation. The result at $c = .005$ is:

$$C_0' = -1.366(12). \tag{C.15}$$

We will calculate the contributions of the sub-leading terms in the following.

Terms with Multiple Delta Functions

The occurrence of peaks in terms of the expansion (3.15) in the Feynman Tree Theorem indicates a non-zero contribution of terms with more delta functions. Whenever one propagator is cut and another gets singular in the integration region, also this propagator can be replaced by a delta function and the product of both delta function does not vanish at the singularity. Therefore, each of the peaks in (C.5) implies a possible imaginary part, coming from terms with one Δ^l and one Δ^u in (3.15), and the overlap indicates a further real part coming from a term with one Δ^l and two Δ^u. Since each delta function decreases the dimension of the final numerical integration by one, the evaluation usually gets simpler for terms with more delta functions.

Replacing the first propagator in (C.1) by Δ^l and the second by Δ^u, we get:

$$C''_{0,1} = \frac{1}{2}\frac{1}{i\pi^2}(-2\pi i)^2 \int \frac{d^4k}{2\sqrt{\mathbf{k}^2+m^2}} \frac{\delta(k_0-\sqrt{\mathbf{k}^2+m^2})\delta\left(k_0-(-p_1^0-\sqrt{(\vec{k}-\vec{p}_1)^2+m^2})\right)}{2\sqrt{(\vec{k}-\vec{p}_1)^2+m^2}(p_2^2-2kp_2)}. \tag{C.16}$$

Here, we also included the factor $\frac{1}{2}$ coming from the coefficient C_{LUP} of equation (3.15). Performing the k_0-integration, switching to spherical coordinates and again performing the subsequent radial and azimuthal integration, we end up at:

$$C''_{0,1} = i\frac{\pi}{6m^2}\int_{-1}^{1}\frac{dx}{x-\frac{1}{\sqrt{5}}}, \tag{C.17}$$

where we substituted the polar coordinate by $x = \cos\theta$. This integral has again a singularity as expected from the fact that the two peaks in (C.5) overlapped. Again, we are only interested in the real part of the integration. The integral can easily be evaluated using Cauchy's principal value prescription. This yields with $m = 1$:

$$C''_{0,1} = -i\,0.503924. \tag{C.18}$$

Replacing the first and the third propagator by a delta function leads again to a one dimensional integral after performing the same steps as before. However, the explicit expression is rather complex and not very illuminating, so we do not list it here. The integrand again shows the expected singular behavior, however, this time the principal value vanishes.

For the contribution of the term where the first propagator is replaced by Δ^l and the other two by Δ^u, no numerical integration has to be performed at all. After integration over the delta functions and the trivial azimuthal integration the final result is:

$$C'''_0 = \frac{\pi^2}{6m^2}. \tag{C.19}$$

Final Result

Collecting all results of the above analysis, we get for the scalar three-point function:

$$C_0 = 0.279(12) - i\,0.503924. \tag{C.20}$$

Within the error this coincides with the LoopTools result (C.3). The contribution of the three delta term (C.19) is rather high and leads to a final result which is about one order of magnitude smaller than the numerical result of the leading terms (C.15). Thus, the relative error of the combined result increases considerably. To get a smaller relative error more sampling points have to be used in the numerical integration. Nevertheless, we showed that even in the case of overlapping peaks we can get a numerical result for loop integrals and there are no further theoretical limitations of an application of this method to multileg amplitudes.

D. Extension to Two Loops

In the case of connected multiple loops one might think to end up at different sets of tree graphs after cutting, depending on the order of the k_i^0-integration. As an example take the two loop graph depicted in figure D.1. In a first loop momentum assignment, the propagators labeled 1, 2, 3 might form the first loop while 3, 4, 5 the second. Then, there is one common propagator 3. Naively, if cutting the left loop first one would expect to obtain the tree graphs with cut propagators (1, 3) and (2, 3) twice while (3, 4) and (3, 5) appeared only once. In total one would get 10 tree graphs. One could also assign the momenta such that the outer propagators 1, 2, 4, 5 form a loop and the second loop is one of the inner loops. Starting with the outer loop one would get 12 tree graphs. In the following we will show that each combination of cutting the two loops appears only once, independent of the order of the integration.

The propagators of any two loop diagram can fall into three categories. The ones, which carry momentum of the first loop $F^{(1)}$, the ones which belong to both loops, $F^{(2)}$, and finally those which carry only the momentum of the second loop, $F^{(3)}$. Neglecting contribution from the numerator, the total two loop graph is then given by:

$$G_2 = F^{n_1} \star F^{n_2} \star F^{n_3}, \tag{D.1}$$

where for better readability we wrote

$$F^{n_i} = \prod_{k=1}^{n_i} F_k^{(i)}. \tag{D.2}$$

Using the same abbreviation for advanced Green functions we write:

$$F^{n_i} = (F^{n_i} - A^{n_i}) + A^{n_i}. \tag{D.3}$$

The first two terms can further be rewritten with the help of equation (3.10), where on the left hand side we have the product over the advanced Green functions, which is not zero in this case:

$$\begin{aligned} I^{(i)} &= F^{n_i} - A^{n_i}, && \text{(D.4)} \\ &= \sum \Delta^l F^{(i)} \cdots - \sum \Delta^l \Delta^l F^{(i)} \cdots + \ldots - (-1)^n \sum \Delta^l \cdots \Delta^l, \\ &= \sum_{\substack{perm. \\ U_i + L_i + P_i = n_i}} C_{LUP}\ \Delta^{l^{L_i}} \Delta^{u^{U_i}} P^{P_i}. && \text{(D.5)} \end{aligned}$$

In going from the second line to the third we made the same substitution as before to get to equation (3.15). Here, we did not explicitly wrote out the terms with only one Δ^l function, but included these also in the sum. The coefficient C_{LUP} is given as before, (3.16).

We therefore get for the two loop graph:

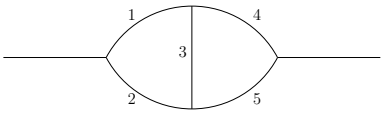

Figure D.1: Generic two loop graph.

$$\begin{aligned} G_2 &= I^{n_1} \star I^{n_2} \star I^{n_3} + A^{n_1} \star I^{n_2} \star I^{n_3} + I^{n_1} \star A^{n_2} \star I^{n_3} + I^{n_1} \star I^{n_2} \star A^{n_3} \\ &\quad + A^{n_1} \star A^{n_2} \star I^{n_3} + A^{n_1} \star I^{n_2} \star A^{n_3} + I^{n_1} \star A^{n_2} \star A^{n_3} + A^{n_1} \star A^{n_2} \star A^{n_3}. \end{aligned}$$

The terms in the second line vanish when integrating over the respective loop momentum. The term $A^{n_1} \star I^{n_2} \star A^{n_3}$ vanishes after a transformation of the loop momentum such that the momentum flowing through the set of propagators previously belonging to both loops is now one of the new loop momenta.

Reversing (D.4), we get

$$G_2 = F^{n_1} \star I^{n_2} \star I^{n_3} + I^{n_1} \star F^{n_2} \star I^{n_3} + I^{n_1} \star I^{n_2} \star F^{n_3} - 2I^{n_1} \star I^{n_2} \star I^{n_3}. \tag{D.6}$$

Using (3.12) we can substitute for F^{n_i}:

$$F^{n_i} = \prod_{k=1}^{n_i} \left(P_k^{(i)} + \frac{1}{2}\Delta_k^l + \frac{1}{2}\Delta_k^u \right) = \sum_{perm.} \frac{1}{2^{L_i+U_i}} \Delta^{l^{L_i}} \Delta^{u^{U_i}} P^{P_i}. \tag{D.7}$$

The coefficient C_{LUP} in (D.5) vanishes for even L_i. Thus, we only get a result different from zero in (D.6), if at least in two of the slots an odd number of delta functions Δ^l is present. Since the two coefficients in (D.5) and (D.7) are rather similar we can easily find the final result:

$$G_2 = \sum_{perm.} C_{G_2} \; \Delta^{l^{L_1}} \Delta^{u^{U_1}} P^{P_1} \star \Delta^{l^{L_2}} \Delta^{u^{U_2}} P^{P_2} \star \Delta^{l^{L_3}} \Delta^{u^{U_3}} P^{P_3}, \tag{D.8}$$

$$C_{G_2} = \frac{4}{2^{L+U}} \begin{cases} +1 & \text{for two } L_i \text{ odd, one } L_i \text{ even} \\ -1 & \text{for all } L_i \text{ odd} \\ 0 & \text{otherwise} \end{cases} \tag{D.9}$$

As expected, the leading terms are those where two cuts open both loops and result in a tree graph. These are given for two $L_i = 1$, the third being zero and also $U = 0$. Each term appears only once, $C_{G_2} = 1$. The final result $D.8$ looks rather simple. However, the peak structure of the resulting integrands might still be quite complicated. In this thesis we will not investigate multi loop graphs further and leave them to future work.

Bibliography

[1] S. Weinberg, "The Quantum theory of fields. Vol. 1: Foundations,". Cambridge, UK: Univ. Pr. (1995) 609 p.

[2] S. Weinberg, "The quantum theory of fields. Vol. 2: Modern applications,". Cambridge, UK: Univ. Pr. (1996) 489 p.

[3] M. E. Peskin and D. V. Schroeder, "An Introduction to quantum field theory,". Reading, USA: Addison-Wesley (1995) 842 p.

[4] M. Bohm, A. Denner, and H. Joos, "Gauge theories of the strong and electroweak interaction,". Stuttgart, Germany: Teubner (2001) 784 p.

[5] **Particle Data Group** Collaboration, W. M. Yao *et al.*, "Review of particle physics," *J. Phys.* **G33** (2006) 1–1232.

[6] J. Wess and B. Zumino, "A Lagrangian Model Invariant Under Supergauge Transformations," *Phys. Lett.* **B49** (1974) 52.

[7] J. Wess and B. Zumino, "Supergauge Transformations in Four-Dimensions," *Nucl. Phys.* **B70** (1974) 39–50.

[8] **LHC/LC Study Group** Collaboration, G. Weiglein *et al.*, "Physics interplay of the LHC and the ILC," *Phys. Rept.* **426** (2006) 47–358, `hep-ph/0410364`.

[9] T. Sjostrand, S. Mrenna, and P. Skands, "PYTHIA 6.4 physics and manual," *JHEP* **05** (2006) 026, `hep-ph/0603175`.

[10] S. Frixione and B. R. Webber, "Matching NLO QCD computations and parton shower simulations," *JHEP* **06** (2002) 029, `hep-ph/0204244`.

[11] A. Denner, S. Dittmaier, M. Roth, and D. Wackeroth, "RACOONWW 1.3: A Monte Carlo program for four-fermion production at e+ e- colliders," *Comput. Phys. Commun.* **153** (2003) 462–507, `hep-ph/0209330`.

[12] S. Jadach, W. Placzek, M. Skrzypek, B. F. L. Ward, and Z. Was, "The Monte Carlo event generator YFSWW3 version 1.16 for W pair production and decay at LEP2/LC energies," *Comput. Phys. Commun.* **140** (2001) 432–474, `hep-ph/0103163`.

[13] R. P. Feynman, "Quantum theory of gravitation," *Acta Phys. Polon.* **24** (1963) 697–722.

[14] T. Ohl, "Vegas revisited: Adaptive Monte Carlo integration beyond factorization," *Comput. Phys. Commun.* **120** (1999) 13–19, `hep-ph/9806432`.

[15] T. Hahn, "Generating Feynman diagrams and amplitudes with FeynArts 3," *Comput. Phys. Commun.* **140** (2001) 418–431, `hep-ph/0012260`.

[16] T. Hahn and M. Perez-Victoria, "Automatized one-loop calculations in four and D dimensions," *Comput. Phys. Commun.* **118** (1999) 153–165, `hep-ph/9807565`.

[17] M. Moretti, T. Ohl, and J. Reuter, "O'Mega: An optimizing matrix element generator," `hep-ph/0102195`.

[18] U. Mosel, "Path integrals in field theory: An introduction,". Berlin, Germany: Springer (2004) 213 p.

[19] J. C. Collins, "RENORMALIZATION. AN INTRODUCTION TO RENORMALIZATION, THE RENORMALIZATION GROUP, AND THE OPERATOR PRODUCT EXPANSION,". Cambridge, Uk: Univ. Pr. (1984) 380p.

[20] R. K. Ellis, H. Georgi, M. Machacek, H. D. Politzer, and G. G. Ross, "Perturbation Theory and the Parton Model in QCD," *Nucl. Phys.* **B152** (1979) 285.

[21] A. Denner, "Techniques for calculation of electroweak radiative corrections at the one loop level and results for W physics at LEP-200," *Fortschr. Phys.* **41** (1993) 307–420.

[22] G. 't Hooft and M. J. G. Veltman, "Regularization and Renormalization of Gauge Fields," *Nucl. Phys.* **B44** (1972) 189–213.

[23] B. W. Lee and J. Zinn-Justin, "Spontaneously Broken Gauge Symmetries. 1. Preliminaries," *Phys. Rev.* **D5** (1972) 3121–3137.

[24] B. W. Lee and J. Zinn-Justin, "Spontaneously broken gauge symmetries ii. perturbation theory and renormalization," *Phys. Rev.* **D5** (1972) 3137–3155.

[25] B. W. Lee and J. Zinn-Justin, "Spontaneously broken gauge symmetries. 3. Equivalence," *Phys. Rev.* **D5** (1972) 3155–3160.

[26] B. W. Lee and J. Zinn-Justin, "Spontaneously Broken Gauge Symmetries. 4. General Gauge Formulation," *Phys. Rev.* **D7** (1973) 1049–1056.

[27] D. A. Ross and J. C. Taylor, "RENORMALIZATION OF A UNIFIED THEORY OF WEAK AND ELECTROMAGNETIC INTERACTIONS," *Nucl. Phys.* **B51** (1973) 125–144.

[28] N. N. Bogoliubov and O. S. Parasiuk, "On the Multiplication of the causal function in the quantum theory of fields," *Acta Math.* **97** (1957) 227–266.

[29] W. Zimmermann, "Local Operator Products and Renormalization in Quantum Field Theory," in *Lectures on Elementary Particles and Quantum Field Theory*, Deser, Grisaru, and Pendleton, eds., vol. 1 of *1970 Brandeis University Summer Institute in Theoretical Physics*, pp. 395–592. The M.I.T. Press, 1970.

[30] J. C. Collins, "Renormalization: General theory," `hep-th/0602121`.

[31] W. Kilian, "WHIZARD 1.0: A generic Monte-Carlo integration and event generation package for multi-particle processes. Manual,". LC-TOOL-2001-039.

[32] W. Kilian, T. Ohl, and J. Reuter, "WHIZARD: Simulating Multi-Particle Processes at LHC and ILC," `arXiv:0708.4233 [hep-ph]`.

[33] T. Kinoshita, "Mass singularities of Feynman amplitudes," *J. Math. Phys.* **3** (1962) 650–677.

[34] T. D. Lee and M. Nauenberg, "Degenerate Systems and Mass Singularities," *Phys. Rev.* **133** (1964) B1549–B1562.

[35] F. Bloch and A. Nordsieck, "Note on the Radiation Field of the electron," *Phys. Rev.* **52** (1937) 54–59.

[36] G. Passarino and M. J. G. Veltman, "ONE LOOP CORRECTIONS FOR e+ e- ANNIHILATION INTO mu+ mu- IN THE WEINBERG MODEL," *Nucl. Phys.* **B160** (1979) 151.

[37] A. Denner and S. Dittmaier, "Reduction schemes for one-loop tensor integrals," *Nucl. Phys.* **B734** (2006) 62–115, `hep-ph/0509141`.

[38] T. Gehrmann, "Tools for NNLO QCD Calculations," `arXiv:0709.0351 [hep-ph]`.

[39] S. Weinzierl, "Automated calculations for multi-leg processes," `arXiv:0707.3342 [hep-ph]`.

[40] S. Laporta, "High-precision calculation of multi-loop Feynman integrals by difference equations," *Int. J. Mod. Phys.* **A15** (2000) 5087–5159, `hep-ph/0102033`.

[41] C. Anastasiou and A. Daleo, "Numerical evaluation of loop integrals," *JHEP* **10** (2006) 031, `hep-ph/0511176`.

[42] M. Czakon, "Automatized analytic continuation of Mellin-Barnes integrals," *Comput. Phys. Commun.* **175** (2006) 559–571, `hep-ph/0511200`.

[43] T. Binoth and G. Heinrich, "An automatized algorithm to compute infrared divergent multi-loop integrals," *Nucl. Phys.* **B585** (2000) 741–759, `hep-ph/0004013`.

[44] Z. Nagy and D. E. Soper, "Numerical integration of one-loop Feynman diagrams for N- photon amplitudes," *Phys. Rev.* **D74** (2006) 093006, `hep-ph/0610028`.

[45] C. Anastasiou, S. Beerli, and A. Daleo, "Evaluating multi-loop Feynman diagrams with infrared and threshold singularities numerically," *JHEP* **05** (2007) 071, `hep-ph/0703282`.

[46] D. E. Soper, "QCD calculations by numerical integration," *Phys. Rev. Lett.* **81** (1998) 2638–2641, `hep-ph/9804454`.

[47] D. E. Soper, "Techniques for QCD calculations by numerical integration," *Phys. Rev.* **D62** (2000) 014009, hep-ph/9910292.

[48] M. Kramer and D. E. Soper, "Next-to-leading order numerical calculations in Coulomb gauge," *Phys. Rev.* **D66** (2002) 054017, hep-ph/0204113.

[49] S. Catani and M. H. Seymour, "A general algorithm for calculating jet cross sections in NLO QCD," *Nucl. Phys.* **B485** (1997) 291–419, hep-ph/9605323.

[50] D. A. Kosower, "Antenna factorization of gauge-theory amplitudes," *Phys. Rev.* **D57** (1998) 5410–5416, hep-ph/9710213.

[51] A. Gehrmann-De Ridder, T. Gehrmann, and E. W. N. Glover, "Antenna subtraction at NNLO," *JHEP* **09** (2005) 056, hep-ph/0505111.

[52] R. P. Feynman, "Closed loop and tree diagrams,". In *J R Klauder, Magic Without Magic*, San Francisco 1972, 355-375.

[53] R. P. Feynman, "Problems in quantizing the gravitational field, and the massless Yang-Mills field,". In *J R Klauder, Magic Without Magic*, San Francisco 1972, 377-408.

[54] A. Arnold, K. Koehler, and P. Schlaile, "Numerische Berechnung von Strahlungskorrekturen," Diplomarbeiten, 2003. Universitaet Karlsruhe, Supervisor: W.Kilian.

[55] A. Brandhuber, B. Spence, and G. Travaglini, "From trees to loops and back," *JHEP* **01** (2006) 142, hep-th/0510253.

[56] R. E. Cutkosky, "Singularities and discontinuities of Feynman amplitudes," *J. Math. Phys.* **1** (1960) 429–433.

[57] L. D. Landau, "On analytic properties of vertex parts in quantum field theory," *Nucl. Phys.* **13** (1959) 181–192.

[58] V. S. Fadin and V. A. Khoze, "Threshold Behavior of Heavy Top Production in e+ e- Collisions," *JETP Lett.* **46** (1987) 525–529.

[59] D. R. Yennie, S. C. Frautschi, and H. Suura, "The infrared divergence phenomena and high-energy processes," *Ann. Phys.* **13** (1961) 379–452.

[60] S. Weinzierl, "Introduction to Monte Carlo methods," hep-ph/0006269.

[61] T. Ohl, "Electroweak gauge bosons at future electron positron colliders," hep-ph/9911437.

[62] G. P. Lepage, "A New Algorithm for Adaptive Multidimensional Integration," *J. Comput. Phys.* **27** (1978) 192.

[63] T. Hahn, "CUBA: A library for multidimensional numerical integration," *Comput. Phys. Commun.* **168** (2005) 78–95, hep-ph/0404043.

[64] R. Kleiss and R. Pittau, "Weight optimization in multichannel Monte Carlo," *Comput. Phys. Commun.* **83** (1994) 141–146, hep-ph/9405257.

[65] C. G. Papadopoulos, "PHEGAS: A phase space generator for automatic cross-section computation," *Comput. Phys. Commun.* **137** (2001) 247–254, hep-ph/0007335.

[66] F. Krauss, R. Kuhn, and G. Soff, "AMEGIC++ 1.0: A matrix element generator in C++," *JHEP* **02** (2002) 044, hep-ph/0109036.

[67] F. A. Berends, R. Pittau, and R. Kleiss, "All electroweak four fermion processes in electron - positron collisions," *Nucl. Phys.* **B424** (1994) 308–342, hep-ph/9404313.

[68] N. Toomi, J. Fujimoto, S. Kawabata, Y. Kurihara, and T. Watanabe, "Luminosity spectrum measurement in future e+ e- linear colliders using large-angle Bhabha events," *Phys. Lett.* **B429** (1998) 162–168.

[69] J. Brau *et al.*, "International Linear Collider reference design report. 1: Executive summary. 2: Physics at the ILC. 3: Accelerator. 4: Detectors,". ILC-REPORT-2007-001.

[70] M. L. G. Redhead, "Radiative Corrections to the Scattering of Electrons and Positrons by Electrons," *Royal Society of London Proceedings Series A* **220** (Nov., 1953) 219–239.

[71] F. A. Berends, K. J. F. Gaemers, and R. Gastmans, "alpha**3 Contribution to the angular asymmetry in e+ e- → mu+ mu-," *Nucl. Phys.* **B63** (1973) 381–397.

[72] F. A. Berends, K. J. F. Gaemers, and R. Gastmans, "Hard photon corrections for Bhabha scattering," *Nucl. Phys.* **B68** (1974) 541–550.

[73] M. Consoli, "ONE LOOP CORRECTIONS TO e+ e- → e+ e- IN THE WEINBERG MODEL," *Nucl. Phys.* **B160** (1979) 208.

[74] G. Montagna, O. Nicrosini, and F. Piccinini, "Precision physics at LEP," *Riv. Nuovo Cim.* **21N9** (1998) 1–162, hep-ph/9802302.

[75] R. Bonciani and A. Ferroglia, "Two-loop QED corrections to Bhabha scattering," *Nucl. Phys. Proc. Suppl.* **157** (2006) 11–15, hep-ph/0601246.

[76] S. Actis, M. Czakon, J. Gluza, and T. Riemann, "Fermionic NNLO contributions to Bhabha scattering," arXiv:0710.5111 [hep-ph].

[77] J. Fleischer, J. Gluza, A. Lorca, and T. Riemann, "First order radiative corrections to Bhabha scattering in d dimensions," *Eur. J. Phys.* **48** (2006) 35–52, hep-ph/0606210.

[78] F. A. Berends and R. Kleiss, "Distributions in the Process e+ e- → e+ e- (Gamma)," *Nucl. Phys.* **B228** (1983) 537.

[79] M. A. Dobbs *et al.*, "Les Houches guidebook to Monte Carlo generators for hadron collider physics," `hep-ph/0403045`.

[80] F. Maltoni and T. Stelzer, "MadEvent: Automatic event generation with MadGraph," *JHEP* **02** (2003) 027, `hep-ph/0208156`.

[81] A. Pukhov *et al.*, "CompHEP: A package for evaluation of Feynman diagrams and integration over multi-particle phase space. User's manual for version 33," `hep-ph/9908288`.

[82] T. Gleisberg *et al.*, "SHERPA 1.alpha, a proof-of-concept version," *JHEP* **02** (2004) 056, `hep-ph/0311263`.

[83] W. Kilian, J. Reuter, and T. Robens, "NLO event generation for chargino production at the ILC," *Eur. Phys. J.* **C48** (2006) 389–400, `hep-ph/0607127`.

[84] S. Catani, F. Krauss, R. Kuhn, and B. R. Webber, "QCD matrix elements + parton showers," *JHEP* **11** (2001) 063, `hep-ph/0109231`.

[85] Y. Kurihara *et al.*, "QCD event generators with next-to-leading order matrix-elements and parton showers," *Nucl. Phys.* **B654** (2003) 301–319, `hep-ph/0212216`.

[86] T. Robens, "Event generation for next to leading order chargino production at the International Linear Collider," `hep-ph/0610401`.

[87] D. Kiseilewska *et al.*, *Detector Outline Document for the Large Detector Concept.* LDC Working Group, http://www.ilcldc.org/documents/dod, 2006.

[88] K. Hagiwara and D. Zeppenfeld, "Helicity Amplitudes for Heavy Lepton Production in e+ e- Annihilation," *Nucl. Phys.* **B274** (1986) 1.

Acknowledgements

I am very grateful to my supervisor Wolfgang Kilian for advice, encouragement and a fruitful and nice atmosphere throughout the years. Furthermore, I want to thank Tania Robens and Jürgen Reuter for frequent help and suggestions. For careful reading of the preceding pages and valuable suggestions for making them readable, I want to thank Christian Schwinn, Kai Schmidt-Hoberg and Tania again.

For impressive three years, many thanks go to (in a rough order of appearance):
Markus, Tania, Toffi, H-Man, Benny, Danni, Dani, Kai, Dirk, Klaus, Nancy, Annika, Marie, Riccardo, Nico, Moïra, Gonzalo and all the others.

Finally, I want to thank my parents for support throughout all the years and of course:

Hamburg.